

**THE USE OF SURFACE WAVE METHODS IN TERRAIN  
SUCEPTIBLE TO SHALLOW LAND SLIDES IN THE CITY  
OF  
CAMPOS DO JORDÃO, BRAZIL**

**EMPREGO DE ONDAS SUPERFICIAIS EM TERRENO  
SUSCETÍVEL A ESCORREGAMENTOS NA CIDADE  
DE  
CAMPOS DO JORDÃO/SP**

Master Thesis in Geophysics

**Brian Sam Shams**

The Institute of Astronomy, Geophysics, and Atmospheric Science

University of São Paulo



**Supervisor:**

Renato Luiz Prado Ph.D.

**São Paulo, 2016**

## Acknowledgments

I owe a great deal of thanks to many people who have made it possible for me to not only accomplish my research goals, but also to manage the task of living abroad in Brazil.

I was first introduced to the subject of geophysics by Dr. James W. Rector at U.C. Berkeley, and I thank him for inspiring me to learn more about this unbelievable deep field of study. I would like to thank my advisor, Dr. Renato L. Prado, for always being helpful and kind. His guidance allowed me to narrow my broad research interests and eventually focus on a topic suitable for a master's degree. A special thanks to Dr. Choon Park for sharing his expertise and knowledge in using ParkSEIS© and in understanding the MASW method. I am thankful to Dr. Julian Ivanov and the staff at the Kansas Geological Survey for their help when I attended the SurfSeis© workshop in 2015. A word of gratitude to Rodrigo F. de Lucena for allowing me to use his dispersion function code, and for sharing his knowledge. Dr. Carlos A. Mendonça gave me the knowledge in the field of inversion to be able to create my own inversion code, for which I am very thankful. I am also thankful for Dr. Rodolfo M. Mendes sharing his geotechnical investigation for use in this research. I want to thank the faculty and staff at IAG-USP, who have always been very resourceful and helpful. In addition, I am very grateful to my friends and family who have always supported me and made me feel at home in São Paulo.

It is common amongst physicists, scientists, and mathematicians to name theories with the name of the originator as a sign of respect (i.e. Rayleigh wave, Love wave, Jacobian matrix, etc.). However, it must be recognized that much of the accumulated knowledge in these fields has been passed down from countless individuals whom history has forgotten. Therefore, I would like to thank, more than any individual, the human spirit of curiosity and the desire to share new knowledge.

## Abstract

This study seeks to prove the usefulness of the Multichannel Analysis of Surface Waves (MASW) method as complementary data to conventional geotechnical and geological data in the characterization of areas of landslide risk. The setting is located in a low income housing neighborhood in the city of Campos do Jordão, state of São Paulo, Brazil. The area was devastated by numerous landslides between December 1999 to January 2000 after heavy rainfall in the area. The landslides in this area are known to be shallow. Refraction and MASW surveys were performed in this research and then processed to obtain seismic velocity profiles of the subsurface. In order to better identify the fundamental mode of the Rayleigh wave, separate surveys isolating the vertical and radial components of the Rayleigh wave were performed. By comparing the inverted shear wave ( $V_S$ ) and compressional wave ( $V_P$ ) profiles with the already known geotechnical and geological data of the site, a better understanding of the geological interfaces that constitute the landslide prone area is obtained.

## Resumo

Este estudo busca demonstrar a aplicabilidade do método de análise multicanal de ondas superficiais (MASW) e a importância da integração de seus resultados com os da investigação geológica-geotécnica para a caracterização de áreas sujeitas a deslizamentos de terra. O local de estudo situa-se em uma área residencial com precárias condições de infraestrutura urbana na cidade de Campos do Jordão, estado de São Paulo, Brasil. Na área houve vários episódios de escorregamento entre dezembro de 1999 e janeiro de 2000 após a ocorrência de chuvas intensas. Os escorregamentos nesta área são classificados como rasos. Nesta pesquisa foram realizados ensaios de sísmica de refração e MASW e gerados perfis e seções de velocidade de propagação das ondas sísmicas. Para obter uma melhor identificação do modo fundamental da onda Rayleigh foram realizadas diferentes aquisições visando ao registro das componentes vertical e radial do movimento da onda. A integração dos perfis de velocidades da onda cisalhante ( $V_s$ ) e da onda compressional ( $V_p$ ) com os dados geológicos e geotécnicos obtidos anteriormente permitiu aprimorar o mapeamento das interfaces geológicas importantes para o estudo dos processos de escorregamento do local.

# CONTENTS

<b>1</b>	<b><u>Introduction</u></b> .....	<b>1-3</b>
1.1	<u>Motives</u> .....	2
1.2	<u>Objectives</u> .....	2-3
1.3	<u>Approach</u> .....	3
<b>2</b>	<b><u>Theoretical Background</u></b> .....	<b>4-35</b>
2.1	<u>Historical Overview of the Development of Near-Surface Seismic Methods</u> .....	4
2.2	<u>Surface Waves in an Infinite-Elastic-Isotropic-Homogeneous Half-Space</u> .....	4-5
2.2.1	<u>The Rayleigh Wave</u> .....	5-12
2.3	<u>Surface Waves in a Layered-Infinite-Elastic-Laterally Isotropic/Homogeneous Half-Space</u> .....	13
2.3.1	<u>Normal Mode Theory</u> .....	13-15
2.3.2	<u>The Love Wave</u> .....	15-20
2.3.3	<u>The Rayleigh Wave</u> .....	21-24
2.4	<u>Seismic Methods</u> .....	24
2.4.1	<u>Refraction WET Tomography</u> .....	24-26
2.4.1.1	<u>Field Measurements</u> .....	26
2.4.2	<u>MASW</u> .....	27
2.4.2.1	<u>Field Measurements</u> .....	28-32
2.4.2.2	<u>Data Processing</u> .....	32-33
2.4.2.3	<u>Curve Picking</u> .....	33-34
2.4.2.4	<u>Inversion</u> .....	34-35
2.4.3	<u>Love Wave Analysis</u> .....	35
<b>3</b>	<b><u>Area of Study</u></b> .....	<b>36-43</b>
3.1	<u>Landslide History and Data</u> .....	39-40
3.2	<u>Geological Information</u> .....	40-42

3.3	<a href="#">Existing Geotechnical Data</a>	43
<b>4</b>	<b><a href="#">Data Acquisition</a></b>	<b>44-46</b>
4.1	<a href="#">Site Investigations</a>	44-46
<b>5</b>	<b><a href="#">Data Processing and Analysis</a></b>	<b>47-51</b>
5.1	<a href="#">Refraction Data</a>	47
5.1.1	<a href="#">SH Wave Refraction Data</a>	47
5.1.2	<a href="#">P Wave Refraction Data</a>	47
5.2	<a href="#">Love Wave Data</a>	48
5.3	<a href="#">Passive MASW</a>	49
5.4	<a href="#">A-Priori Model</a>	50
5.5	<a href="#">Active MASW</a>	51
<b>6</b>	<b><a href="#">Results and Conclusions</a></b>	<b>52-53</b>
6.1	<a href="#">Limitations and Shortcomings</a>	52
6.2	<a href="#">Areas of Future Improvement</a>	52-53
6.3	<a href="#">Final Conclusions</a>	53
	<b><a href="#">References</a></b>	<b>54-58</b>
<b>Appendix A</b>	<b>– <a href="#">Elastic Wave Theory</a></b>	<b>59-66</b>
<b>Appendix B</b>	<b>– <a href="#">Dispersion Function Codes</a></b>	<b>67-70</b>
<b>Appendix C</b>	<b>– <a href="#">Synthetic Model Inversions with MATLAB® Code</a></b>	<b>71-75</b>
<b>Appendix D</b>	<b>– <a href="#">Refraction Data</a></b>	<b>76-83</b>
<b>Appendix E</b>	<b>– <a href="#">MASW Analysis Data</a></b>	<b>84-100</b>

## List of Variables

$x, y, z =$  coordinates (see appendix A)

$u_x, u_y, u_z =$  linear displacement

$\sigma_x, \sigma_y, \sigma_z =$  compressive(−) or tensile(+) normal stress

$\tau_{xy}, \tau_{xz}, \tau_{yx}, \tau_{yz}, \tau_{zx}, \tau_{zy} =$  shear stress<sub>(plane)(direction)</sub>

$\varepsilon_x, \varepsilon_y, \varepsilon_z =$  longitudinal strain, and  $\varepsilon_v =$  volumetric strain or dilation

$\gamma_{xy}, \gamma_{xz}, \gamma_{yx}, \gamma_{yz}, \gamma_{zx}, \gamma_{zy} =$  shear strain<sub>(plane)(direction)</sub>

$V_P = P -$  wave velocity

$V_S = S -$  wave velocity

$V_{SH} = S -$  wave velocity (horizontal component)

$V_{SV} = S -$  wave velocity (vertical component)

$V_R =$  Rayleigh – wave velocity (phase velocity)

$V_L =$  Love – wave velocity (phase velocity)

$\nu =$  Poisson's Ratio

$\rho =$  density

$\lambda, \mu =$  Lamé's constants

$E =$  Young's Modulus

$G =$  Shear Modulus

$h, H =$  Layer Thickness

$K =$  Bulk Modulus

$M = P -$  wave Modulus

$f =$  frequency (hz)

$\omega =$  Angular Frequency

$i =$  imaginary number

$k =$  wavenumber

$k_R =$  Rayleigh wavenumber

$k_L$  = Love wavenumber

$n$  = mode number (0 = fundamental, 1,2 ...  $\infty$  = higher modes) or layer number

$dx$  = Spacing between geophones

$x_1$  = Source offset (distance between source and closest geophone)

$x_T$  = Total length of geophone array

$\Delta d$  = Resolution of dispersion image (in terms of the phase velocity)

$z_{max}$  = The maximum depth of investigation (i.e. depth to half – space)

## List of Acronyms / Definitions

IAG – USP: The Institute of Astronomy, Geophysics, and Atmospheric Sciences at the University of São Paulo

MASW: Multichannel Analysis of Surface Waves

P Wave: A compression seismic wave (known originally as Primary Wave)

RMSE: Root mean square error

S Wave: A shear seismic wave (known originally as Secondary Wave)

SASW: Spectra Analysis of Surface Waves

SV Wave: A S wave with particle displacements occurring the vertical direction

SH Wave: A S wave with particle displacements occurring the horizontal direction

## List of Tables

[Table 2.1](#) – A table showing the recommended field parameters for MASW surveys by the KGS. (from Penumado, 2005) .....28

[Table 3.1](#) – Geotechnical characterization of the three deformed samples. (from Mendes et al., 2015) .....43

[Table 4.1](#) – A table of all field parameters for the seismic surveys used for this study. 44

# List of Figures

<a href="#">Figure 2.1</a>	– A graphical illustration of the exponentials in the wave equation .....	8
<a href="#">Figure 2.2</a>	– A graph of the Rayleigh wave to SV wave velocity ratio, with respect to Poisson’s ratio .....	11
<a href="#">Figure 2.3</a>	– P, S, and Rayleigh wave velocities with respect to Poisson’s Ratio. (from Richart, 1970) .....	11
<a href="#">Figure 2.4</a>	– Comparison of vertical and radial Rayleigh wave displacements, showing a 90° phase offset. (from Stein, 2009) .....	11
<a href="#">Figure 2.5</a>	– Rayleigh vertical and radial displacements with depth, and corresponding elliptical particle motion. (from Udías, 1999) .....	11
<a href="#">Figure 2.6</a>	– Rayleigh radial and vertical particle displacement profiles for a given frequency, showing variation with Poisson's ratio. (from Richart, 1970) ..	12
<a href="#">Figure 2.7</a>	– Rayleigh wave stress profile. (from Viktorov, 1967) .....	12
<a href="#">Figure 2.8</a>	– Cylindrical coordinates of an elastic rod. (from Udías, 1999) .....	13
<a href="#">Figure 2.9</a>	– An illustration of an elastic rod with fixed ends. (from Udías, 1999).....	13
<a href="#">Figure 2.10</a>	– Longitudinal displacement in an elastic rod due to the first three modes. (from Udías, 1999) .....	15
<a href="#">Figure 2.11</a>	– An illustration of the coordinate system and displacements caused by Love and Rayleigh waves. (from Stein, 2009) .....	15
<a href="#">Figure 2.12</a>	– The simple example model used in the derivation of the Love wave .....	16
<a href="#">Figure 2.13</a>	– Love wave (normalized) displacement profiles for each mode at a given frequency. From an example model (by Chen, 1993). Higher modes travel deeper. ....	18
<a href="#">Figure 2.14</a>	– Graph of the Love wave cutoff frequencies .....	19
<a href="#">Figure 2.15</a>	– MATLAB© code written to display the left-hand and right-hand sides of the Love wave dispersion function, Eq. (2.11) .....	19
<a href="#">Figure 2.16</a>	– A visualization of the left-hand and right-hand sides of the Love wave dispersion function (bottom). The Love wave dispersion curves are shown for the model shown in figure 2.12 (Top) .....	20
<a href="#">Figure 2.17</a>	– A visualization of a two-dimensional layered model, used for surface wave modeling .....	21

<a href="#">Figure 2.18</a>	– Rayleigh wave displacement profiles for both vertical and horizontal components for each mode at a given frequency. From an example model (by Chen, 1993) .....	23
<a href="#">Figure 2.19</a>	– Rayleigh wave dispersion curves for the fundamental mode and three higher modes of an example model. (from Udías, 1999) .....	24
<a href="#">Figure 2.20</a>	– An illustration of ray paths crossing a gridded region in a study of seismic tomography of the earth. (from Udías, 1999) .....	25
<a href="#">Figure 2.21</a>	– A schematic representation of a Fresnel volume with a source and a receiver. (from Watanabe, 1999) .....	25
<a href="#">Figure 2.22</a>	– An illustration of a refraction site investigation with a linear array of geophones and a sledgehammer as an active source .....	26
<a href="#">Figure 2.23</a>	– An illustration of an active source MASW field survey using a linear geophone array .....	27
<a href="#">Figure 2.24</a>	– An illustration of the field parameters for a MASW survey (from Penumadu, 2005).....	28
<a href="#">Figure 2.25</a>	– A dispersion image illustrating the phase velocity resolution. (from Xia et al., 2005) .....	30
<a href="#">Figure 2.26</a>	– An illustration of the optimum offset range and how body waves eventually dominate energy of high frequencies after a certain distance. Modified from the short course notes of SurfSeis© by the KGS .....	31
<a href="#">Figure 2.27</a>	– A visualization of the site investigation, multichannel record, and dispersion image that is an output of MASW data processing (from Park, 2005) .....	33
<a href="#">Figure 2.28</a>	– An illustration of the MASW 3-step procedure after field measurements, data processing, curve fitting, and inversion. (from Park et al., 2004).....	34
<a href="#">Figure 3.1</a>	– Visualization of the area of study using data from a digital elevation model via NASA SRTM.....	36
<a href="#">Figure 3.2</a>	– A recent satellite image of the city of Campos do Jordão, and satellite images of the neighborhood of Santo Antônio from 1972, 1982, and recently. (from Ahrendt, 2005 and Mendes et al., 2015).....	37
<a href="#">Figure 3.3</a>	– A panoramic view of a section of the Santo Antônio neighborhood (from Ahrendt, 2005) .....	37
<a href="#">Figure 3.4</a>	– A Google Earth satellite image of the site of investigation .....	38
<a href="#">Figure 3.5</a>	– Images of the site of investigation from the field.....	38

<a href="#">Figure 3.6</a>	– The aftermath of landslides in the neighborhood of Santo Antônio during the winter of 1999-2000. (from Ahrendt, 2005).....	39
<a href="#">Figure 3.7</a>	– Devastating landslides which occurred in the nearby neighborhood of Britador. (from Ahrendt, 2005) .....	39
<a href="#">Figure 3.8</a>	– Shallow landslides that occurred in the Santo Antônio neighborhood of Campos do Jordão. (from Ahrendt, 2005) .....	39
<a href="#">Figure 3.9</a>	– Images of landslides which occurred in the city of Campos do Jordão in January, 2000. (from Mendes et al., 2015).....	40
<a href="#">Figure 3.10</a>	– Evolution of the topography of the Campos do Jordão plateau from the Paleocene to the Holocene and geological profiles obtained by drilling. (from Modenesi et al., 2010). .....	41
<a href="#">Figure 3.11</a>	– A profile view of the Santo Antônio neighborhood showing the topography and near-surface geological groups defined by Ahrendt, 2005 .....	42
<a href="#">Figure 3.12</a>	– Soil profile from geotechnical investigation (from Mendes et al., 2015). ..	43
<a href="#">Figure 4.1</a>	– Google Earth satellite image of the area of study and the survey line.. .....	44
<a href="#">Figure 4.2</a>	– An illustration of the “fixed” long array and the “move-along” short arrays used for surveys 2 and 3.. .....	45
<a href="#">Figure 4.3</a>	– Configuration of the circular array used for the passive-MASW survey....	46
<a href="#">Figure 5.1</a>	– A dispersion image of Love wave energy obtained by processing through SurfSeis©.....	48
<a href="#">Figure 5.2</a>	– Inversion of the passive MASW survey with circular array obtained by processing through ParkSEIS© .....	49
<a href="#">Figure 5.3</a>	–The interpreted a-priori model of the site of investigation.....	50
<a href="#">Figure A.1</a>	– Stress-strain curves under elastic, elastic-plastic, plastic, and viscoelastic regimes.....	59
<a href="#">Figure A.2</a>	– An illustration of the coordinate system used in presented equations.....	60
<a href="#">Figure A.3</a>	– An illustration of Hooke's law in three dimensions (adapted from Santamarina, 2001).....	62
<a href="#">Figure A.4</a>	– The relationship between shear stress and shear strain .....	62
<a href="#">Figure A.5</a>	– Five Stresses acting on an element during wave propagation. (adapted from Santamarina, 2001).....	64
<a href="#">Figure A.6</a>	– P wave propagation (from Stokoe & Santamarina, 2000).....	65
<a href="#">Figure A.7</a>	– SV wave propagation (from Stokoe & Santamarina, 2000).....	66

<a href="#">Figure A.8</a>	– SH wave propagation.....	66
<a href="#">Figure C.1</a>	– Properties of a simple two-layer model (1). .....	71
<a href="#">Figure C.2</a>	– A graph showing the 10 points used for inversion of the fundamental mode dispersion curve for model 1 .....	71
<a href="#">Figure C.3</a>	– Results of the inversion of model 1 using MATLAB® code .....	72
<a href="#">Figure C.4</a>	– Properties of model 2 (model from Xia et al., 1999).. .....	73
<a href="#">Figure C.5</a>	– A graph showing the 10 points used for inversion of the fundamental mode dispersion curve for model 2 .....	73
<a href="#">Figure C.6</a>	– Results of the inversion of model 2 using MATLAB® code .....	74
<a href="#">Figure C.7</a>	– Sensitivity analysis of the model from Xia et al., 1999 .....	75
<a href="#">Figure D.1</a>	– Picked arrivals for near shot offset SH wave refraction survey .....	76
<a href="#">Figure D.2</a>	– Picked arrivals for medium shot offset SH wave refraction survey. ....	76
<a href="#">Figure D.3</a>	– Picked arrivals for far shot offset SH wave refraction survey.....	77
<a href="#">Figure D.4</a>	– Travel time curves for SH wave refraction survey.....	77
<a href="#">Figure D.5</a>	– Smoothed WET inversion of SH wave refraction data .....	78
<a href="#">Figure D.6</a>	– Wave coverage of SH wave refraction data .....	78
<a href="#">Figure D.7</a>	– All picked first arrivals for P wave refraction survey .....	79-82
<a href="#">Figure D.8</a>	– Travel time curves for P wave refraction survey.....	82
<a href="#">Figure D.9</a>	– Smoothed WET inversion of P wave refraction data. ....	83
<a href="#">Figure D.10</a>	–Wave coverage of P wave refraction data .....	83
<a href="#">Figure E.1</a>	– Diagram of shot locations and geophone array for the short arrays.. ..	84
<a href="#">Figure E.2</a>	– Dispersion images for the top array (from Figure E.1) for a variety of shot locations. Horizontal and vertical components are shown separately and then combined.....	85
<a href="#">Figure E.3</a>	– Dispersion images for the middle array (from Figure E.1) for a variety of shot locations. Horizontal and vertical components are shown separately and then combined.....	86
<a href="#">Figure E.4</a>	– Dispersion images for the bottom array (from Figure E.1) for a variety of shot locations. Horizontal and vertical components are shown separately and then combined.....	87

<a href="#">Figure E.5</a>	– Individual inversions of the picked dispersion curves of the best dispersion images for each short array.....	88
<a href="#">Figure E.6</a>	– Interpolated 2-D shear wave velocity profile inversion, from 3 1-D inversions for each short array (top). Associated 2-D confidence profile (bottom). ..	89
<a href="#">Figure E.7</a>	– A-priori model inputted into SurfSeis© as the initial model in the inversion process..	90
<a href="#">Figure E.8</a>	– Interpolated 2-D shear wave velocity profile inversion, from 3 1-D inversions for each short array. Result of using a-priori information as a starting model, in SurfSeis©.....	90
<a href="#">Figure E.9</a>	– Associated RMSE profile.....	90
<a href="#">Figure E.10</a>	–A diagram of the long array, showing shot locations .....	91
<a href="#">Figure E.11</a>	–Dispersion images for the long array for a variety of shot locations. Horizontal and vertical components are shown separately and then combined..	92
<a href="#">Figure E.12</a>	–Individual inversions of the picked dispersion curves of the best dispersion images.....	93
<a href="#">Figure E.13</a>	–Reanalysis of the bottom picked dispersion curve in Figure E.12, by adding one more point at a lower frequency. ....	94
<a href="#">Figure E.14</a>	–Inversion of the redefined dispersion curve using the default initial model in SurfSeis©.....	94
<a href="#">Figure E.15</a>	– Synthetic model derived from the inversion results from figure E.14 for the long array as well as modeling settings .....	95
<a href="#">Figure E.16</a>	– Comparison of real and synthetic seismograms for the vertical component at shot location 6 for the long array.....	96
<a href="#">Figure E.17</a>	– Comparison of real and synthetic seismograms for the horizontal (or radial) component at shot location 6 for the long array .....	97
<a href="#">Figure E.18</a>	– Comparison of real and synthetic dispersion images for the vertical component at shot location 6 for the long array. ....	98
<a href="#">Figure E.19</a>	– Comparison of real and synthetic dispersion images for the horizontal (or radial) component at shot location 6 for the long array.....	99
<a href="#">Figure E.20</a>	– Comparison of real and synthetic dispersion images for the combined vertical and horizontal components at shot location 6 for the long array .....	100

# List of Equations

<a href="#">Eq. 2.1</a>	– Displacement in the x direction in terms of undefined harmonic functions .....	5
<a href="#">Eq. 2.2</a>	– Displacement in the z direction in terms of undefined harmonic functions .....	5
<a href="#">Eq. 2.3</a>	– Generalized definition of the harmonic function $\Phi$ .....	8
<a href="#">Eq. 2.4</a>	– Generalized definition of the harmonic function $\Psi$ .....	8
<a href="#">Eq. 2.5</a>	– The solvable harmonic function $\Phi$ for Rayleigh waves in an infinite-elastic-isotropic-homogeneous half-space .....	9
<a href="#">Eq. 2.6</a>	– The solvable harmonic function $\Psi$ for Rayleigh waves in an infinite-elastic-isotropic-homogeneous half-space .....	9
<a href="#">Eq. 2.7</a>	– The solved equation for displacement in the x direction for Rayleigh waves in an infinite-elastic-isotropic-homogeneous half-space .....	9
<a href="#">Eq. 2.8</a>	– The solved equation for displacement in the z direction for Rayleigh waves in an infinite-elastic-isotropic-homogeneous half-space .....	9
<a href="#">Eq. 2.9</a>	– An equation relating $V_R$ to $V_{SV}$ in terms of Poisson’s ratio .....	10
<a href="#">Eq. 2.10</a>	– The solved equation for displacement in the y direction for Love waves in a two-layer infinite-elastic-laterally-isotropic-homogeneous half-space .....	18
<a href="#">Eq. 2.11</a>	– The dispersion function for Love waves in a two-layer infinite-elastic-laterally-isotropic-homogeneous half-space .....	19
<a href="#">Eq. 2.12</a>	– The dispersion curve cutoff frequencies for Love waves in a two-layer infinite-elastic-laterally-isotropic-homogeneous half-space .....	19
<a href="#">Eq. 2.13</a>	– The nearest offset from a source that is sufficiently far away to where a Rayleigh wave can be generated in a simplified two-layered model (from Xia et al., 2005) .....	30
<a href="#">Eq. 2.14</a>	– The objective function used in the MATLAB® code .....	35
<a href="#">Eq. A.1</a>	– The wave equation for propagation in the x direction in terms of stress ....	64
<a href="#">Eq. A.2</a>	– Equation A.1 in terms of strain, after applying Hooke’s law .....	64
<a href="#">Eq. A.3</a>	– Equation A.1 in terms of displacement, after applying Hooke’s law .....	64

## Chapter 1 - Introduction

Observing seismic waves traveling through the subsurface can provide important information for mapping the properties of shallow soils and sediments. Because the properties of seismic waves are related to certain properties of the media through which the waves travel, these properties can be deduced from the observation and measurement of seismic wave propagation.

In a region prone to shallow landslide danger, obtaining the properties of shallow soils and sediments can play an important role in understanding the subsurface and potentially helping to minimize risk to local inhabitants. There are many variables that may influence the occurrence of a landslide, such as meteorological variables (i.e. rain intensity, duration, etc.), geological variables (i.e. mineralogical composition, weathering, etc.), geotechnical variables (i.e. moisture content, water level, etc.), seismicity variables (i.e. soil stiffness, damping ratio, etc.), and human variables (i.e. poor standards of construction, man-made debris, etc.). Some of these variables are directly and indirectly related, and many can belong to more than one category.

Geotechnical drilling and lab testing can obtain near-surface soil and sediment properties. However, this practice is not only costly and time consuming but is limited to sampling very small sections as wide as the borehole and interpolating between them. For the cost of lower resolution, possible ambiguities of solution sets, and obtaining only a limited set of properties which can only indirectly relate to geological and geotechnical properties, geophysical methods offer the following advantages: (1) flexibility and high investigation speed, (2) non-invasive testing with the ability to determine the internal structure of the subsurface, (3) investigating a large volume of the subsurface, and (4) being relatively low-cost (Jongmans & Garambois, 2007). Although there exist various geophysical methods to obtain soil and sediment properties, seismic methods can nearly always determine the internal structure of materials in a slope; and furthermore, seismic refraction has been a standard tool for geotechnical investigations for many years (Hack, 2000). There are many examples of seismic refraction being used in post-landslide reconnaissance investigations, as in Bogoslovsky et al. (1977), Caris et al. (1991), Godio et al. (2005), Glade et al. (2004), Spillmann et al. (2007), and Willenberg et al. (2008). In recent years, surface wave analysis has become a popular seismic method and is often used in combination with seismic refraction, as they can share the same geophone array (Havenith et al., 2000, Jongmans et al., 2009, Grandjean et al., 2011). Attempts at joint inversion of refraction and surface wave analysis have also been performed (Ivanov, 2002). Investigations performed in landslide-prone areas using only surface wave analysis (Coccia et al., 2010) are also seen in the literature.

However, many published studies using seismic techniques in landslide regions are typically located in non-tropical regions and often in mountainous alpine environments, where sharp velocity contrasts are common at the near surface. In contrast, in tropical regions intensive chemical weathering leads to the formation of a thick weathering crust

over the bedrock (Chamley, 1990). This thick layer of weathering crust can make near-surface seismic investigations more difficult by reducing sharp contrasts in geological material at the near surface, and therefore sharp contrasts of seismic properties (i.e. stiffness, wave velocity). Since many seismic methods rely on the assumption that the subsurface is layered, this thick weathering crust may provide a challenge for reliable data processing and inversion.

Furthermore, surface wave analysis for the purpose of near surface geotechnical investigation (i.e. shear wave velocity inversion) is currently under rapid evolution, as the method still suffers from some issues preventing reliable inversions for a variety of conditions (Socco et al. 2000).

This study provides an opportunity to investigate the advantages and disadvantages of surface wave analysis techniques to determine the near surface seismic properties of a tropical region prone to shallow landslides and to discuss ideas to improve these near surface seismic methods.

## 1.1 Motives

This research seeks to contribute to the problem of understanding the subsurface of terrain prone to shallow landslides and to understand the potential contribution of the multichannel analysis of surface waves (MASW) method to this end. Furthermore, the importance of a-priori information in the MASW inversion process is also studied to investigate the viability of the current MASW inversion methods, by means of commercial software SurfSeis©, and ParkSEIS©.

It is hoped that this research will help develop, promote, and understand geophysical techniques that can aid geotechnical engineers in various engineering problems that require an understanding of the subsurface. It is the opinion of the author that advances in near surface geophysical techniques may revolutionize the practice of geotechnical site investigations. By giving the engineer more tools to measure the subsurface we can expect a greater degree of accuracy in the assessment of vital geotechnical parameters, which can be of immense importance in various engineering projects.

## 1.2 Objectives

The **primary objective** of this study is to test the multichannel analysis of surface waves (MASW) (Park et al., 1999) method in an environment that challenges the underlying assumptions of the method. The study site is located in a mountainous tropical environment with challenging topography and a very thick weathered layer (residual soil and saprolite).

We can consider the **secondary objective** to be the exploration of MASW inversion results when considering a-priori data. In this study a-priori data is assumed from existing

geotechnical and geological data as well as other seismic methods performed on site (Seismic Refraction, Love Wave, and Passive MASW surveys).

The **key deliverable** of this project is the near-surface shear wave velocity profile of the study site.

## 1.3 Approach

As explained in section 1.1, the MASW method is the focus of this study.

The general approach of this study can be divided into the following steps:

- Gather all relevant geotechnical and geological data available for the site and surrounding region.
- Perform refraction and surface wave investigations at the site.
- Process refraction and surface wave (excluding the active MASW survey) data separately, and verify consistency.
- Develop an a-priori model with a combination of geotechnical/geological data and seismic inversion (excluding the active MASW survey) results.
- Invert MASW (Rayleigh wave) data both considering a-priori data and not, and compare results.

## Chapter 2 - Theoretical Background

### 2.1 Historical Overview of the Development of Near-Surface Seismic Methods

In the mid-to-late nineteenth century, the first seismic exploration methods were developed from early earthquake studies. 1846 saw Robert Mallet be the first man to use an “artificial” energy source in a seismic experiment; he also became the first man to use the term “seismology”. August Schmidt created the travel time-distance graph in 1888 for the determination of seismic velocities; this graph is fundamental to many modern seismic methods. G.K. Knott explained the phenomenon of seismic propagation, refraction, and reflection in 1899. The combination of two world wars, a boom in the oil & gas industry, and the invention of the computer made the twentieth century an exceptional period of growth for applied seismology. By the 1920s seismic reflection had become widely used for the exploration of hydrocarbons and soon became the dominant method for the exploration of oil and gas throughout the world. Seismic refraction methods were also being developed with the invention of the ‘Plus-Minus’ method by J.G. Hagedoorn in 1959 and the ‘reciprocal method’ by L.V. Hawkins in 1961. R. Jones was among the first to propose engineering applications in surface-wave analysis (Jones, 1958, 1962). Soon a new method, named the spectral analysis of surface waves (SASW) (Nazarian & Stokoe, 1984), made surface-wave analysis popular among the engineering community, and is still popular to the present day (Socco, Foti, & Boiero, 2010). And more recently, the multichannel analysis of surface waves (MASW) method, developed by researchers from the Kansas Geological Survey (Park et al., 1999), has become a popular way to analyze surface waves while using the same survey configuration of a common refraction survey. Much of the historical information provided in this paragraph is based on (Reynolds, 2011).

Modern applied seismology is divided into three branches: refraction, reflection, and surface wave analysis. Reflection analysis is the most powerful method for oil exploration due to its ability to image deep structures. Refraction and surface wave analysis, however, have been consistently used for near surface applications useful to engineers interested in the shallow subsurface. These are the two methods used in this study.

### 2.2 Surface Waves in an Infinite-Elastic-Isotropic-Homogeneous Half-Space

This section reviews the most common derivation of Rayleigh waves seen in many seismology textbooks (Aki & Richards, 1980; Chapman, 2004; Lay & Wallace, 1995;

Shearer, 2009; Stein, 2009; Udías, 1999). The Rayleigh wave derivation presented in this section is mostly influenced by Kramer (2002). Assuming a homogeneous half space with no layering greatly simplifies the Rayleigh wave problem, but it is important to note that although many characteristics are shared between Rayleigh waves in homogeneous media and layered media, there are also some major differences such as normal modes and dispersion. Definitions of elastic moduli and related terms can be found in Appendix A.

## 2.2.1 The Rayleigh wave

There is only one kind of surface wave that can exist in an infinite-elastic-isotropic-homogeneous half-space, the Rayleigh Wave. Let us assume a two-dimensional space where  $z$  is the vertical axis and  $x$  is the horizontal axis.

Let us define horizontal displacement ( $u_x$ ) and vertical displacement ( $u_z$ ) as the following differential equations,

$$u_x = \frac{\partial \Phi}{\partial x} + \frac{\partial \Psi}{\partial z} \quad (2.1)$$

$$u_z = \frac{\partial \Phi}{\partial z} - \frac{\partial \Psi}{\partial x} \quad (2.2)$$

Now we must define the harmonic (or potential) functions  $\Phi$  and  $\Psi$ . In order to do this, we must introduce the wave equation for a two dimensional elastic solid, and then we can define volumetric strain and rotational strain in terms of  $\Phi$  and  $\Psi$ .

Introducing the wave equations for two-dimensions ( $x, z$ ) in terms of stress,

$$\begin{aligned} \rho \frac{\partial^2 u_x}{\partial t^2} &= \frac{\partial \sigma_x}{\partial x} + \frac{\partial \tau_{yx}}{\partial y} + \frac{\partial \tau_{zx}}{\partial z} \\ \rho \frac{\partial^2 u_z}{\partial t^2} &= \frac{\partial \tau_{xz}}{\partial x} + \frac{\partial \tau_{yz}}{\partial y} + \frac{\partial \sigma_z}{\partial z} \end{aligned}$$

Now we can write the two wave equations in terms of strain by using Hooke's law,

$$\begin{aligned} \rho \frac{\partial^2 u_x}{\partial t^2} &= (\lambda + \mu) \frac{\partial \varepsilon_v}{\partial x} + \mu \nabla^2 u_x \\ \rho \frac{\partial^2 u_z}{\partial t^2} &= (\lambda + \mu) \frac{\partial \varepsilon_v}{\partial z} + \mu \nabla^2 u_z \end{aligned}$$

Now let us define volumetric strain and rotational strain in terms of  $\Phi$  and  $\Psi$ ,

$$2D \text{ volumetric strain} = \varepsilon_v = \varepsilon_{xx} + \varepsilon_{zz} = \frac{\partial u_x}{\partial x} + \frac{\partial u_z}{\partial z} = \frac{\partial}{\partial x} \left( \frac{\partial \Phi}{\partial x} + \frac{\partial \Psi}{\partial z} \right) + \frac{\partial}{\partial z} \left( \frac{\partial \Phi}{\partial z} - \frac{\partial \Psi}{\partial x} \right) = \frac{\partial^2 \Phi}{\partial x^2} + \frac{\partial^2 \Phi}{\partial z^2} = \nabla^2 \Phi$$

$$\text{rotational strain in } x - z \text{ plane} = 2\Omega_y = 2 \left( \frac{1}{2} \left( \frac{\partial u_x}{\partial z} - \frac{\partial u_z}{\partial x} \right) \right) = \frac{\partial}{\partial z} \left( \frac{\partial \Phi}{\partial x} + \frac{\partial \Psi}{\partial z} \right) - \frac{\partial}{\partial x} \left( \frac{\partial \Phi}{\partial z} - \frac{\partial \Psi}{\partial x} \right) = \frac{\partial^2 \Psi}{\partial z^2} + \frac{\partial^2 \Psi}{\partial x^2} = \nabla^2 \Psi$$

Now we can write the two wave equations in terms of  $\Phi$  and  $\Psi$  by using the definition  $u_x$  and  $u_y$  from equations 2.1 and 2.2,

$$\rho \frac{\partial}{\partial x} \left( \frac{\partial^2 \Phi}{\partial t^2} \right) + \rho \frac{\partial}{\partial z} \left( \frac{\partial^2 \Psi}{\partial t^2} \right) = (\lambda + 2\mu) \frac{\partial}{\partial x} (\nabla^2 \Phi) + \mu \frac{\partial}{\partial z} (\nabla^2 \Psi)$$

$$\rho \frac{\partial}{\partial z} \left( \frac{\partial^2 \Phi}{\partial t^2} \right) - \rho \frac{\partial}{\partial x} \left( \frac{\partial^2 \Psi}{\partial t^2} \right) = (\lambda + 2\mu) \frac{\partial}{\partial z} (\nabla^2 \Phi) - \mu \frac{\partial}{\partial x} (\nabla^2 \Psi)$$

Now we can simultaneously solve these two wave equations to obtain,

$$\frac{\partial^2 \Phi}{\partial t^2} = \frac{\lambda + 2\mu}{\rho} \nabla^2 \Phi = V_P^2 \nabla^2 \Phi$$

$$\frac{\partial^2 \Psi}{\partial t^2} = \frac{\mu}{\rho} \nabla^2 \Psi = V_{SV}^2 \nabla^2 \Psi$$

Assuming that the wave is harmonic and propagates with the Rayleigh wave velocity, we can express  $\Phi$  and  $\Psi$  as,

$$\Phi = F(z) e^{i(\omega t - k_r x)}$$

$$\Psi = G(z) e^{i(\omega t - k_r x)}$$

where the functions  $F(z)$  and  $G(z)$  describe the variation of volumetric strain and rotational strain with depth.

Inserting these two harmonic functions into the solutions to the wave equations yields,

$$-\frac{\omega^2}{v_p^2}F(z) = -k_R^2F(z) + \frac{d^2F(z)}{dz^2}$$
$$-\frac{\omega^2}{v_{SV}^2}G(z) = -k_R^2G(z) + \frac{d^2G(z)}{dz^2}$$

and rearranging these two equations gives,

$$\frac{d^2F}{dz^2} - \left(k_R^2 - \frac{\omega^2}{v_p^2}\right)F = 0$$
$$\frac{d^2G}{dz^2} - \left(k_R^2 - \frac{\omega^2}{v_{SV}^2}\right)G = 0$$

The general solution of these two equations is as follows,

$$F(z) = A_1e^{-qz} + B_1e^{qz}$$
$$G(z) = A_2e^{-sz} + B_2e^{sz}$$

where the arbitrary constants  $q$  and  $s$  are defined as,

$$q = \sqrt{k_R^2 - \frac{\omega^2}{v_p^2}}$$
$$s = \sqrt{k_R^2 - \frac{\omega^2}{v_{SV}^2}}$$

We can see that the general solution contains a linear combination of two types of exponentials.

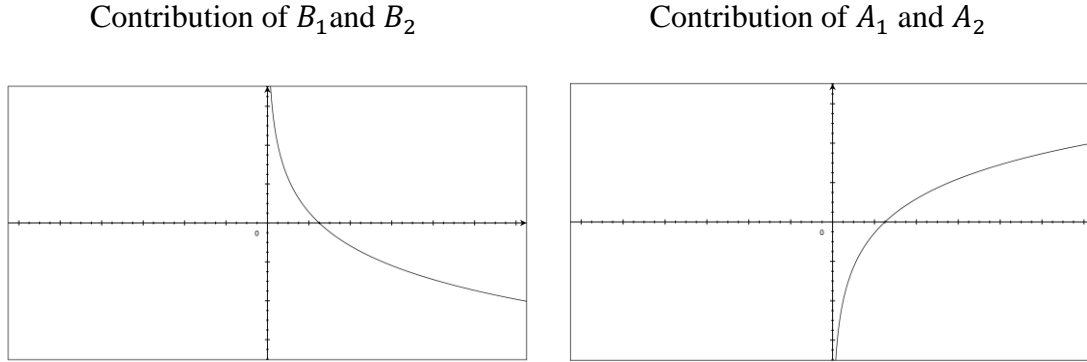


Figure 2.1 - A graphical illustration of the exponential functions that constants  $A_1, A_2, B_1, B_2$  are multiplied by. On the left is plotted  $x = \exp(z)$ , and on the right  $x = \exp(-z)$ , keep in mind that  $z$  is positive in the down direction.

It is unrealistic for the amplitude of displacement to increase to infinity with depth, and therefore we can assume the terms of  $B_1$  and  $B_2$  to be 0. Another way to think of this is that  $B_1$  and  $B_2$  represent the amplitudes of the upward going reflected waves from an interface. However, since we are assuming an infinite isotropic medium, there are no interfaces, and therefore these terms must be 0.

Therefore,

$$F(z) = A_1 e^{-qz}$$

$$G(z) = A_2 e^{-sz}$$

and now the harmonic functions  $\Phi$  and  $\Psi$  can be defined as,

$$\Phi = A_1 e^{-qz+i(\omega t - k_r x)} \tag{2.3}$$

$$\Psi = A_2 e^{-sz+i(\omega t - k_R x)} \tag{2.4}$$

We now have two equations and three unknowns ( $A_1, A_2, k_r$ ). We can eliminate  $A_2$  by introducing the boundary condition that neither shear nor normal stress can exist at the free surface ( $z = 0$ ).

$$\sigma_{z(z=0)} = \lambda \varepsilon_v + 2\mu \varepsilon_z = \lambda \varepsilon_v + 2\mu \frac{du_z}{dz} = 0$$

$$\tau_{zx(z=0)} = \mu \varepsilon_{xz} = \mu \left( \frac{du_z}{dx} + \frac{du_x}{dz} \right) = 0$$

We can rewrite these boundary conditions using the definitions of  $u_x$  and  $u_z$  in terms of the harmonic functions  $\Phi$  and  $\Psi$  given in equations (2.1) and (2.2) and the general solutions to  $\Phi$  and  $\Psi$  given by equations (2.3) and (2.4) as,

$$\sigma_{z(z=0)} = A_1[(\lambda + 2\mu)q^2 - \lambda k_R^2] - 2iA_2\mu k_R s = 0$$

$$\tau_{zx(z=0)} = 2iA_1 k_R q + A_2(s^2 + k_R^2) = 0$$

Now we can define  $A_2$  in terms of  $A_1$ ,

$$A_2 = -\frac{A_1 2iqk_R}{s^2 + k_R^2}$$

and finally the “solvable” harmonic functions  $\Phi$  and  $\Psi$  can be expressed as,

$$\Phi = A_1 e^{-qz + i(\omega t - k_R x)} \quad (2.5)$$

$$\Psi = -\frac{A_1 2iqk_R}{s^2 + k_R^2} e^{-sz + i(\omega t - k_R x)} \quad (2.6)$$

where,

$$A_1 \left( \frac{(\lambda + 2\mu)q^2 - \lambda k_R^2}{2i\mu k_R s} + \frac{2iqk_R}{s^2 + k_R^2} \right) = 0$$

Now we can define the distribution of the amplitude of displacement due to a Rayleigh Wave.

By using the definition of the harmonic functions  $\Phi$  and  $\Psi$ , we can write the horizontal displacement ( $u_x$ ) and vertical displacement ( $u_z$ ) as the following,

$$u_x = A_1 \left( -ik_R e^{-qz} + \frac{2iqsk_R}{s^2 + k_R^2} e^{-sz} \right) e^{i(\omega t - k_R x)} \quad (2.7)$$

$$u_z = A_1 \left( \frac{2qk_R^2}{s^2 + k_R^2} e^{-sz} - q e^{-qz} \right) e^{i(\omega t - k_R x)} \quad (2.8)$$

And finally we can define the Rayleigh wave velocity by equating the boundary conditions, which gives us,

$$4q\mu s k_R^2 = (s^2 + k_R^2)[(\lambda + 2\mu)q^2 - \lambda k_R^2]$$

By applying the definitions of  $q$  and  $s$  and factoring out  $\mu^2 k_r^8$  we can obtain,

$$16 \left(1 - \frac{\omega^2}{V_P^2 k_R^2}\right) \left(1 - \frac{\omega^2}{v_{SV}^2 k_R^2}\right) = \left(2 - \frac{\lambda+2\mu}{\mu} \frac{\omega^2}{V_P^2 k_R^2}\right)^2 \left(2 - \frac{\omega^2}{v_{SV}^2 k_R^2}\right)^2$$

Let us now rewrite this equation in terms of the Rayleigh-wave to S-Wave and P-Wave ratios where,

$$\frac{V_r}{V_{SV}} = \frac{\omega}{V_{SV} k_R}$$

$$\frac{V_R}{V_P} = \frac{\omega}{V_P k_R} = \frac{\omega}{V_{SV} k_R \sqrt{(\lambda+2\mu)/\mu}} = \alpha \frac{\omega}{V_{SV} k_R} = \alpha \frac{V_R}{V_{SV}}$$

where,

$$\alpha = \sqrt{\frac{\mu}{(\lambda+2\mu)}} = \sqrt{\frac{(1-2\nu)}{(2-2\nu)}}$$

Now rewriting the equation in terms of this ratio, and after expanding and rearranging we obtain,

$$\left(\frac{V_R}{V_{SV}}\right)^6 - 8 \left(\frac{V_R}{V_{SV}}\right)^4 + (24 - 16\alpha^2) \left(\frac{V_R}{V_{SV}}\right)^2 + 16(\alpha^2 - 1) = 0 \quad (2.9)$$

We are now able to find the displacement and velocity of any particle influenced by a Rayleigh wave in an infinite-elastic-isotropic-homogeneous half-space.

The following is a list of the implications of this Rayleigh wave solution:

- The Rayleigh wave is really a grouping of P and SV waves near the surface.
- Rayleigh wave velocity is very close to the S wave velocity and varies with the Poisson's ratio.
- Vertical displacement is 90° off-phase with the horizontal (or radial) displacement.
- Particle Motion is elliptical.
- Particle motion is purely vertical at a certain depth (0.19λ) and ellipticity varies with depth.
- Horizontal and vertical displacement have different amplitudes with depth. And the amplitudes vary with the Poisson ratio.
- The stress profile explains the unique profiles of the vertical and horizontal displacement amplitudes.

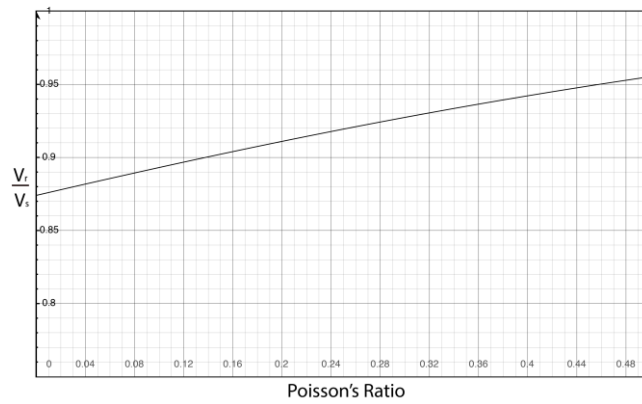


Figure 2.2 - A graph of equation 2.9 showing that the Rayleigh wave to SV wave velocity ratio, with respect to Poisson's ratio.

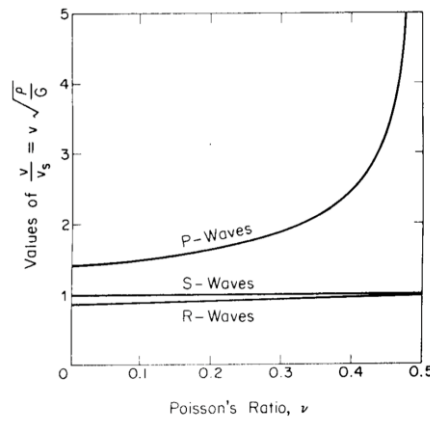


Figure 2.3– P, S, and Rayleigh wave velocities with respect to Poisson's Ratio. Richart, 1970.

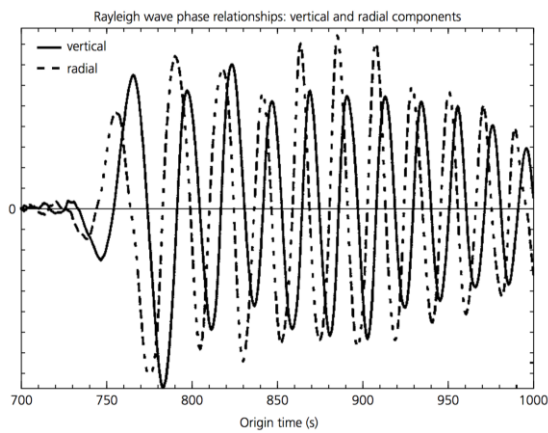


Figure 2.4 - Comparison of vertical and radial Rayleigh wave displacements, showing a 90° phase offset. Stein, 2009.

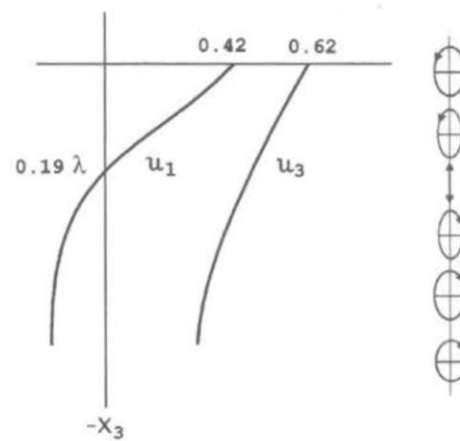


Figure 2.5 - Rayleigh vertical and radial displacements with depth and corresponding elliptical particle motion. Udias, 1999.

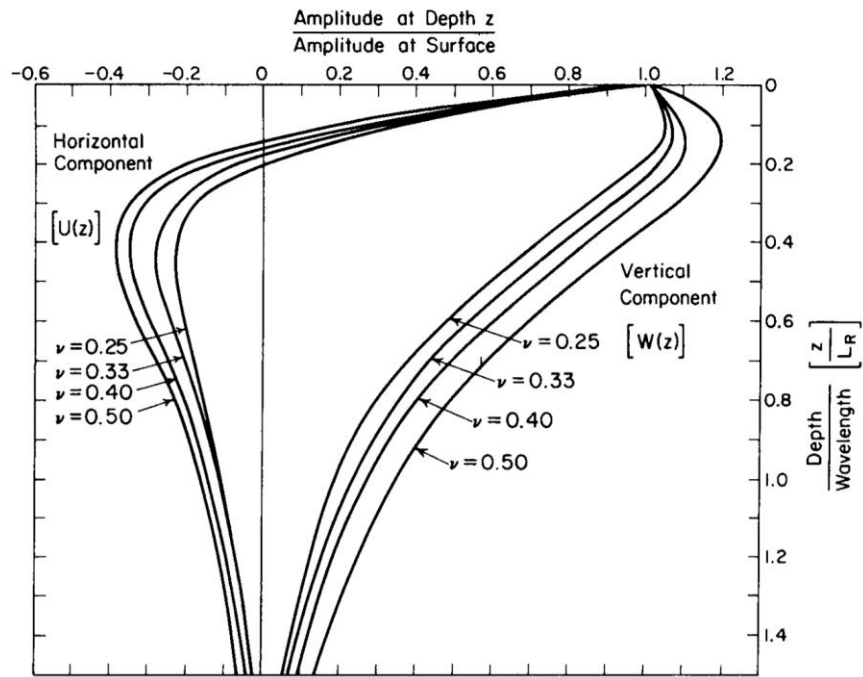


Figure 2.6 - Rayleigh horizontal and vertical particle displacement profiles for a given frequency, showing variation with the Poisson's ratio. Richart, 1970.

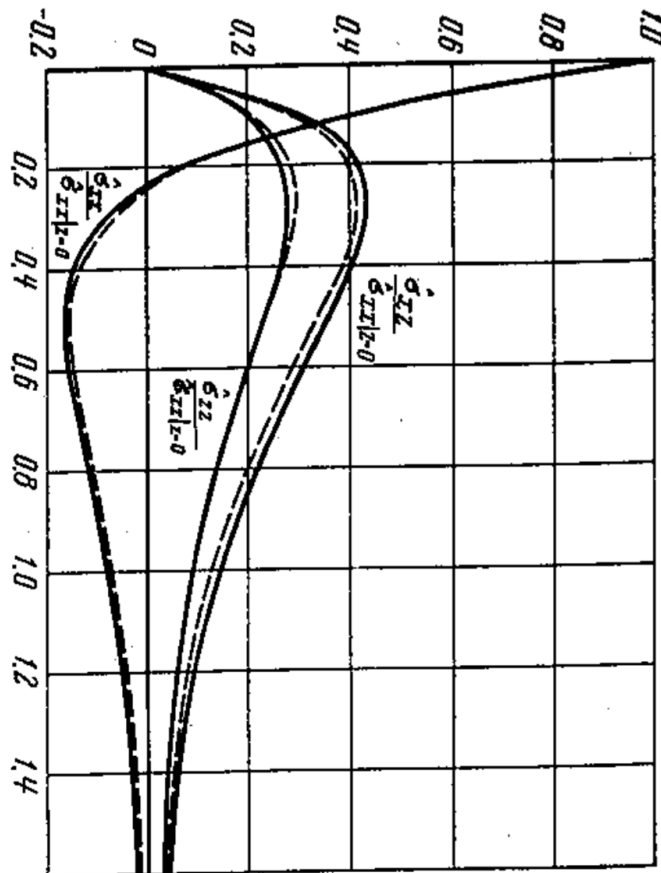


Figure 2.7- Rayleigh wave stress profile. Viktorov, 1967.

## 2.3 Surface Waves in a Layered-Infinite-Elastic-Laterally Isotropic/Homogeneous Half-Space

The introduction of layers introduces three important phenomena, Love waves, normal modes, and dispersion. We will begin this section by reviewing normal mode theory by using the wave solution to a finite elastic rod fixed at both ends. Next the Love wave problem is solved for the simplest two-layer model. And finally, a very brief overview of the Rayleigh wave solution is given as a detailed derivation will be quite lengthy and not necessary for much of the dispersive and modal characteristics are very similar to the Love wave solution. In practice, a layered homogeneous elastic model is a useful approximation for many near-surface situations (Xu et al., 2006).

### 2.3.1 Normal Mode Theory

When elastic waves propagate in a medium with infinite dimensions there exist no modes, and when elastic waves propagate in a medium with finite dimensions, there exist an infinite number of modes. By introducing layers, we effectively create a finite dimension space, and therefore an infinite number of modes.

Let us understand normal mode theory by analyzing vibrations in a finite elastic rod (adapted from Udías, 1999).

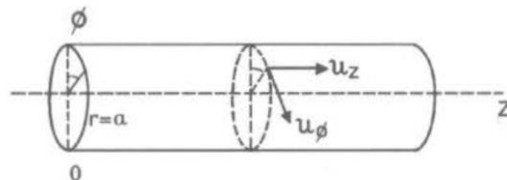


Figure 2.8 - Cylindrical coordinates of an elastic rod. Udías, 1999.

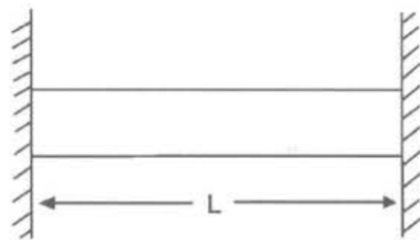


Figure 2.9 - Consider the rod with fixed ends. Udías, 1999.

Consider a finite isotropic-elastic rod where there only exist longitudinal displacements.

$u_z = \text{longitudinal displacement}$

$u_\phi = \text{radial displacement for all angles } \phi = 0$

The normal stress in the longitudinal direction can be written as,

$$\sigma_z = (\lambda + 2\mu) \frac{\partial u_z}{\partial z}$$

We can write the wave equation (in the absence of forces) as,

$$\frac{\partial^2 u_z}{\partial z^2} = \frac{1}{V_p^2} \frac{\partial^2 u_z}{\partial t^2}$$

where,

$$V_p^2 = \frac{(\lambda + 2\mu)}{\rho}$$

The general solution to this wave equation can be written as,

$$u_z = A \sin(kz) \cos(\omega t + \theta)$$

where  $\theta$  is the initial phase. The boundary conditions (both ends fixed) are defined as,

$$u_z(0, t) = 0$$

$$u_z(L, t) = 0$$

and therefore,

$$A \sin(kL) = 0, \quad kL = (n + 1)\pi, \quad \text{for } n = 0, 1, 2, 3 \dots, \infty$$

and finally the solution (for a given mode) is,

$$u_z^n(z, t) = A_n \sin\left(\frac{(n+1)\pi z}{L}\right) \cos(\omega_n t + \theta_n)$$

where,

$$\omega_n = \frac{(n+1)\pi V_P}{L}, \text{ for } n = 0, 1, 2, 3 \dots, \infty$$

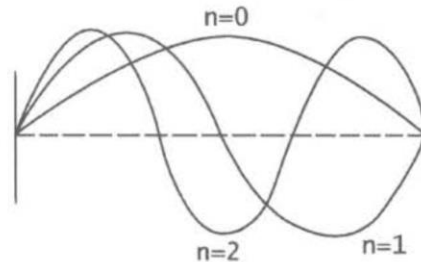


Figure 2.10 – Longitudinal displacement in the rod due to the first three modes, from Udías, 1999.

When  $n$  is equal to 0, this is known as the fundamental mode, and “higher modes” are defined for  $n$  larger than 0. The displacement due to wave motion is now the sum of all the modes. Although the wave equation here is unique to an isotropic-elastic rod, this modal behavior is also seen in surface waves that exist in bounded media.

### 2.3.2 The Love wave

Love waves only exist in layered media, as they essentially consist of SH-waves that are trapped by multiple reflections within layers, where the largest amplitudes exist at the surface. In a two-layer model, Love waves can only occur if the surface layer has a lower velocity than the half space. This section is a review of the Love wave solution for a simple two-layer model.

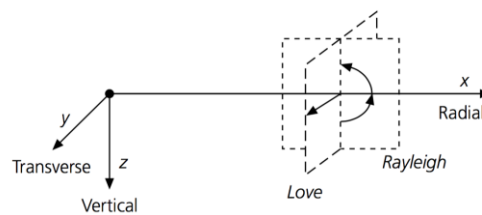


Figure 2.11 – An illustration of the coordinate system and displacements caused by Love and Rayleigh waves. Stein, 2009.

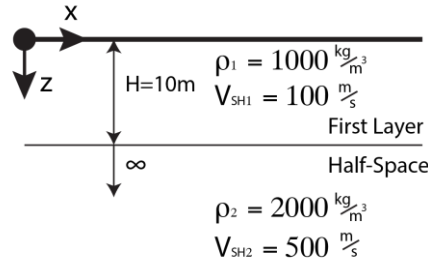


Figure 2.12 - The simple example model used in this derivation of the Love wave.

We can define the Love wave displacement for a wave propagating as,

$$u_y(x, z, t) = V(z)e^{i(k_L x - \omega t)}$$

Now let us consider the wave equations for SH waves (transverse displacement) propagating in the x and z directions for each layer.

$$\frac{\partial^2 u_y}{\partial t^2} = \begin{cases} \frac{G_1}{\rho_1} \left( \frac{\partial^2 u_y}{\partial x^2} + \frac{\partial^2 u_y}{\partial z^2} \right) & \text{for } 0 \leq z \leq H \text{ (first layer)} \\ \frac{G_2}{\rho_2} \left( \frac{\partial^2 u_y}{\partial x^2} + \frac{\partial^2 u_y}{\partial z^2} \right) & \text{for } 0 \geq H \text{ (Half - Space)} \end{cases}$$

Let us define the amplitude  $V(z)$  as the following general solution,

$$V(z) = \begin{cases} A_1 e^{-q_1 z} + B_1 e^{q_1 z} & \text{for } 0 \leq z \leq H \text{ (first layer)} \\ A_2 e^{-s_2 z} + B_2 e^{s_2 z} & \text{for } 0 \geq H \text{ (Half - Space)} \end{cases}$$

where  $q_1$  and  $s_2$  are defined as,

$$q_1 = \sqrt{k_L^2 - \frac{\omega^2}{V_{SH1}^2}}$$

$$s_2 = \sqrt{k_L^2 - \frac{\omega^2}{V_{SH2}^2}}$$

$B_2$  must be 0 since the half space is infinite and there cannot be an up going wave.

Now let us introduce the boundary conditions. We have the following two boundary conditions,

$$\begin{array}{l} \text{At the surface } (z = 0) \\ \text{At infinite Depth } (z = \infty) \end{array} \left\{ \begin{array}{l} \text{There exists no shear stress} \\ \text{There exists no displacement} \end{array} \right.$$

which can be expressed as,

$$\left\{ \begin{array}{l} G \frac{\partial u_y}{\partial z} = \frac{\partial V(z)}{\partial z} e^{i(k_L - \omega t)} = -A_1 q_1 e^{-q_1 z} + q_1 B_1 e^{q_1 z} = (A_1 - B_1) q_1 (e^{-q_1 z} + e^{q_1 z}) = 0 \\ u_y = 0 \end{array} \right.$$

This implies that  $A_1 = B_1$

Now we have,

$$V(z) = \begin{cases} A_1 (e^{-q_1 z} + e^{q_1 z}) & \text{for } 0 \leq z \leq H \text{ (first layer)} \\ A_2 e^{-s_2 z} & \text{for } z \geq H \text{ (half - space)} \end{cases}$$

We can consider two more boundary conditions,

$$\text{At the layer interface } (z = H) \left\{ \begin{array}{l} \text{Shear stress is equal in both layers} \\ \text{Displacement is equal in both layers} \end{array} \right.$$

Let us use the following mathematic identities,

$$2\cos(i\theta) = i(e^{i\theta} + e^{-i\theta}), 2\sin(i\theta) = (e^{i\theta} - e^{-i\theta})$$

Now we can express these two boundary conditions as,

$$\left\{ \begin{array}{l} 2iV_{SH1}^2 \rho_1 A_1 \sin(iq_1 H) = V_{SH2}^2 \rho_2 s_2 A_2 e^{-s_2 H} \\ 2A_1 \cos(iq_1 H) = A_2 e^{-s_2 H} \end{array} \right.$$

Now  $A_2$  can be expressed in terms of  $A_1$  by,

$$A_2 = \frac{2\cos(iq_1 H)}{e^{-s_2 H}} A_1$$

And finally using these relations from the boundary conditions we can write,

$$u_y(x, z, t) = \begin{cases} 2A_1 \cos \left[ \omega \sqrt{\left( \frac{1}{V_{SH1}^2} - \frac{1}{V_{L_n}^2} \right) z} \right] e^{i(k_{L_n} x - \omega t)} & \text{for } 0 \leq z \leq H \\ 2A_1 \cos \left[ \omega \sqrt{\left( \frac{1}{V_{SH1}^2} - \frac{1}{V_{L_n}^2} \right) H} \right] \exp \left[ -\omega \sqrt{\left( \frac{1}{V_{L_n}^2} - \frac{1}{V_{SH2}^2} \right) (z - H)} \right] e^{i(k_{L_n} x - \omega t)} & \text{for } 0 \geq H \\ & \text{for } n = 0, 1, 2 \dots \infty \end{cases} \quad (2.10)$$

This equation gives us the transverse displacement ( $u_y$ ) caused by the Love wave for each mode  $n$ . You can think of this equation as an eigenvalue problem and in order to solve it we must find the eigenvalues ( $V_L$ ) for each mode  $n$  for a given angular frequency  $\omega$  and once we plug this back into the Eigen functions (equation 2.10 for each mode  $n$ ) we obtain a displacement to depth profile for each mode at a particular frequency like in the example shown in figure 13.

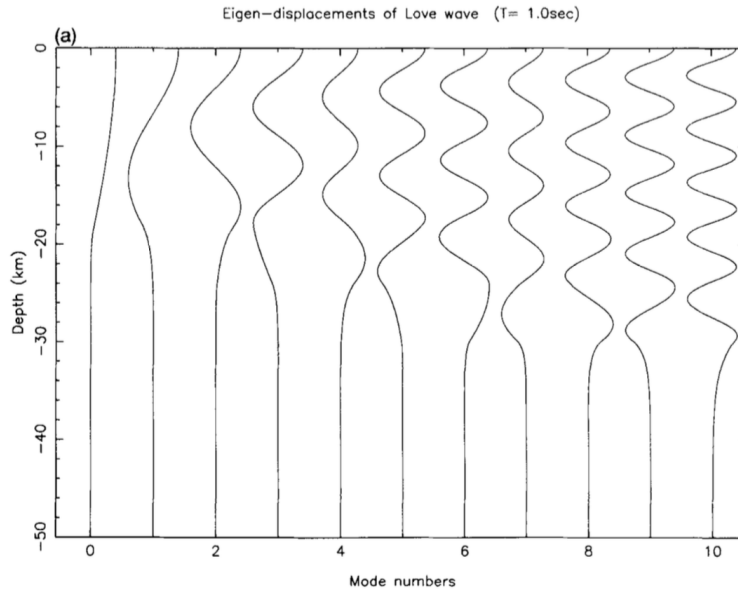


Figure 2.13 - Love wave (normalized) displacement profiles for each mode at a given frequency. From an example model by Chen, 1993. Higher modes travel deeper.

In order to find the eigenvalues ( $V_L$ ) for each mode  $n$  we can use the following relationship, which is the results of setting the determinants equal to zero of the linear system of equations that we obtain by applying the boundary conditions,

$$\tan \left[ \frac{\omega H}{V_{SH1}} \sqrt{1 - \left( \frac{V_{SH1}}{V_L} \right)^2} \right] = \frac{\rho_2 V_{SH2}}{\rho_1 V_{SH1}} \sqrt{\frac{\left( \frac{V_{SH2}}{V_{SH1}} \right)^2 - \left( \frac{V_L}{V_{SH1}} \right)^2}{\left( \frac{V_L}{V_{SH1}} \right)^2 - 1}} \quad (2.11)$$

This is known as the Love-Wave Dispersion Function.

We can see from this equation that only the fundamental mode ( $n = 0$ ) contains velocities at all frequencies. We call the lowest frequency that a higher mode ( $n = 1, 2, 3 \dots \infty$ ) can exist its cutoff frequency. The cutoff frequency for each higher mode can be found using the following relationship,

$$\omega_{c_n} = 2\pi f_{c_n} \frac{n\pi}{H \sqrt{\left( \frac{1}{V_{SH1}^2} \right) - \left( \frac{1}{V_{SH2}^2} \right)}} \text{ for } n = 0, 1, 2 \dots \infty \quad (2.12)$$

Figure 2.14 shows the visualization of the cut off frequencies for the model shown in figure 2.12. Plotting the left-hand and right-hand sides of the dispersion functions allows for a visualization of the solutions to the dispersion function. As evident in figure 2.16, higher frequencies have more modes, and subsequently more roots (or solutions) to the dispersion function, Eq. (2.11).

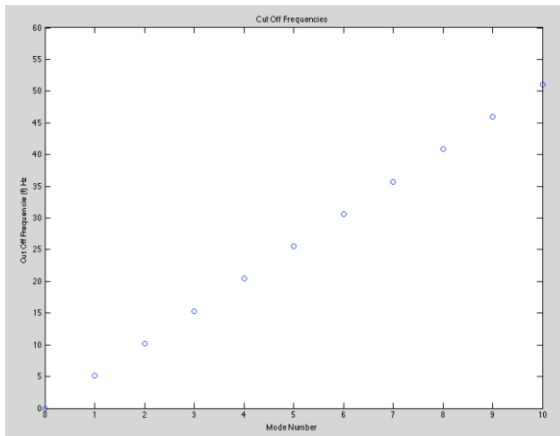


Figure 2.14 - Graph of the Love wave cutoff frequencies.

```
%A MATLAB CODE TO PLOT THE LEFT-HAND AND RIGHT-HAND OF THE LOVE-WAVE
%DISPERSION EQUATION
%BRIAN SHAMS - IAG USP 2015
clear all
%SELECT FREQUENCY
f=20;
w=2*pi*f;
%%%%%%%%%%%%%%%%%%%%%%%%%%%%%%%%%%%%%%%%%%%%%%%%%%%%%%%%%%%%%%%%%%%%%%%%
%MODEL PARAMETERS
vs1=100;vs2=500;
pl=1000;p2=2000;
vL=linspace(0,600,100000);%HERE YOU CAN DEFINE THE NUMBER OF POINTS
H=10;
%%%%%%%%%%%%%%%%%%%%%%%%%%%%%%%%%%%%%%%%%%%%%%%%%%%%%%%%%%%%%%%%%%%%%%%%
%DEFINE LEFT AND RIGHT-HAND
LH=tan((H*w/vs1).*sqrt(1-(vL./vs1).^2));
RH=(p2*vs2)/(pl*vs1)+sqrt(((vs2/vs1)^2-(vL/vs1).^2)./(vL./vs1).^2-1);
%%%%%%%%%%%%%%%%%%%%%%%%%%%%%%%%%%%%%%%%%%%%%%%%%%%%%%%%%%%%%%%%%%%%%%%%
%REMOVE DISCONTINUOUS LINES
for i=1:length(LH)-1
    if sign(LH(i))=1 && sign(LH(i+1))=-1
        LH(i+1)=nan;
    end
    if real(RH(i))=0
        RH(i)=nan;
    end
end
%%%%%%%%%%%%%%%%%%%%%%%%%%%%%%%%%%%%%%%%%%%%%%%%%%%%%%%%%%%%%%%%%%%%%%%%
%PLOT
plot(vL,LH,vL,RH)
legend('Left-Hand','Right-Hand')
title(['Left-Hand and Right-Hand of Love Wave Dispersion Function at F=' num2str(f) ' Hz'])
xlabel('Love Wave Velocity')
ylabel('Value of Left-Hand and Right-Hand of Dispersion Function')
%%%%%%%%%%%%%%%%%%%%%%%%%%%%%%%%%%%%%%%%%%%%%%%%%%%%%%%%%%%%%%%%%%%%%%%%
```

Figure 2.15 - MATLAB® code written to display the left-hand and right-hand sides of the dispersion function, Eq. (2.11).

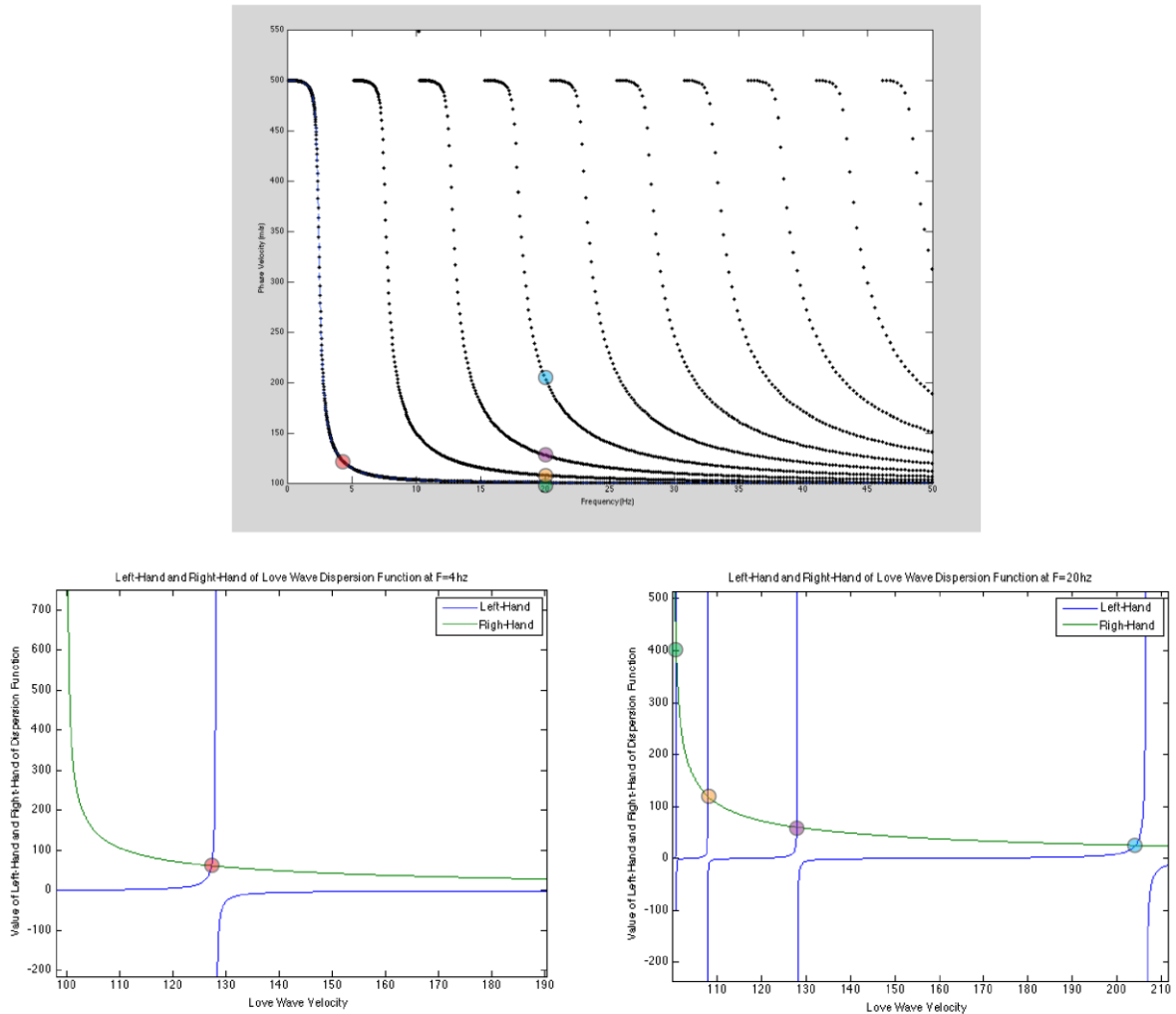


Figure 2.16 - A visualization of the left-hand and right-hand sides of the Love wave dispersion function (bottom left and right) at a particular frequency. The love wave dispersion curves are shown for the model shown in figure 2.12 (Top); the curves represent the solutions to the dispersion function at each frequency.

### 2.3.3 The Rayleigh wave

In the previous section the Love wave problem was solved for a simple two-layer model. However, to solve even a simple two-layer Rayleigh wave problem considerably more effort is involved. Because Love wave dispersion and modal behavior is very similar to that of Rayleigh waves and as the purpose of this section is to demonstrate the dispersive and modal characteristics of Rayleigh waves in layered media, the majority of the derivation will be bypassed and rather the most important characteristics of Rayleigh waves in layered media will be discussed.

The Rayleigh eigenvalue problem is more complicated to solve because it involves both P and SV waves, which are the two waves that essentially constitute a Rayleigh wave. The most common way to solve it is by the transfer matrix method, after Thomson (1950) and Haskell (1953) (Pei, 2007). However, there are other alternative matrix methods such as the stiffness matrix method after Kausel and Roesset (1981) and the reflection-transmission coefficient matrix method after Kennet (1984) and Luco and Aspel (1983). Numerical methods such as finite-element method (Lysmer and Drake, 1972), finite-difference method (Boore, 1972), and numerical integral method (Takeuchi and Saito, 1972) can also solve the Rayleigh eigenvalue problem (Pei, 2007). A detailed derivation of the Rayleigh wave problem can be found in many seismology textbooks such as Aki & Richards (1980).

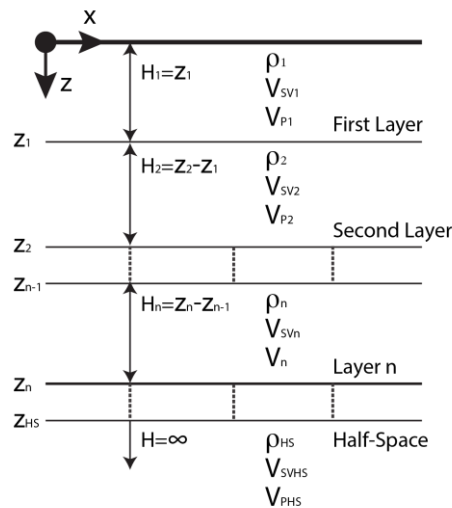


Figure 2.17 - A visualization of a two-dimensional layered model, used for surface wave modeling.

We start exactly the same as the homogeneous case defining displacements,

$$u_x = \frac{\partial \Phi}{\partial x} + \frac{\partial \Psi}{\partial z}$$

$$u_z = \frac{\partial \Phi}{\partial z} - \frac{\partial \Psi}{\partial x}$$

where the harmonic functions  $\Phi$  and  $\Psi$  are defined as,

$$\Phi = (A_1 e^{-qz} + B_1 e^{qz}) e^{i(\omega t - k_R x)}$$

$$\Psi = (A_2 e^{-sz} + B_2 e^{sz}) e^{i(\omega t - k_R x)}$$

where  $q$  and  $s$  are defined as,

$$q = \sqrt{k_R^2 - \frac{\omega^2}{v_P^2}}$$

$$s = \sqrt{k_R^2 - \frac{\omega^2}{v_{SV}^2}}$$

We cannot ignore  $B_1$  because it represents a reflected wave traveling upward, and we can only ignore  $B_2$  when it is representing the half-space. Also we will have to solve these equations at each layer interface, so we will re-write it in a form per layer.

$$\Phi_n = (A_n e^{-q_n(z-z_{n-1})} + B_n e^{q_n(z-z_{n-1})}) e^{i(\omega t - k_R x)}$$

$$\Psi_n = (C_n e^{-s_n(z-z_{n-1})} + D_n e^{s_n(z-z_{n-1})}) e^{i(\omega t - k_R x)}$$

$$q_n = \sqrt{k_R^2 - \frac{\omega^2}{v_{Pn}^2}}$$

$$s_n = \sqrt{k_R^2 - \frac{\omega^2}{v_{SVn}^2}}$$

Let us consider the following boundary conditions,

- 1) Stresses  $\sigma_z$  and  $\tau_{xz}$  are zero at the surface.
- 2) Displacements  $u_x$  and  $u_y$  are zero at infinite depth.
- 3) Stresses  $\sigma_z$  and  $\tau_{xz}$  are the same for both layers at an interface.
- 4) Displacements  $u_x$  and  $u_y$  are the same for both layers at an interface.

And eventually we can derive the following vector expressions for the displacements and stresses in each layer,

$$u_{x_n} = \begin{bmatrix} B_n e^{q_n(z-z_{n-1})} \\ D_n e^{s_n(z-z_{n-1})} \\ A_n e^{-q_n(z-z_{n-1})} \\ C_n e^{-s_n(z-z_{n-1})} \end{bmatrix} [ik_R \quad -s_n \quad ik_R \quad s_n] e^{i(\omega t - k_R x)}$$

$$u_{y_n} = \begin{bmatrix} B_n e^{q_n(z-z_{n-1})} \\ D_n e^{s_n(z-z_{n-1})} \\ A_n e^{-q_n(z-z_{n-1})} \\ C_n e^{-s_n(z-z_{n-1})} \end{bmatrix} [q_n \quad ik_R \quad -q_n \quad ik_R] e^{i(\omega t - k_R x)}$$

$$\sigma_{z_n} = \begin{bmatrix} B_n e^{q_n(z-z_{n-1})} \\ D_n e^{s_n(z-z_{n-1})} \\ A_n e^{-q_n(z-z_{n-1})} \\ C_n e^{-s_n(z-z_{n-1})} \end{bmatrix} [\mu_n(2k_R^2 - k_{SV_n}^2) \quad 2i\mu_n s_n k_R \quad \mu_n(2k_R^2 - k_{SV_n}^2) \quad -2i\mu_n s_n k_R] e^{i(\omega t - k_R x)}$$

$$\tau_{xz_n} = \begin{bmatrix} B_n e^{q_n(z-z_{n-1})} \\ D_n e^{s_n(z-z_{n-1})} \\ A_n e^{-q_n(z-z_{n-1})} \\ C_n e^{-s_n(z-z_{n-1})} \end{bmatrix} [2i\mu_n q_n k_R \quad -\mu_n(2k_R^2 - k_{SV_n}^2) \quad -2i\mu_n q_n k_R \quad -\mu_n(2k_R^2 - k_{SV_n}^2)] e^{i(\omega t - k_R x)}$$

We can now develop these vectors into a matrix eigenvalue problem, and eventually find the values to  $A_n$ ,  $B_n$ ,  $C_n$ ,  $D_n$  and consequently the displacements and velocities for each layer. And we see the similar dispersive and modal behavior as seen in Love waves.

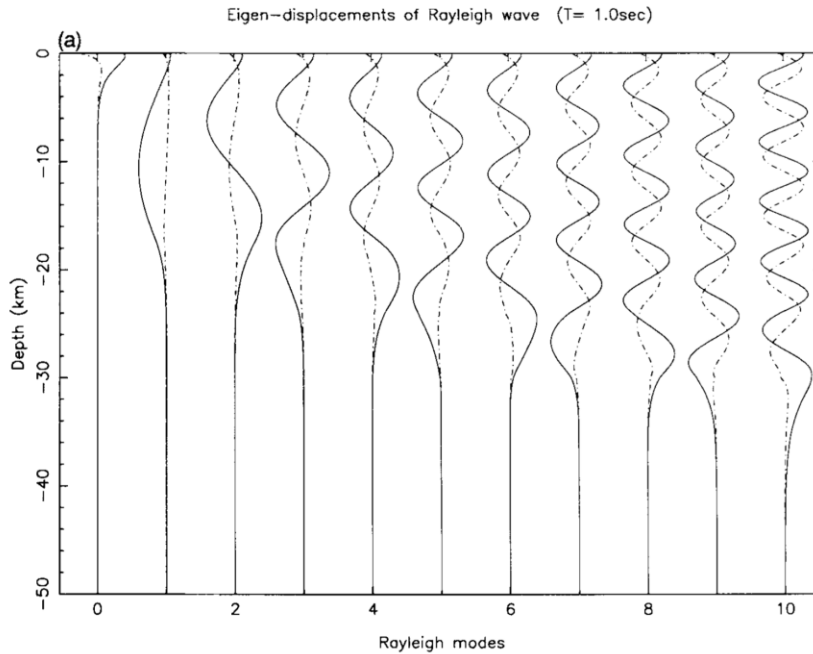


Figure 2.18 – Rayleigh wave displacement profiles for both vertical (solid) and horizontal (dotted) components for each mode at a given frequency. From an example model by Chen, 1993.

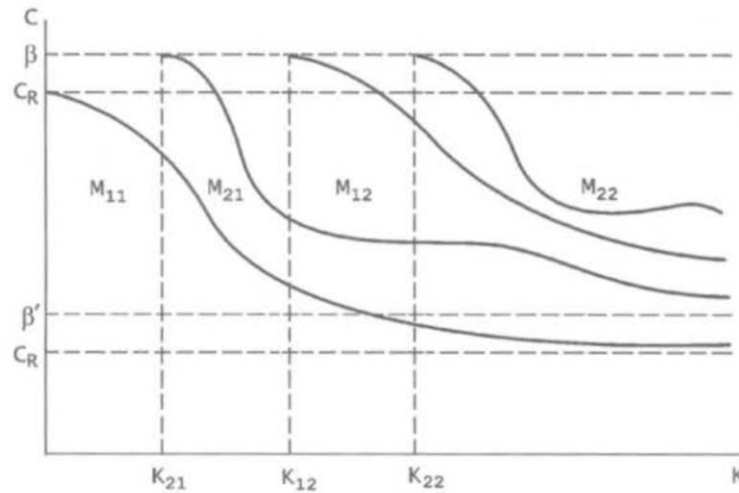


Figure 2.19 – Rayleigh wave dispersion curves for the fundamental mode (shown as  $M_{11}$ ) and three higher modes. The vertical axis is the Rayleigh wave phase velocity ( $V_R$ ) and the horizontal axis is frequency. The ranges for the SV wave velocity (shown as  $\beta$ ) and the Rayleigh wave phase velocity (shown as  $C_R$ ) are shown. The cutoff frequencies are also shown as  $K_{21}$ ,  $K_{12}$ ,  $K_{22}$ . From Udías, 1999.

## 2.4 Seismic Methods

### 2.4.1 Refraction WET Tomography

The foundations of the general theory of tomography can be found in work of J. Radon (1917) and applied by A. Cormack in 1963 (Udías, 1999), and has since been used in many fields. Seismic tomography applied to study the Earth's interior was developed in the mid-1970s (aki et al., 1976, apud Udías, 1999). Refraction tomography techniques are essentially travel time tomography methods applied to refracted waves. As with the finite element method, tomography separates a region into blocks or sub-regions, and in the case of travel time tomography the residual (or difference) of the observed and modeled wave arrival times at each sub-region is the object of the inversion process. Since observed data is typically only available on the surface, the aim of travel time tomography is to explain the residuals (or incoherence between the model and observed data) through velocity distribution inside the earth, where a higher concentration of ray paths adds more confidence.

Refraction tomography is based on an iterative process. First an initial model of seismic velocities is generated in accordance with the source/geophone arrangement employed to record the refracted waves. Subsequently, an inversion algorithm seeks to minimize the difference of the residuals by making adjustments to the model until a solution is found, be it local or global.

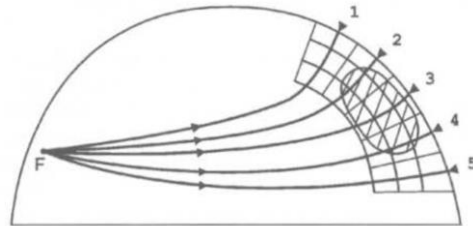


Figure 2.20 – Ray paths crossing a gridded region in a study of seismic tomography of the earth. Residuals are only obtainable between ray paths, so outside points are not invertible. From Udias, 1999.

Refraction tomography is not subject to the same constraints imposed by the simplifying assumptions of conventional refraction methods such as the delay time and generalized reciprocal methods; refraction tomography performs well in many situations where conventional methods fail, e.g., where lateral or vertical gradients compose a significant component of the velocity structure (Sheehan et al., 2005).

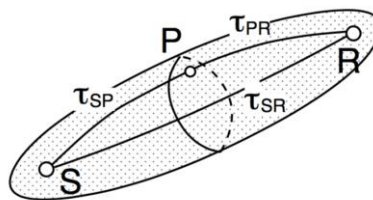


Figure 2.21 – A schematic representation of a Fresnel volume with a source (S) and a receiver (R), from Watanabe, 1999.

In this research Rayfract® is used as the software for processing refraction data. Rayfract® employs the wavepath eikonal travel time inversion method (WET) (Schuster & Quintus-Bosz, 1993) by calculating the travel times from the finite difference of the eikonal first order equation proposed by Lecomte et al. (2000) and using the Fresnel volume approach proposed by Watanabe et al. (1999). A Fresnel volume considers not only the ray path as influencing the seismic signal recorded by a geophone but also takes into account the structure around the ray path. For this work, Rayfract’s “smooth inversion” algorithm is used for all WET tomography inversions; this algorithm creates a one dimensional initial model based on the Delta-t-V (Rohdewald, n.d.) inversion results and smooths it to remove artifacts (Sheehan et al., 2005).

### 2.4.1.1 Field Measurements

Refraction data is typically collected by a linear spread of geophones on the earth surface recording seismic data originating from an active source (in the case of this research, a sledgehammer). In order to obtain the maximum amount of information from a survey it is necessary to collect data from a variety of shot (or source) locations. Rayfract® recommends at least one shot per every sixth receiver in an array for a reliable WET tomography inversion.

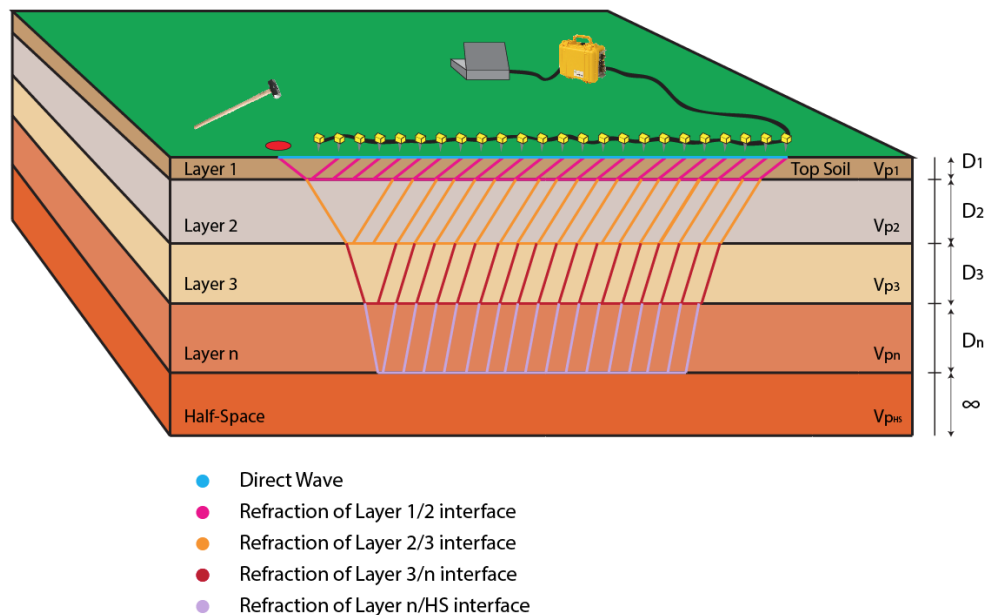


Figure 2.22 –An illustration of a refraction site investigation with a linear array of geophones and a sledgehammer as an active source. Note that not all refraction interpretation methods required idealized flat layering as shown.

## 2.4.2 MASW

The multichannel analysis of surface waves (MASW) method, first introduced by Park et al. (1999), is a seismic method which exploits the dispersive nature of Rayleigh waves (in layered media) to invert a one-dimensional model of the earth (that can be interpolated into a two-dimensional profile) in terms of the P wave velocity, SV wave velocity, density, and thickness of each layer. The MASW method is most commonly used with a linear geophone array, as shown in Figure 2.23, with an active source such as a sledgehammer. However, roadside and passive MASW surveys are also common, where a two-dimensional array is preferable for passive surveys to accurately locate the source azimuth. And although MASW is typically used to record the more energetic vertical component of the Rayleigh wave, it can be equally effective in measuring the horizontal (or radial) component, which may be useful in further defining the fundamental or higher modes. It is also important to note that there exist a variety of ways to analyze surface waves by measuring seismic wave arrivals using an array of geophones, and therefore the term MASW will be used exclusively in referring to the general procedure of Rayleigh wave analysis used by Park et al. (1999) and implemented by the commercial software packages SurfSeis© v.4 and ParkSEIS© v.1.

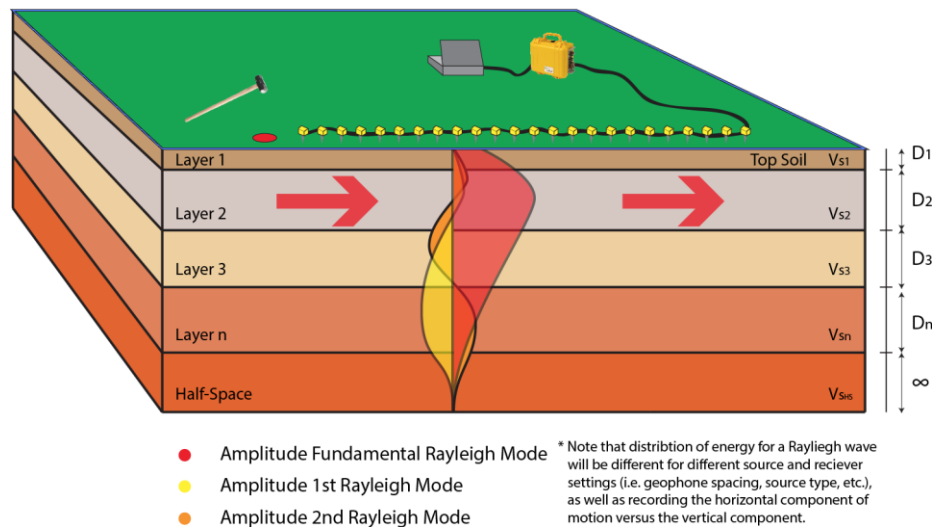


Figure 2.23 – An illustration of an active source MASW field survey using a linear geophone array. Note that Rayleigh waves in layered media will exhibit dispersive and modal behavior, and that the Rayleigh wave amplitudes are not to scale, and will vary with different site characteristics.

### 2.4.2.1 Field Measurements

The first step to the MASW method is the field survey. There are a couple of key parameters to consider.

- Geophone Type
- Number of Geophones
- Geophones Spacing
- Array Length
- Source Offset
- Source Type

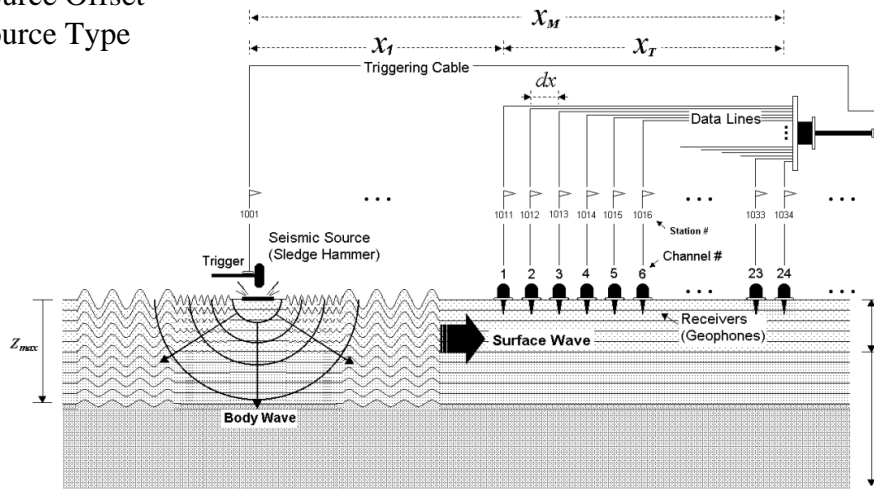


Figure 2.24 – An illustration of the field parameters for a MASW survey, from Penumadu, 2005.

Material Type* ( $V_s$ in m/sec)	$x_1$ (m)	$dx$ (m)	$x_M$ (m)	Optimum Geophone (Hz)	Optimum Source* (Kg)	Recording Time (ms)	Sampling Interval (ms)
<b>Very Soft</b> ( $V_s < 100$ )	1 – 5	0.25 – 0.5	$\leq 20$	4.5	$\geq 5.0$	1000	1.0
<b>Soft</b> ( $100 < V_s < 300$ )	5 – 10	0.5 – 1.0	$\leq 30$	4.5	$\geq 5.0$	1000	1.0
<b>Hard</b> ( $200 < V_s < 500$ )	10 – 20	1.0 – 2.0	$\leq 50$	4.5 – 10.0	$\geq 5.0$	500	0.5
<b>Very Hard</b> ( $500 < V_s$ )	20 – 40	2.0 – 5.0	$\leq 100$	4.5 – 40.0	$\geq 5.0$	500	0.5

\* Average properties within about 30-m depth range

+ Weight of sledge hammer

Table 2.1 - A table showing the recommended field parameters for MASW surveys by the KGS, from Penumadu, 2005.

### **Geophone Type:**

Geophones manufactured with a lower natural frequency have the advantage of effectively recording lower frequency components of surface waves, however geophones are not limited by their natural frequency and many observations have been made of frequencies as low as 5 Hz for 10-Hz geophones and down to 10 Hz for 40 Hz geophones (Park et al., 2002). The lower the seismic velocity of the material (i.e. the softness), the more important it is to have a lower frequency geophone (see Table 2.1). Typically, geophones with natural frequencies lower than 4.5 Hz are not used, as costs tend to increase exponentially for geophones with natural frequencies lower than the relatively common 4.5 Hz.

### **Number of Geophones:**

In a two station (or geophone) survey (i.e. SASW) the geophone spacing determines both the maximum recordable wavelength and the minimum recordable wavelength; in other words, two station surveys can record only one wavelength. With the multichannel approach (MASW), there are a variety of recordable wavelengths as there are a variety of geophone distances to consider. The larger the number of geophones the larger the variety of recordable wavelengths. However, a higher number of geophones alone does not increase the resolution of the dispersion image; this is only achieved by a longer array length (or spread length), which may or may not include more geophones (Park et al., 2001). Ultimately, the chosen geophone spacing and array length are what should determine the number of geophones.

### **Geophone Spacing:**

Because MASW survey arrays typically have evenly spaced geophones, the spacing between each geophone essentially determines the minimum recordable wavelength and therefore the minimum invertible depth. Typical values recommended by the KGS range anywhere between 0.25 m for very shallow surveys and up to 5 m for deeper surveys (Table 2.1).

### **Array Length:**

The length of the array determines the largest recordable wavelength of the survey, and consequently the depth of investigation. Furthermore, the resolution of a dispersion image at a given frequency is directly proportional to the product of the length of the geophone array and the frequency (Xia et al., 2005). However, the longer the array length, the greater the area that is assumed to be laterally homogeneous (this is due to the fundamental assumption of the two-dimensional Rayleigh wave forward modeling schemes that assume a layered medium). Therefore, if a site is known to vary laterally a long array is not recommended, however the maximum depth will be sacrificed with shorter array lengths.

The dispersion image resolution is given by the following equation (Xia et al., 2005),

$$\Delta d = 1/(f \times x_T)$$

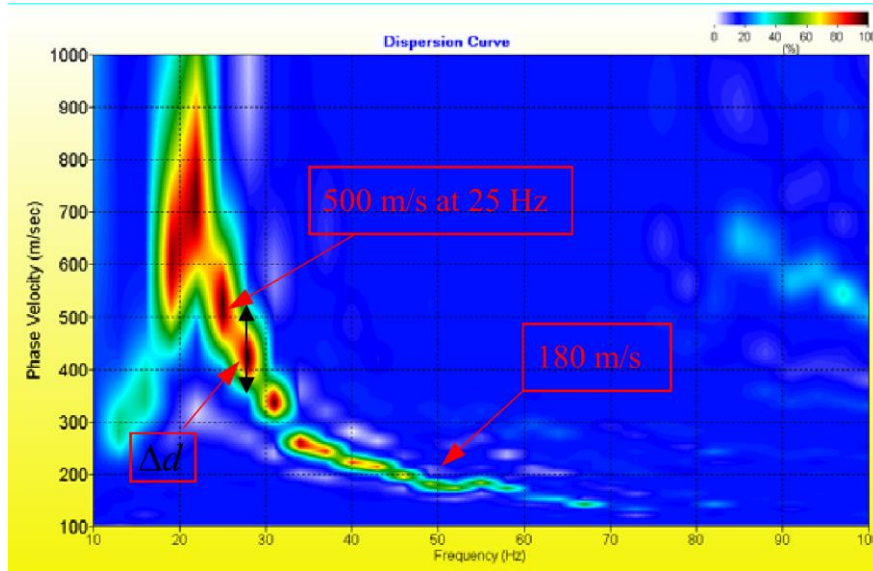


Figure 2.25 - A dispersion image illustrating the phase velocity resolution ( $\Delta d$ ), from Xia et al., 2005.

### Source Offset:

Rayleigh waves require a certain distance to form; this is because a Rayleigh wave is essentially a grouping of P and SV waves that form as a result of interactions at the surface interface. The nearest offset from a source that is sufficiently far away to where a Rayleigh wave can be generated in a simplified two-layered model is given by equation 2.13 (Xia et al., 2005).

$$x_{1(min)} = \frac{2h}{\sqrt{(V_P/V_{SV})^2 - 1}} \quad (2.13)$$

This equation clearly shows how the distance to which a Rayleigh wave is generated is related to not just the velocities of the first layer ( $V_P$  &  $V_{SV}$ ) but also the thickness ( $h$ ) of the first layer. If we assume that  $V_P/V_S$  is equal to 4, then we see that the minimum offset is about  $h/2$  or 50% of the depth to the half-space (or maximum depth of investigation). This is a good rule of thumb to consider when determining the minimum source offset, and although equation 2.13 is based on a two-layer model, it is also valid for a multi-layer model because the reflected P wave energy from the interface of the first two layers always interferes with the direct S wave energy first (Xu et al., 2006).

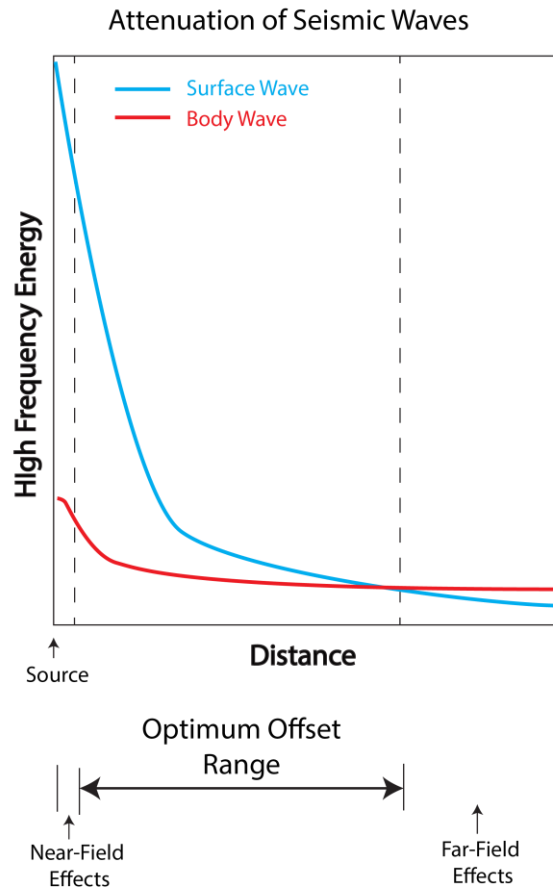


*Figure 2.26 – An illustration of the optimum offset range and how body waves eventually dominate energy of high frequencies after a certain distance. Modified from the short course notes of SurfSeis© by the KGS.*

Park et al. (1999) defines the near-field effects as the effects which do not allow Rayleigh waves to travel as horizontal plane waves near the source; and likewise, the far-field effects are defined as the rapid attenuation of high frequency surface wave energy with distance (see Figure 2.26), eventually allowing body wave energy to dominate. The recommended best practice is to pick a source offset range that is greater than the minimum offset (i.e. approximately  $0.5 \times z_{max}$  in most cases) and is not too long that will cause far-field effects; the recommended source offsets in Table 1 can be used to avoid far-field effects in most conditions.

### **Source Type:**

There are a variety of sources available to process surface wave data. In general, sources can be divided into passive and active, where passive sources derive from events which induce ground vibrations that are not purposely intended for the survey, and active sources are sources of energy which originate from a purposeful release of energy into the ground to induce vibration. Typical examples of passive sources include vehicle traffic, construction work, ocean waves, etc., and typical examples of active sources include sledgehammer impacts, explosion charges, weight drops, etc. Sledgehammer sources are perhaps the most common type of active source due to the relative ease and cost of use. Park et al. (2002) showed that although a 20-lb sledgehammer source obtained slightly lower frequency surface wave energy as compared to a 10-lb sledgehammer, a rubber-band-aided weight drop with more impact energy actually increased the higher frequency surface wave energy at a particular site. Thus, an increase of impact strength does not necessarily increase the amount of surface wave energy at lower frequencies (Park et al., 2002).

### **2.4.2.2 Data Processing**

Before the conversion of multichannel records into dispersion images (through slant-stack processing) we can improve the seismic data by muting, automatic gain control, and/or filtering (Yilmaz, 2001). MASW data processing is essentially the conversion of seismic multichannel records (or seismograms) into dispersion images (or overtones). There exist a variety of methods to perform this conversion, such as the pi-omega transformation (McMechan and Yedlin, 1981). However, MASW implements the phase-shift method (Park et al., 1998), which achieves a higher resolution than the pi-omega method (Park et al. 1998).

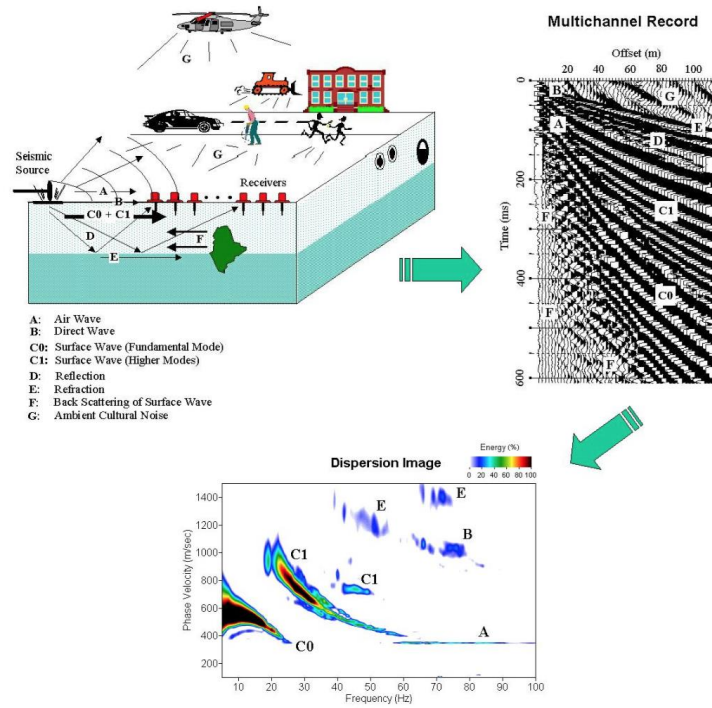


Figure 2.27 – A visualization of the site investigation, multichannel record, and dispersion image that is an output of MASW data processing, from Park, 2005.

### 2.4.2.3 Curve Picking

The next step is to use the dispersion image to accurately find and select points that lie on the dispersion curve of the fundamental mode (and possibly higher modes) of the Rayleigh wave.

This is perhaps the most controversial aspect of MASW as it introduces unquantifiable human error into the process. An experienced user of the MASW method will recognize certain patterns in the dispersion images and with time confidence can build in the curve selection process, however the biggest challenge is the unpredictable site response. It has become evident through modeling that the fundamental mode is not necessarily the dominating mode and the continuity of a signal in the dispersion image does not necessary mean that it belongs to a single mode (Moro, 2015).

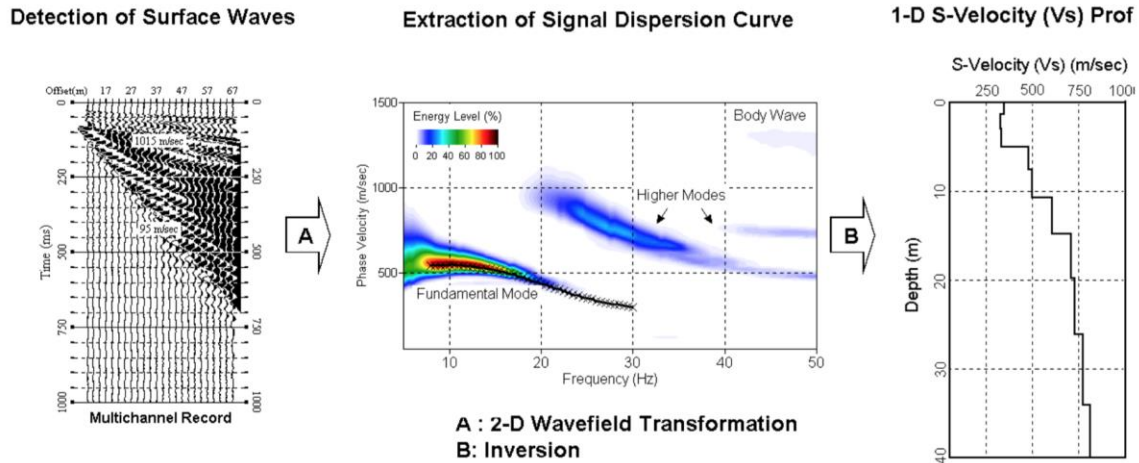


Figure 2.28 – An illustration of the 3-step procedure after field measurements, data processing, curve fitting, and inversion. Note that here only the fundamental mode has been picked and used for inversion, from Park et al., 2004.

### 2.4.2.4 Inversion

The forward modeling algorithms for both SurfSeis© and ParkSEIS© are based on Schwab and Knopoff (1972), which itself is based on the transfer matrix method of Thomson (1950) and Haskell (1953). Although SurfSeis© is capable of multi-mode inversion, it is typically used for fundamental mode inversion as energy is usually concentrated in that mode, making it easier to pick. Furthermore, the fundamental mode always has the lowest Rayleigh wave phase velocities and is the only mode to exist at all frequencies, distinguishing it even further from the other modes.

The inversion algorithms differ between SurfSeis© and ParkSEIS©. The algorithm for SurfSeis© is based on Xia et al. (1999) whereas the ParkSEIS© algorithm has not been published. Both software packages allow the user to modify certain settings in the inversion process, but neither allow modifications to the objective function.

The MATLAB® code written for this research performs inversion using MATLAB’s built in minimizer functions such as `fmincon` and `fminsearch`. In this code, the objective function is defined as the Euclidian distance between the picked dispersion curve and a dispersion curve that varies with each iteration as parameters are adjusted until a minimum is reached.

$$obj\ func = \min\{\|Picked\ Disp\ Curve - Variable\ Disp\ Curve\|^2\} \quad (2.14)$$

### 2.4.3 Love Wave Analysis

The multichannel analysis of love waves is essentially equivalent to the MASW method that is used for Rayleigh waves. However, presumably because SH wave generation is more difficult and SH refraction surveys seldom performed, neither SurfSeis© nor ParkSEIS© contain the forward modeling algorithm (also found in Schwab and Knopoff, 1972) for Love waves, and therefore are incapable of inverting for them. However, theoretically these two software packages are useful up until the inversion process (i.e. extracting a dispersion image from a multichannel record and picking the fundamental dispersion curve). Once a dispersion curve has been picked from a Love wave dispersion image, it can be inverted in an inversion algorithm that can be implemented in any computer language. The author has created a MATLAB® code which can invert Love wave fundamental mode dispersion curves as well as that of the Rayleigh wave for simplified two-dimensional layered homogeneous isotropic models.

## Chapter 3 - Area of Study

In the large scale, the area of study is situated on the Campos do Jordão plateau, a high elevation land mass located near the southeastern border of the Mantiqueira mountain range (Serra da Mantiqueira), Brazil. The Mantiqueira mountain range reaches a maximum elevation of 2,798 meters at Pedra da Mina peak, however the immediate region of the site of investigation averages around 1,700 meters in elevation.

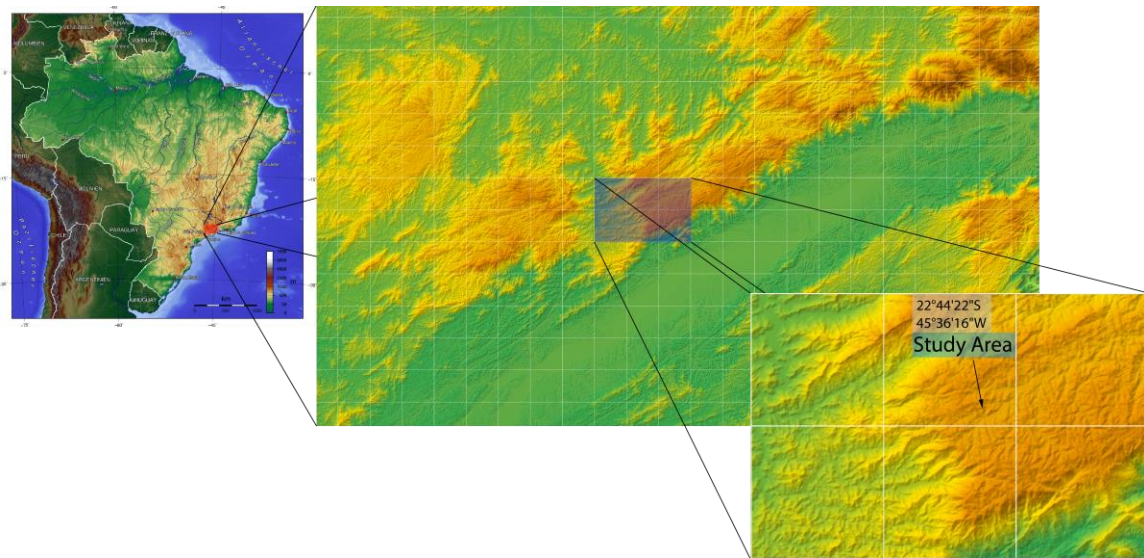


*Figure 3.1 – Visualization of the area of study using data from a digital elevation model via NASA Shuttle Radar Topography Mission Global 30m (SRTM\_GLI).*

In the medium scale, the area of study is located in the low income housing neighborhood of Santo Antônio, a part of the city of Campos do Jordão in the state of São Paulo. The neighborhood has seen a sharp rise in the number of inhabitants and homes since the 1970s (see figure 3.2, right side) as the region has developed into a popular tourist destination for Brazilians. Despite very expensive housing development in large parts of the city, the population found in this neighborhood is predominantly low income and live in poor housing conditions, which is typically a result of initially unauthorized land use which was later legalized by the government. As a result, the steep terrain is improperly occupied, where cuts and landfills are often carried out by the residents themselves, often resulting in precarious and dangerous slope stability issues (Ahrendt, 2005).

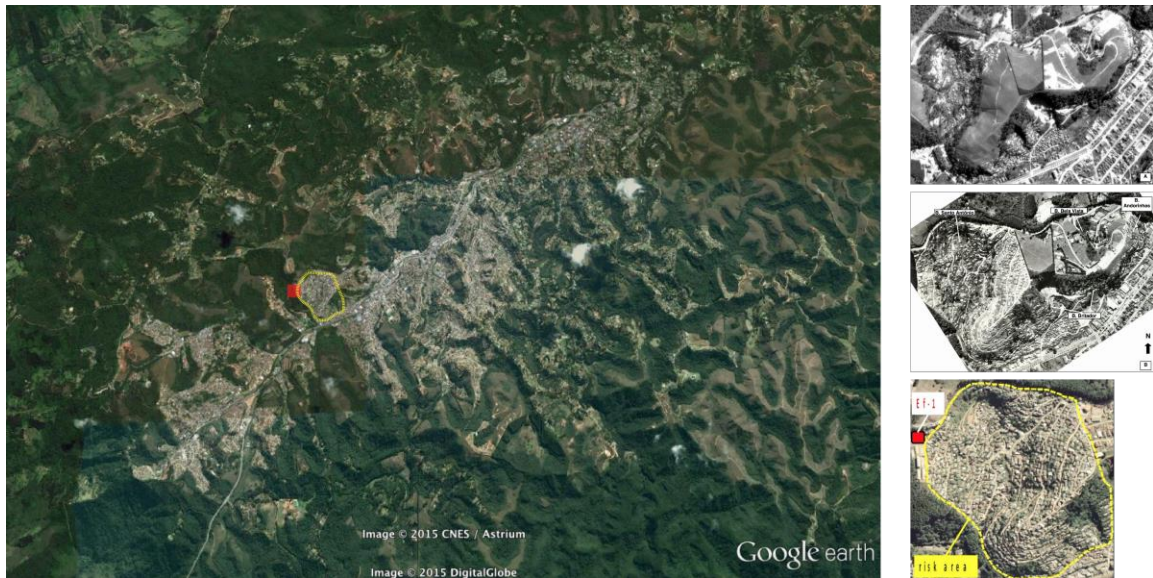


Figure 3.2 – A recent satellite image of the city of Campos do Jordão (left) from Google Earth, with the neighborhood of Santo Antônio circled in yellow and the site of investigation represented by a red square. Images of Santo Antônio from 1972 (top right), 1982 (right center) (Ahrendt, 2005) and recently (bottom right) (Mendes et al., 2015) show the rapid development of the region. Note that north is pointing up in all images.



Figure 3.3 - A panoramic view of a section of the Santo Antônio neighborhood, from Ahrendt, 2005.

In the small scale, the area of study is located to the far west side of Santo Antônio, between a building which is currently managed by a local university and a caged weather monitoring station used previously by the Geological Institute (IG) of the state of São Paulo. The site was chosen because it sits on a relatively stable slope for the safety of personnel, and because it shares many geological characteristics with nearby areas where landslides have previously occurred. Due to these characteristics, a geotechnical investigation was conducted at the site by Mendes et al. (2015). The site is located less than 200 meters from an area known to have suffered from landslides during the region's infamous landslide event of the 1999-2000 winter.



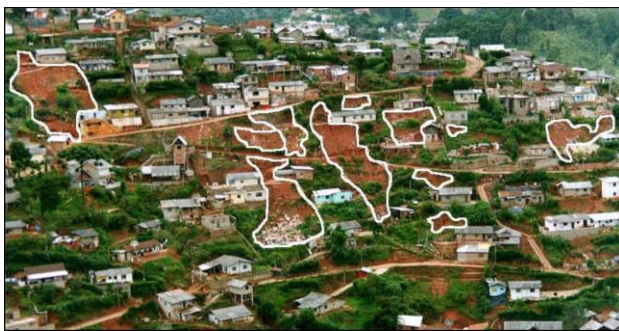
Figure 3.4 – A Google Earth satellite image of the site of investigation. The geophone array is represented by the yellow line, the caged monitoring station by the red box, and the orange circle represents the location where the passive MASW survey was performed.



Figure 3.5 – Images of the site of investigation. An image of the west side of Santo Antônio from the valley floor pointing to the caged monitoring station in red (top left), from Mendes et al. (2015). Two images of the site during MASW and refraction surveying (top right and bottom).

### 3.1 Landslide History and Data

Santo Antônio and nearby neighborhoods were devastated after widespread landslides destroyed many homes between December 1999 and January 2000 after heavy rainstorms hit the region. The disaster became the focus of many research efforts afterwards (Ahrendt, 2005; Mendes 2012; Mendes et al., 2015). These research efforts have resulted in some valuable information, however a detailed near surface velocity profile has yet to be available. The landslides which occurred during this event were very shallow, generally being less than a meter deep (Ahrendt, 2005).



*Figure 3.6 – The aftermath of landslides in the neighborhood of Santo Antônio during the winter of 1999-2000, from Ahrendt, 2005.*

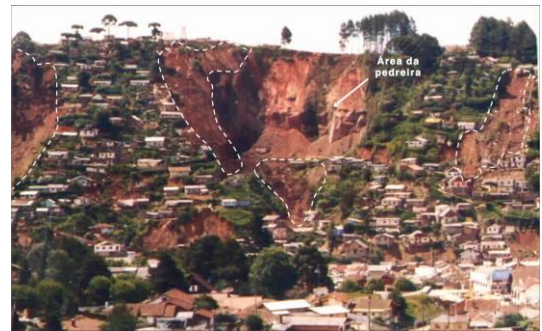


*Figure 3.7 – Some of the most devastating landslides occurred in the nearby neighborhood of Britador. From Ahrendt, 2005.*



*Figure 3.8 – Shallow landslides that occurred in the Santo Antônio neighborhood of Campos do Jordão, here within 200 meters of the site of investigation. From Ahrendt, 2005.*

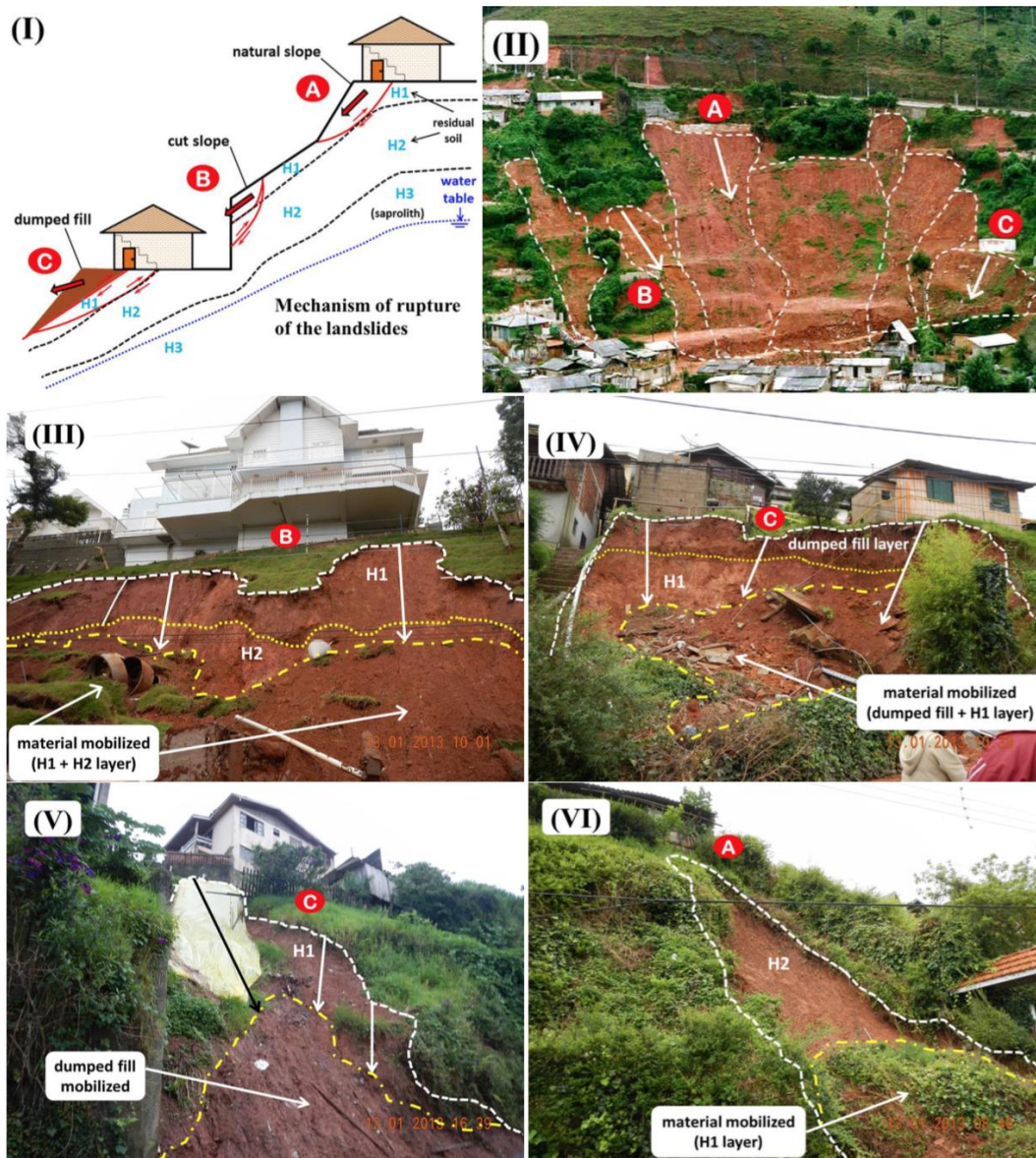


Figure 3.9 – Images of landslides which occurred in the city of Campos do Jordão in January, 2000. The diagram (I) shows the shallow nature of the landslides, where the slip surface is confined to the top two residual soil layers (Mendes et al., 2015; original source: Geological Institute of the state of São Paulo).

### 3.2 Geological Information

The Mantiqueira mountain range is geologically old, dating to the Precambrian and the Paleozoic (Modesi, 2010). The predominant geology of Campos do Jordão includes metamorphic rocks such as migmatites, gneisses, metadiorite, and granulites; and there also occur schists, quartzites, and metaconglomerates in the form of lenses and some magmatic intrusions; locally there occur migmatites with alternating bands of neosome (the newly formed metamorphic parts of the migmatites) and paleosome (parts of the migmatites made of the original igneous rock) (Ahrendt, 2005). The secondary minerals include oxides and hydroxides of aluminum and iron along with clay minerals (Ahrendt, 2005).

A geological investigation of the Campos do Jordao plateau at various points between 2-5 km south-east of the study site performed by Modenesi et al. (2010) reveals depths to bedrock (composed of banded gneisses and granitic rock) between 30-50 meters. The depth profiles are a results of drilling performed for the study and they also show water levels between 23 to 37 meters deep. The study also reveals a very thick layer of weathered saprolite over the bedrock (up to 50 meters deep), largely composed of kaolinite clays.

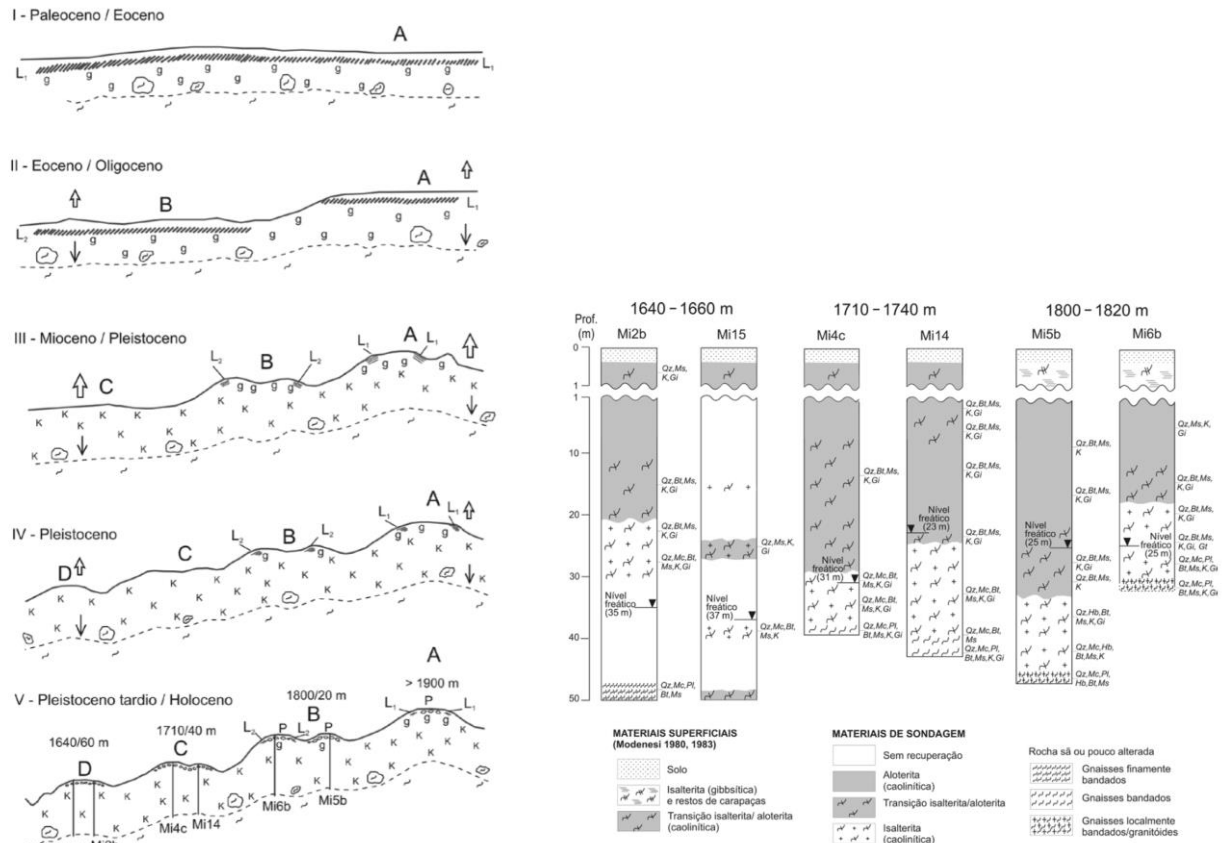


Figure 3.10 – Evolution of the topography of the Campos do Jordão plateau from the Paleocene to the Holocene, not that even the high elevations of the plateau contain thick weathered saprolite layers covering the bedrock (left). Geological profiles obtained by drilling showing depth to bedrock up to 50 m (note that profile Mi15 did not reach bedrock despite going down to 50 m) at different locations with different elevations on the plateau. From Modenesi et al., 2010.

Ahrendt (2005) describes the near-surface geology of the hillside where the site of investigation is located as a division of three layers (Figure 3.11): an upper residual soil layer, a lower residual soil layer, and a saprolite layer (shown as I-R, II-R, and V-S in figure 31 respectively). However, it is important to keep in mind that the exact location of the site of investigation was not characterized in detail, but rather included as having the same geology of the immediate region around the east facing hillsides (group U4 as shown in Figure 3.11).

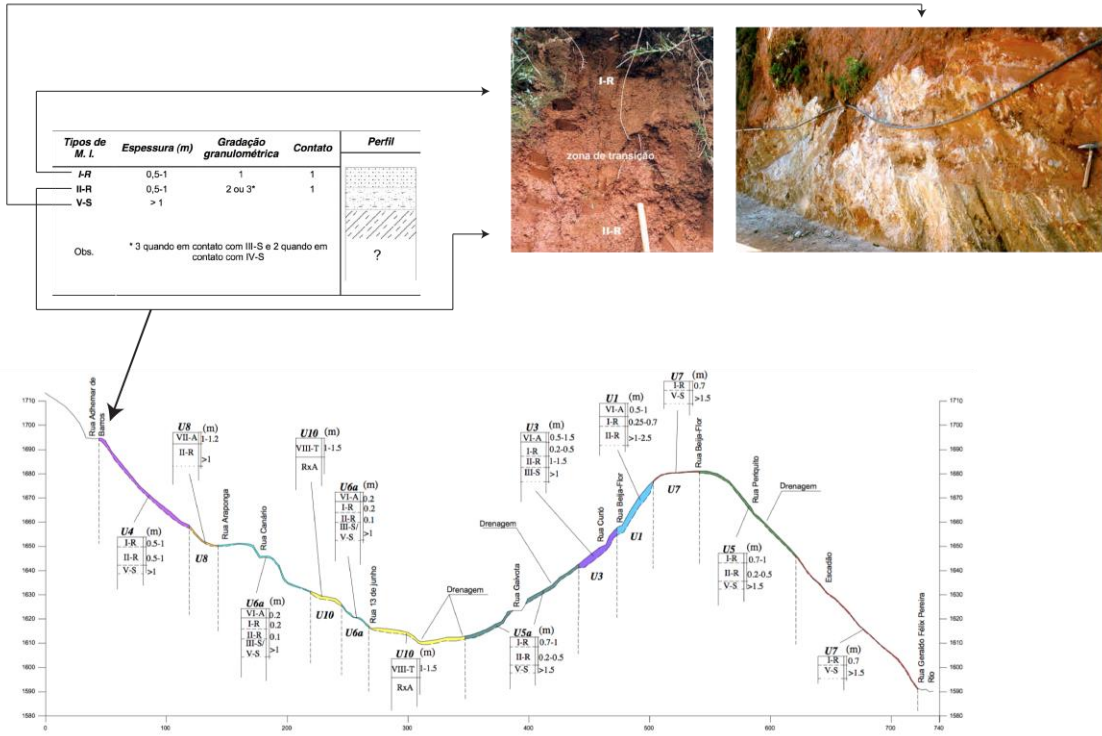


Figure 3.11 – A profile view of the Santo Antônio neighborhood showing the topography and near-surface geological groups defined by Ahrendt (2005). The assumed profile and images of geological layers are shown on the top. Images and diagrams from Ahrendt, 2005.

### 3.3 Existing Geotechnical Data

A near-surface geotechnical investigation was performed by Mendes et al. (2015) within meters of the geophone array line used in this research. Mendes also divides the near-surface into three layers; the topsoil (H1), mature residual soil that is relatively homogenous with no rock matrix structure (H2), and young residual soil or saprolites with a rock matrix structure composed of bedrock pieces that have not fully weathered into saprolite.

Geotechnical characterization in the form of sieve analysis, soil gran density, natural density, and Atterberg limits (liquid and plastic) were performed from three deformed samples that were collected on site (see Figure 3.12, Mendes et al., 2015). The results are shown in Table 3.1.

Municipalities/ experimental field	Localization		Sample/ layer in soil profile	Depth sample (m)	Grain size (%)			Atterberg limits			$\gamma_s$ (kN/m <sup>3</sup> )	$\gamma$ (kN/m <sup>3</sup> )	
	Long.	Lat.			Sand	Silt	Clay	w <sub>L</sub> (%)	w <sub>P</sub> (%)	IP (%)			USCS
Campos do Jordão (Ef-1)	45°36'W	22°44'S	CJ-H1	0.3	54	19	27	25	NP	NP	ML	29.6	13.1
			CJ-H2	3.0	42	14	44	31	29	2	ML	23.5	16.2
			CJ-H3	6.0	67	26	7	24	21	3	SM	27.0	13.8

Table 3.1 – Geotechnical characterization of the three deformed samples from Mendes et al., 2015.



Figure 3.12 – Soil profile from geotechnical investigation (Mendes et al., 2015).

## Chapter 4 - Data Acquisition

### 4.1 Site Investigations

A series of seismic investigations were performed at the area of study (Figure 3.5). Figure 4.1 shows the exact location of the east-west survey line that was used for all active-source investigations. Table 4.1 lists all the field parameters for each survey.



Figure 4.1 – Google Earth satellite image of the area of study and the survey line.

Survey #	Geophone Type	Sample Rate	# of Geophones	Geophone Spacing	Array Length	Source Offset(s)	Source	Analysis
1	Horizontal 24 Hz	.25 ms	96	0.2 m	19 m	.2/19.2/ 30 m	Sledge Hammer	SH-Refraction Love Wave
2	Vertical 4.5 Hz	0.5 ms	48	0.5/1 m	24/48 m	.25/6.25/ 12.25 m	Sledge Hammer	P-Refraction Active-MASW Vertical
3	Horizontal 24 Hz	1 ms	48	0.5/1 m	24/48 m	.25/6.25/ 12.25 m	Sledge Hammer	Active-MASW Radial
4	Vertical 4.5 Hz	1 ms	32	~1.5 m Circular	15 m Diam.	---	Ambient Energy	Passive-MASW Vertical

Table 4.1 - A table of all field parameters for the seismic surveys used for this study.

An experimental SH refraction survey was performed in 2014 (Survey #1 in table 4.1) that was not involved with this work. This survey was performed on the same survey line as illustrated in Figure 4.1. However, as the survey was only experimental and not a conventional refraction survey, it was only performed only with sources with three different offsets on one side of the array. The source was a sledgehammer, which was used to hit against a metal plate that was wedged with its side into the earth to allow for a lateral force to generate SH waves. Shots were stacked 5 times to remove noise.

Three field surveys were performed for this research by the author and a crew from IAG – USP (surveys 2,3 & 4 in Table 4.1). Surveys 2 and 3 are identical in all their characteristics with the exception of the geophone type and the date performed; survey 2 was conducted in May of 2015 and survey 3 in June of 2015. One long array and three short arrays were used for surveys 2 and 3 (see Figure 4.2).

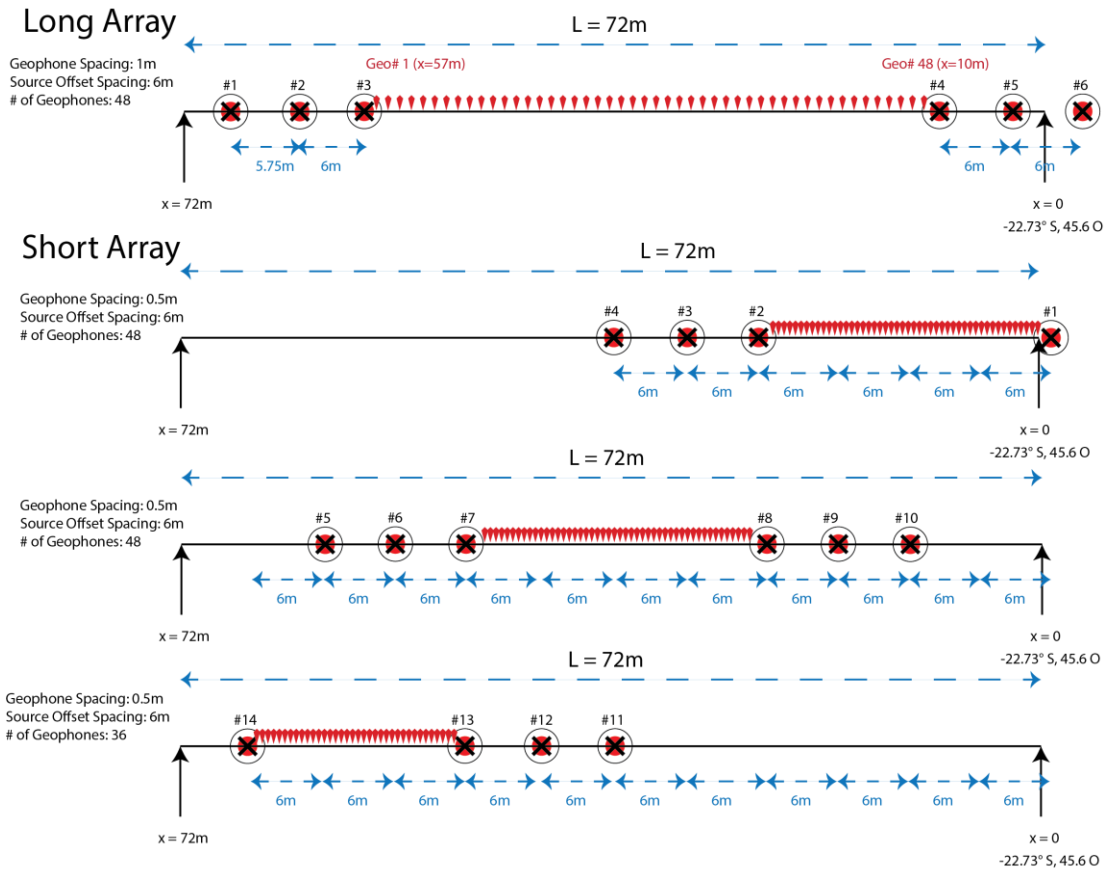


Figure 4.2 –An illustration of the “fixed” long array and the “move-along” short arrays used for surveys 2 and 3.

A “fixed” long array was used to maximize the depth of investigation while sacrificing any lateral variation, and a set of three “move-along” short arrays were used to obtain higher frequency data, by using shorter geophone spacing, and to introduce some lateral variation by allowing for three 1-D inversion points at the mid-section of each short array. Although surveys 2 and 3 appear identical, by performing the same survey with horizontally orientated geophones (oriented in the direction of the geophone line, or radially orientated) the radial component of the Rayleigh wave was recorded, despite the source being a sledgehammer hitting a steel plate in the vertical direction. The multichannel records of surveys 2 and 3 appear to show dispersion of surface wave energy indicating the existence of Rayleigh waves at the site.

And lastly, a passive MASW survey was conducted approximately 150 meters south of the site using a circular array (see figure 3.4). This nearby location was selected because it was the nearest site that appeared to not have been disturbed by means of past human activity, and because unlike the survey line location of all the other surveys, this location was able to accommodate a 2-D geophone array. A passive MASW survey using a linear array at the main site of investigation was not performed due to the fact that some ambient noise energy will arrive obliquely to the linear array and will appear with higher “apparent” velocities than the real velocity of the noise (Louie, 2001). A circular array was chosen as it equally records energy from all directions, providing higher resolutions for ambient sources from all directions. The largest diameter that the site allowed for was used (15 m), as only the deeper layering is of interest at this location. Despite its distance from the original area of study some useful information can be obtained from this passive survey; in particular the deeper geological structure, which it is more likely to share with the original survey line location.

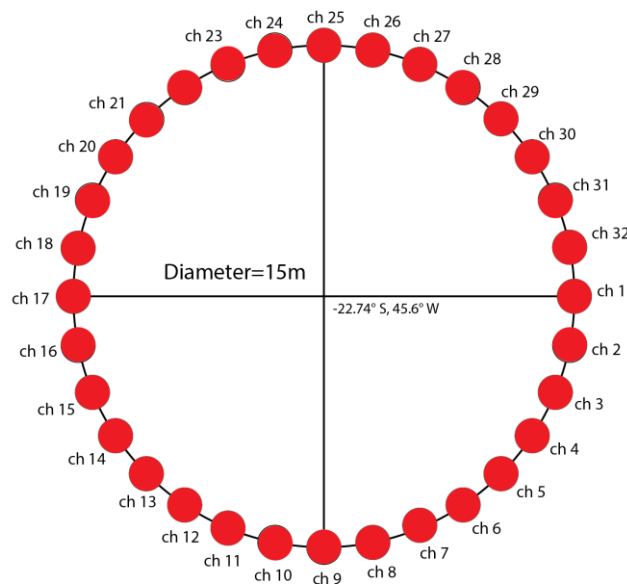


Figure 4.3 - Configuration of the circular array used for the passive-MASW survey.

## Chapter 5 – Data Processing and Analysis

### 5.1 Refraction Data

Rayfract® recommends at least one shot per every sixth receiver in an array for a reliable WET tomography inversion. Although the survey used for P wave refraction analysis does not follow this recommendation, a considerable amount of shot locations were recorded for considerable wave coverage. The SH refraction survey however was experimental and has a very limited wave coverage.

#### 5.1.1 SH Wave Refraction Data

The first arrival picks of SH refraction data can be seen in Appendix D.1. Unfortunately, as the survey was not intended for refraction tomography analysis there are only a limited amount of source locations, only three in fact. As a result, there is a very limited amount of wave coverage (see Figure D.6 in Appendix D) and therefore the smoothed WET inversion results (Figure D.5 in Appendix D) are not very reliable. But nevertheless, it suggests a shallow layer at around a meter in depth.

#### 5.1.2 P Wave Refraction Data

The first arrival picks of P refraction data can be seen in Appendix D.2. It is clear from wave coverage graph (Figure D.10 of Appendix D) that there is much more wave coverage in the P refraction survey as compared to the SH refraction survey. As a result the smoothed WET inversion results (Figure D.9 of Appendix D) are considered to be much more reliable. The inversion results suggest again a layer interface at around a meter in depth, another at 2 meters, and one more interface between six to twelve meters in depth.

## 5.2 Love Wave Data

A dispersion image is obtained from SurfSeis© after processing the multichannel records of the SH refraction survey. It is evident from visual inspection that the 24 Hz geophones did not record low enough frequencies to properly distinguish a fundamental mode Love wave. As a result, fundamental mode inversion was not performed. However a simple inspection of the dispersion image at higher frequencies reveals a minimum velocity of 150 m/s, suggesting that the SH wave velocity of the surface layer is 150 m/s.

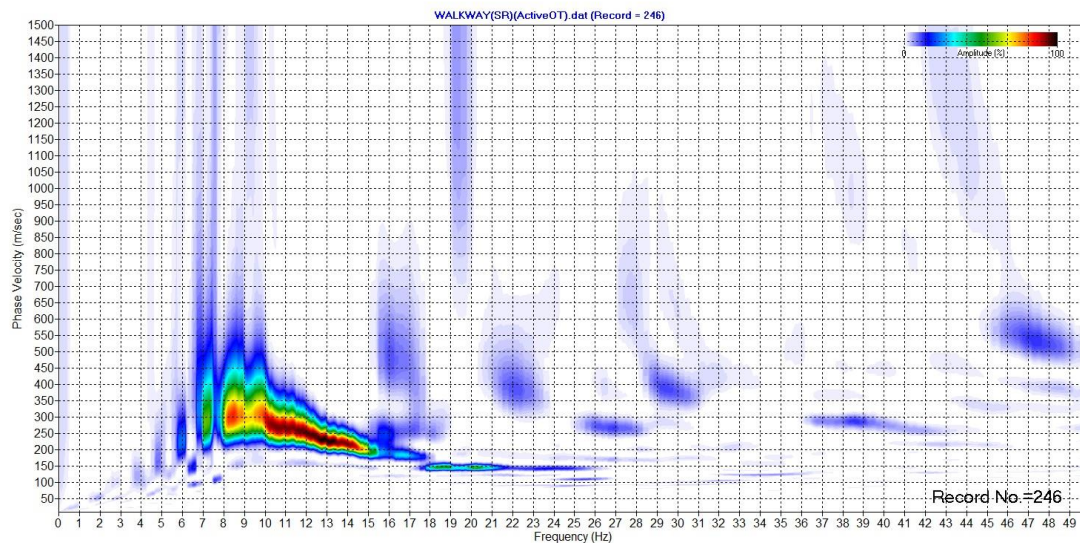


Figure 5.1 - A dispersion image of Love wave energy obtained by processing through SurfSeis©.

### 5.3 Passive MASW

The results of the passive MASW survey are consistent with near surface velocities from other methods. Surprisingly the fundamental mode appears to be visible up to 40 Hz, however, any pattern is lost below 10 Hz. Interestingly, the interface depths also appear to share similarities with the refraction inversion results.

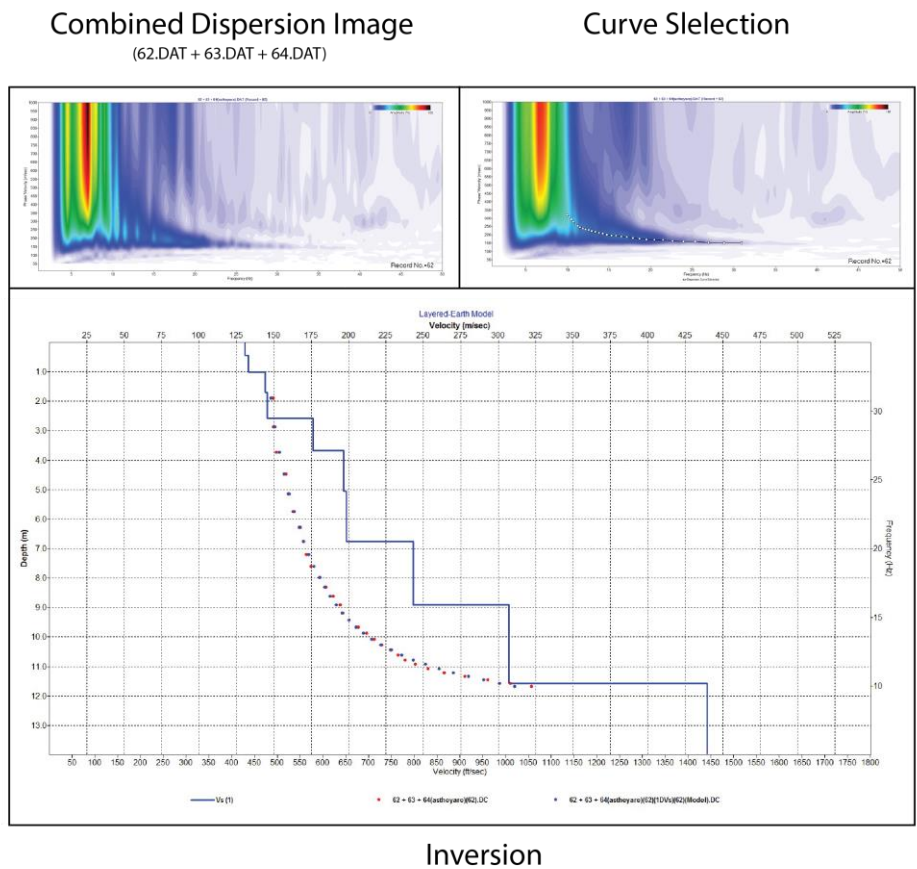


Figure 5.2 - Inversion of the passive MASW survey with circular array, 150 m south of the array line of the area of study. Three dispersion images were combined to increase the signal to noise ratio. Processing was performed using ParkSEIS©.

## 5.4 A-Priori Model

After considering the preceding inversion results and the existing geological and geotechnical data an a-priori model is created to consider for MASW Rayleigh wave inversion. This model is shown below in Figure

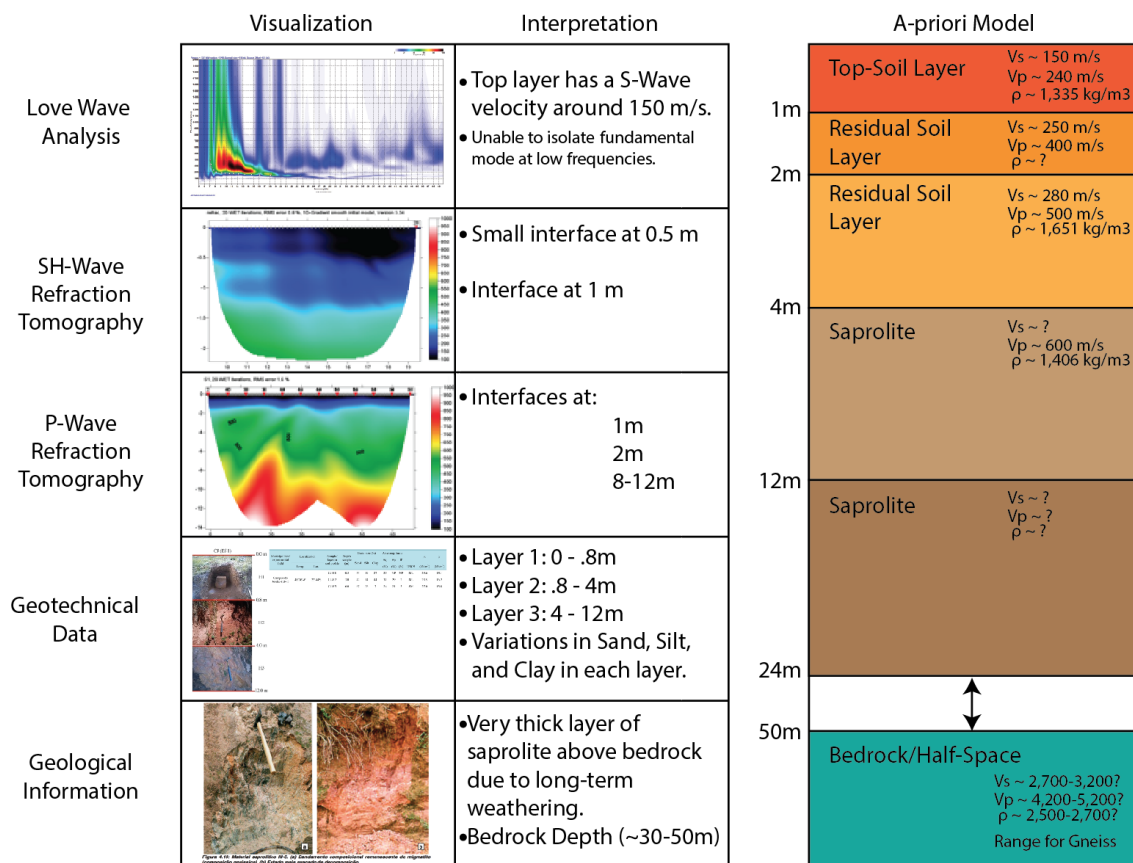


Figure 5.3 - A list of considerations for an a-priori model (left). The a-priori model for MASW inversion (right).

## 5.5 Active MASW

The active source MASW analysis data can be viewed in Appendix E. Section E.1.1 shows all the dispersion images associated with the short arrays used on the geophone line for the shallow survey. It is important to note that the combination of horizontal and vertical components aid in highlighting the fundamental mode at certain frequencies. In many cases the fundamental mode was masked in the vertical component at certain frequency ranges, and therefore by combining it with the horizontal (or radial) component it reemerged. Likewise section E.2.1 shows the dispersion images for the long array for deeper investigation.

Inversion results for the short arrays and long array are shown in E.1.2 and E.2.2, respectively. For the short arrays in E.1.2, inversions are performed for the picked dispersion curves using default initial models in ParkSEIS©, and these inversions are interpolated to create a pseudo two-dimensional inversion. Afterwards, an a-priori model is created and used as the initial model in SurfSeis© for the same dispersion curves. Unfortunately, this a-priori model caused an error in the inversion of the long array dispersion curve in E.2.2. This may have some relation with the rather unusual Poisson's ratio and density values in the model. The best selected inversion of E.2.2 as well as the inversion of its redefined dispersion curve appear to suggest an interface (perhaps of residual soil and saprolite) at around 5 m, followed by gradual increases in velocity until 25 m, where bedrock is not found as the low-frequency data is not available.

An extra low-frequency point is then selected for the best selected inversion of E.2.2 to better define the inversion at low frequencies (Figure E.13). A reasonable shear wave velocity profile is inverted in SurfSeis© (using the default initial model) to obtain Figure E.14. The author believes this inversion to be the most representative 1-D shear wave velocity profile of the site of investigation. This is due to the fact that it agrees well with refraction and other surface wave results, as well as the interfaces defined by geological and geotechnical data. In order to further investigate the validity of this inversion, a comparison between synthetic and real data is shown in section E.2.3.

The synthetic data is obtained using the modeling module in ParkSEIS©, which is based on the reflectivity method by Fuchs and Müller, 1971. The code itself is based on a DOS executable created by Dr. Adam O'Neill at Kyoto University, which is based on codes provided by Dr. Klaus Holliger at the Swiss Federal Institute of Technology and Dr. Michael Roth at NORSAR. The inputted model (inverted model from Figure E.14) is shown in Figure E.15, and the resulting side-by-side comparisons of synthetic and field seismograms and dispersion images are shown in Figures E.16-20.

## Chapter 6 – Results and Conclusions

### 6.1 Limitations and Shortcomings

There are some serious limitations to the inversion of perceived fundamental mode Rayleigh wave energy through MASW analysis, using inversion based on simplified two-dimensional forward modeling approaches, which assume flat layering and homogenous and isotropic behavior in each layer. These limitations include but are not limited to:

- Human error involved in dispersion curve picking
- Human error in the field during field measurements
- Non-uniqueness of fundamental mode dispersion curve inversion
- Violations of perfectly layered homogeneous isotropic media
- The abundance of local minima in the inversion solution space
- Lack of lateral resolution

To test inversion reliability, two models were tested using the author's MATLAB® code, which utilizes the objective function described in Eq. 2.14 and the `fminsearch` algorithm in the inversion processes based on the fundamental mode dispersion curve. These models and the inversion results are shown in Appendix C. Model 1 is a simplified two-layer model, and Model 2 is a 6-layer model from Xia et al., 1999. The inversion of Model 1 is shown in Figure C.3, with only a single initial model, which has similar property profiles, but has a dispersion curve that is quite far from Model 1's. The right hand side of Figure C.3 shows how the simple `fminsearch` based inversion scheme finds a good fit in terms of the dispersion curve,  $V_S$ , and  $V_P$ , but is unable to find a good match for density. Inverting Model 2 on the other hand is much more complicated. Figure C.6 shows the inversion results of Model 2 and how they differ with 9 different initial models, which only differ in the value of  $V_P$  (by modifying the Poisson's ratio), and depth to the half-space. The results highlight the abundance of local minima of the objective function (Eq. 2.14), and how important initial models are in the inversion process. To have the best initial model it is imperative to have as much knowledge of the parameters as possible. The sensitivity analysis in Figure C.7 reveals that the thicknesses of each layer influences the dispersion curve the greatest, followed by  $V_S$ , with little contribution from  $V_P$ , and practically no influence from density.

### 6.2 Areas of Future Improvement

MASW and surface wave analysis in general are currently very active research topics (Socco et al, 2010). A promising new research includes a new method called "Polar Mute", which mutes higher mode energy in the dispersion image by separating prograde and retrograde motion (Gribler, 2015). It is conceivable that more muting techniques will

further help in isolating the energy of different modes in the dispersion image. However, an altogether different approach is the inversion of the dispersion image itself. Dal Moro has dubbed this “Full Velocity Spectrum Inversion” (Moro, 2015). This approach eliminates the human error involved in picking the fundamental mode dispersion curve from the dispersion image, or “Full Velocity Spectrum”. Another approach is the inversion of the “effective dispersion curve” (Moro, 2015). The effective dispersion curve is essentially the curve, which follows the pattern of highest energy on the dispersion image. Tokimatsu et al., 1992 provides the relationships between the effective dispersion curve and the modal dispersion curves. The most computationally intensive inversion method is full waveform inversion. However, this method and is rarely used for near surface applications. Perhaps the most complete inversion possible would be a full waveform inversion assuming a viscoelastic-anisotropic-inhomogeneous medium, but computer technology has not reached the level to where this would be practicable for most applications.

### 6.3 Final Conclusions

It is the author’s opinion that the biggest drawback to the MASW method (as defined in this research) is the relatively long array length (and therefore lack of lateral resolution) required to obtain higher resolution dispersion images and the uncertainty in picking the dispersion curve. Ultimately, a series of picked points on the perceived fundamental mode dispersion curve from phase-shifted seismic data does not necessarily invert into reliable results. However crude this method may appear, it can be quite powerful and effective when combining data from both horizontal and vertical components, implementing various filtering tools, and knowing some a-priori information (particularly at depths, which correspond to the most sensitive frequencies of the dispersion curve).

It appears that the MASW results in this research have not only confirmed the refraction WET tomography inversion results, but also inverted realistic deeper shear wave velocity profiles (though unfortunately not reaching the bedrock). Ultimately, the maximum invertible depth at the site of investigation is limited to the length of the array, which was limited by the site constraints of the site of investigation. Although this method still has some way to improve, it is without question a valuable tool to increase the amount of subsurface information from a conventional refraction or linear array seismic survey.

With respect to implications of the results to land slide risk, one can see a consistent near surface layer interface from virtually all sources (geotechnical, refraction, and surface wave) at around one meter in depth. This is characterized as the interface between the top-soil layer and the residual soil. This interface depth appears to be consistent with the slip surfaces reported by Ahrendt (2005), and therefore is potentially related to the slip surface depths of the landslides that occurred in Campos do Jordão the winter of 1999/2000. However, the depth to bedrock was not obtainable due to the limited array length, and the water level was not found due to the limited depth of the P wave WET tomography inversion results.

## References

- Ahrendt, A., 2005. Movimentos de massa gravitacionais—proposta de um sistema de previsão: aplicação na área urbana de Campos do Jordão—SP. Diss. Tese de Doutorado, USP, São Carlos.
- Aki, K., & Richards, P. G., 1980. Quantitative Seismology. Vol. 1 & Vol. 2.
- ASTM D2487-11, 2011. Standard Practice for Classification of Soils for Engineering Purposes (Unified Soil Classification System), ASTM International, West Conshohocken, PA, [www.astm.org](http://www.astm.org).
- Bogoslovsky, V. A., & Ogilvy, A., 1977. GEOPHYSICAL METHODS FOR THE INVESTIGATION OF LANDSLIDES. GEOPHYSICS, VOL. 42 , 562-571.
- Boore, David M., 1972. Finite difference methods for seismic wave propagation in heterogeneous materials. *Methods in computational physics* 11: 1-37.
- Burger, H. R., Sheehan, A. F., & Jones, C. H., 2006. Introduction to Applied Geophysics. W.W. Norton & Company, Inc.
- Caris, J. P., & Van Asch, T. W., 1991. Geophysical, geotechnical and hydrological investigations of a small landslide in the French Alps. *Engineering Geology*, 31(3), p 249-276.
- Chamley, Hervé, 1990. *Sedimentology*. Berlin: Springer-Verlag.
- Chapman, Chris, 2004. *Fundamentals of seismic wave propagation*. Cambridge University Press.
- Chen, Xiaofei, 1993. A systematic and efficient method of computing normal modes for multilayered half-space. *Geophysical Journal International* 115.2: 391-409.
- Coccia, S., Del Gaudio, V., Venisti, N., & Wasowski, J., 2010. Application of Refraction Microtremor (ReMi) technique for determination of 1-D shear wave velocity in a landslide area. *Journal of Applied Geophysics*, 71.2, p 71-89.
- De Lucena, R. F., 2014. Avaliações e testes dos Métodos MASW e ReMi por meio do tratamento de dados empíricos e sintéticos em um programa de processamento e inversão desenvolvido em Matlab e sua aplicação em problema geológico na Bacia de Taubaté. Diss. Tese de Doutorado, Instituto de Geociências da USP, São Paulo.
- Foti, Sebastiano, 2000. Multistation methods for geotechnical characterization using surface waves. Diss. Politecnico di Torino.
- Foti, S., Lai, C. G., Rix, J. G., & Strobbia, C., 2015. *Surface Wave Methods for Near-Surface Site Characterization*. CRC Press.

- Fuchs, K., and G. Müller, 1971. Computation of synthetic seismograms with the reflectivity method and comparison with observations. *Geophysical Journal International* 23.4: 417-433.
- Glade, T., Stark, P., & Dikau, R., 2004. Determination of potential landslide shear plane depth using seismic refraction—a case study in Rheinhessen, Germany. *Bulletin of Engineering Geology and the Environment* 64(2): 151-158.
- Godio, A., Strobbia, C., & De Bacco, G., 2005. Geophysical characterisation of a rockslide in an alpine region. *Engineering Geology* , 273-286.
- Grandjean, G., Gourry, J., Sanchez, O., Bitri, A., & Garambois, S., 2011. Structural study of the Ballandaz landslide (French Alps) using geophysical imagery. *Journal of Applied Geophysics* 75:531-542.
- Gribler, Gabriel, 2015. Multi-Component Active Source Rayleigh Wave Analysis. Diss. Boise State University.
- Hack, R., 2000. GEOPHYSICS FOR SLOPE STABILITY. *Surveys in Geophysics*, 21.4, p 423-448.
- Haskell, Norman A., 1953. The dispersion of surface waves on multilayered media. *Bulletin of the seismological Society of America* 43.1: 17-34.
- Havenith, H. B., Jongmans, D., Abdrakhmatov, K., Trefois, P., Delvaux, D., & Torgoev, I., 2000. GEOPHYSICAL INVESTIGATIONS OF SEISMICALLY INDUCED SURFACE EFFECTS: CASE STUDY OF A LANDSLIDE IN THE SUUSAMYR VALLEY, KYRGYSTAN. *Surveys in Geophysics* , 349-369.
- Hiruma, S. T., 1999. NEOTECTÔNICA NO PLANALTO DE CAMPOS DO JORDÃO, SP: DISSERTAÇÃO DE MESTRADO. UNIVERSIDADE DE SÃO PAULO, INSTITUTO DE GEOCIÊNCIAS.
- Ivanov, Julian Metodiev, 2002. JASR: Joint analysis of surface-waves and refractions. Thesis (Ph.D.) - University of Kansas.
- Jones, R., 1958. In-situ measurement of the dynamic properties of soil by vibration methods. *Geotechnique* 8.1 , 1-21.
- Jones, R., 1962. Surface wave technique for measuring the elastic properties and thickness of roads: Theoretical development. *British Journal of Applied Physics*, Vol. 13 , 21-29.
- Jongmans, D., & Garambois, S., 2007. Geophysical investigation of landslides : a review. *Bulletin de la Société géologique de France*, 178.2, p 101-102. .
- Jongmans, D., Bèvre, G., Renalier, F., Schwartz, S., Bearez, N., & Orengo, Y., 2009. Geophysical investigation of a large landslide in glaciolacustrine clays in the Trièves area (French Alps). *Engineering Geology* 109: 45-56.

- Kausel, Eduardo, and José Manuel Roësset, 1981. Stiffness matrices for layered soils. *Bulletin of the Seismological Society of America* 71.6: 1743-1761.
- Kramer, S. L., 1996. *Geotechnical Earthquake Engineering*. In prentice-Hall international series in civil engineering and engineering mechanics. Prentice-Hall, New Jersey.
- Kennett, B. L. N., 1984. Guided wave propagation in laterally varying media—I. Theoretical development. *Geophysical Journal International* 79.1: 235-255.
- Lay, T., & Wallace, T. C., 1995. *Modern global seismology* (Vol. 58). Academic press.
- Lecomte, I., Gjøystdal, H., Dahle, A., & Pedersen, O., 2000. Improving modelling and inversion in refraction seismics with a first order Eikonal solver. *Geophysical Prospecting*, v.48, pp.437-454.
- Louie, John N., 2001. Faster, better: shear-wave velocity to 100 meters depth from refraction microtremor arrays. *Bulletin of the Seismological Society of America* 91.2: 347-364.
- Luco, J. Enrique, and Randy J. Apsel, 1983. On the Green's functions for a layered half-space. Part I/II. *Bulletin of the Seismological Society of America* 73.4: 909-929.
- Lysmer, John, and Lawrence A. Drake, 1972. A finite element method for seismology. *Methods of computational physics* 11: 181-216.
- McMechan, G. A., & Yedlin, M. J., 1981. Analysis of dispersive waves by wave field transformation. *Geophysics* 46.6 , 869-874.
- Mendes, R. M., 2012. Estudo de campos experimentais de monitoramento de variáveis climáticas e geotécnicas para implantação de sistemas de alerta para escorregamentos no Estado de São Paulo. Projeto de Pesquisa FAPESP 2011/22577-2.
- Mendes, R. M., & Filho, M., 2015. Real-Time Monitoring of Climactic and Geotechnical Variables during Landslides on the Slopes of Serra do Mar and Serra da Mantiqueira (São Paulo State, Brazil). *Engineering* 7 , 140-159.
- Modenesi-Gauttieri, M. C., Motta de Toledo, M. C., da Rocha Soares, L. C., Taioli, F., & Shimada, H., 2010. Gênese e evolução do saprólito no planalto de Campos do Jordão: implicações na evolução do relevo. *Revista Brasileira de Geociências* 40(2) , 242-255.
- Moro, G. D., 2015. *Surface Wave Analysis for Near Surface Applications*. Elsevier.
- Nazarian, S., & Stokoe, K. H., 1984. In situ shear wave velocities from spectral analysis of surface waves. *Proceedings of the 8th world conference on earthquake engineering* Vol. 3.
- Park, C. B., & Miller, R., 2008. Roadside Passive Multichannel Analysis of Surface Waves (MASW). *Journal of Environmental & Engineering Geophysics*, v. 13, no. 1, p. 1-11.

Park, C. B., Miller, R. D., & Xia, J., 1998. Imaging dispersion curves of surface waves on multi-channel record. SEG Expanded Abstracts , Vol. 17. No. 1.

Park, C. B., Miller, R. D., & Xia, J., 1999. Multichannel analysis of surface waves. *Geophysics*, v. 64, no. 3, p. 800-808.

Park, C. B., Miller, R. D., & Xia, J., 2001. Offset and resolution of dispersion curve in multichannel analysis of surface waves (MASW). In *Proceedings of the SAGEEP*.

Park, C. B., Miller, R. D., & Miura, H., 2002. Optimum field parameters of an MASW survey. *Exp. Abs.]: SEG-J, Tokyo*.

Pei, Donghong, 2007. Modeling and inversion of dispersion curves of surface waves in shallow site investigations. ProQuest Dissertations and Theses; Thesis (Ph.D.)-University of Nevada, Reno.

Penumadu, D., & Park, C. B., 2005. Multichannel analysis of surface wave (MASW) method for geotechnical site characterization. In *Proceedings of the Geo-Frontiers conference, Austin, Texas*.

Reynolds, J. M., 2011. *An Introduction to Applied and Environmental Geophysics 2nd Edition*. Wiley-Blackwell.

Richart, Frank Edwin, John Russell Hall, and Richard D. Woods, 1970. "Vibrations of soils and foundations."

Rohdewald, S.R., (n.d.). Delta-t-V 1D seismic refraction: Theory. "<http://rayfract.com/pub/deltatv.pdf>"

Santamarina, J. C., 2001. *Soils and Waves: Particulate Materials Behavior, Characterization and Process Monitoring*. John Wiley & Sons, LTD.

Schuster, G. T., & Quintos-Bosz, A., 1993. Wavepath eikonal travelttime inversion: Theory. *Geophysics*, volume 58, pp. 1314-1323. .

Schwab, F. A., & Knopoff, L., 1972. Fast surface wave and free mode computations. *Methods in computational physics* 11 (87-180).

Shearer, Peter M., 2009. *Introduction to seismology*. Cambridge University Press.

Sheehan, Jacob R., William E. Doll, and Wayne A. Mandell, 2005. An evaluation of methods and available software for seismic refraction tomography analysis. *Journal of Environmental & Engineering Geophysics* 10.1: 21-34.

Socco, L. V., Foti, S., & Boiero, D., 2010. Surface-wave analysis for building near-surface velocity models — Established approaches and new perspectives. *Geophysics*, 75(5), 75A83-75A102. .

Spillmann, T., Maurer, H., Willenberg, H., Evans, K. F., Heincke, B., & Green, A. G., 2007. Characterization of an unstable rock mass based on borehole logs and diverse borehole radar data. *Journal of Applied Geophysics* 61, 16-38.

- Stein, Seth, and Michael Wysession, 2009. An introduction to seismology, earthquakes, and earth structure. John Wiley & Sons.
- Stokoe, Kenneth H., and J. Carlos Santamarina, 2000. "Seismic-wave-based testing in geotechnical engineering." ISRM International Symposium. International Society for Rock Mechanics.
- Thomson, William T, 1950. "Transmission of elastic waves through a stratified solid medium." *Journal of applied Physics* 21.2: 89-93.
- Tokimatsu, Kohji, Shuji Tamura, and Hisaya Kojima, 1992. Effects of multiple modes on Rayleigh wave dispersion characteristics. *Journal of Geotechnical Engineering* 118.10: 1529-1543.
- Udías, Agustín, 1999. Principles of seismology. Cambridge University Press.
- Viktorov, Igor A., 1967. Rayleigh and Lamb Waves: Physical Theory and Applications. Transl. from Russian. With a Foreword by Warren P. Mason. Plenum Press.
- Watanabe, T., Matsuoka, T., & Ashida, Y., 1999. Seismic traveltime tomography using Fresnel volume approach. 69th Ann. Internat. Mtg., SEG, Expanded Abstracts .
- Willenberg, H., Loew, S., Eberhardt, E., Evans, K. F., Spillmann, T., Heincke, B., et al., 2008. Internal Structure and deformation of an unstable crystalline rock mass above Randa (Switzerland): Part I — Internal structure from integrated geological and geophysical investigations. *Engineering Geology* 101, 1-14.
- Xia, J., Miller, R. D., & Park, C. B., 1999. Estimation of near-surface shear-wave velocity by inversion of Rayleigh waves. *Geophysics* , v.64, n.3, p.691-700.
- Xia, Jianghai, et al., 2003. "Inversion of high frequency surface waves with fundamental and higher modes." *Journal of Applied Geophysics* 52.1: 45-57.
- Xia, Jianghai, and Yixian Xu, 2005. "Discussion on some practical equations with implications to high-frequency surface-wave techniques." 18<sup>th</sup> EEGS Symposium on the Application of Geophysics to Engineering and Environmental Problems.
- Xu, Yixian, Jianghai Xia, and Richard D. Miller, 2006. "Quantitative estimation of minimum offset for multichannel surface-wave survey with actively exciting source." *Journal of Applied Geophysics* 59.2: 117-125.
- Yilmaz, Özdoğan, 2001. Seismic data analysis. Vol. 1. Tulsa, OK: Society of exploration geophysicists.

## Appendix A

### Elastic Wave Theory

The following section gives an overview of the equations that define the motion of seismic waves in media that can be characterized as linearly-elastic, homogenous, and isotropic.

The justification of the elasticity assumption is based on the observation that “small mechanical perturbations traverse particulate media without causing permanent effects or altering on-going processes.” (Santamarina, 2001). However, this statement is only valid for small-strain waves. Large-strain waves may be generated in the near field of sources and in the near surface during earthquakes (Santamarina, 2001). As a result, the following equations are not valid in the near-field of a source and for very large “earthquake” magnitude sources. However, for small strains the soil behaves essentially as a linear medium (Foti, 2000).

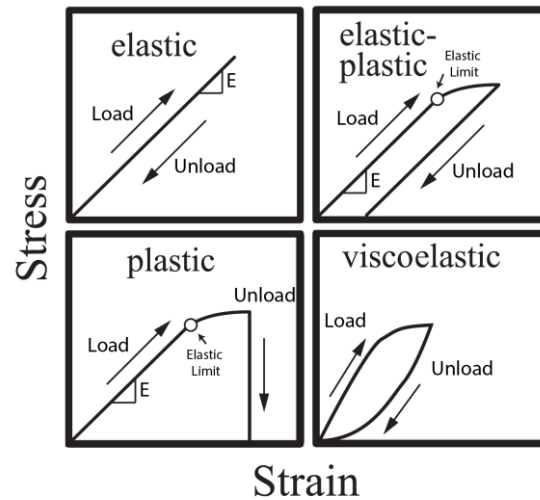


Figure A.1 - Stress-strain curves under elastic, elastic-plastic, plastic, and viscoelastic regimes.  $E$  represents Young's Modulus in Elastic regions. Note that viscoelastic behavior is curved due to a time delay as a result of the absorption of energy.

## A.1 Elastic Parameters

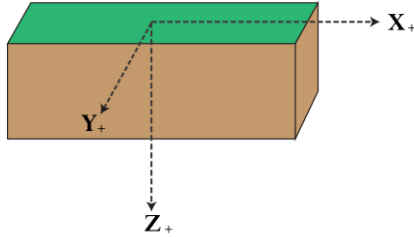


Figure A.2 - Coordinate system used in presented equations. Note that the x-axis follows the direction of wave propagation on the surface for all two-dimensional equations.

### Velocities and Poisson's Ratio:

$$V_S = \sqrt{\frac{\mu}{\rho}} = \sqrt{\frac{G}{\rho}}$$

$$V_P = \sqrt{\frac{\lambda + 2\mu}{\rho}} = \sqrt{\frac{G(2 - 2\nu)}{\rho(1 - 2\nu)}}$$

$$V_S = V_{SH} = V_{SV} \text{ (for isotropic media)}$$

$$\nu = -\frac{\epsilon_{\text{transverse}}}{\epsilon_{\text{longitudinal}}} = \frac{\lambda}{2(\lambda + \mu)}$$

### Isotropic Elastic Moduli:

$$E = \frac{\text{longitudinal stress}}{\text{longitudinal strain}} \text{ (for no lateral stress)} = 2G(1 + \nu) = 2K(1 - 2\nu)$$

$$= \frac{\mu(3\lambda + 2\mu)}{\lambda + \mu}$$

$$K = \frac{\text{Pressure}}{\text{Vol. Strain}} = \frac{E}{3(1 - 2\nu)} = \lambda + \frac{2\mu}{3}$$

$$M = \frac{\text{longitudinal stress}}{\text{longitudinal strain}} (\text{for no lateral strain}) = \frac{E(1-\nu)}{(1+\nu)(1-2\nu)} = \lambda + \frac{2\mu}{3}$$

$$= \rho V_P^2$$

$$G = \frac{\text{shear stress}}{\text{shear strain}} = \frac{E}{1(1+\nu)} = \mu = \rho V_S^2$$

**Lame's Constants:**

$$\lambda = \frac{\nu E}{(1+\nu)(1-2\nu)} = K - \frac{2}{3}G = \rho(V_P^2 - 2V_S^2)$$

$$\mu = \frac{E}{2(1+\nu)} = 3K \frac{(1-2\nu)}{(2+2\nu)} = G = \rho V_S^2$$

**Strain-Displacement Relationships:**

$$\varepsilon_x = \frac{\partial u_x}{\partial x}, \varepsilon_y = \frac{\partial u_y}{\partial y}, \varepsilon_z = \frac{\partial u_z}{\partial z}, \varepsilon_v = \varepsilon_x + \varepsilon_y + \varepsilon_z$$

$$\gamma_{xy} = \frac{\partial u_x}{\partial y} + \frac{\partial u_y}{\partial x}, \gamma_{xz} = \frac{\partial u_x}{\partial z} + \frac{\partial u_z}{\partial x}, \gamma_{yx} = \frac{\partial u_y}{\partial x} + \frac{\partial u_x}{\partial y}, \gamma_{yz} = \frac{\partial u_y}{\partial z} + \frac{\partial u_z}{\partial y},$$

$$\gamma_{zx} = \frac{\partial u_z}{\partial x} + \frac{\partial u_x}{\partial z}, \gamma_{zy} = \frac{\partial u_z}{\partial y} + \frac{\partial u_y}{\partial z}$$

## A.2 A Review of Hooke's Law

Hooke's law relates stress and strain through Young's modulus  $E$  and Poisson's ratio  $\nu$  (Santamarina, 2000). Let us apply Hooke's law to define strain in terms of stress and vice-versa.

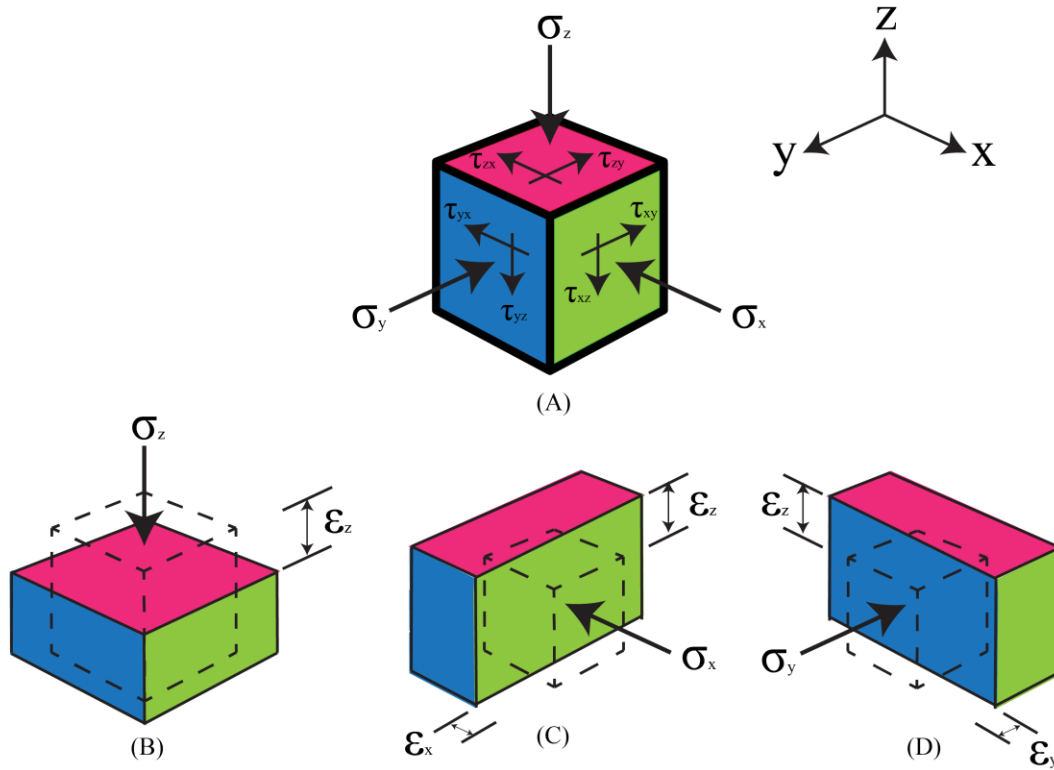


Figure A.3 Constitutive relations: (A) Normal and shear stress acting on an element. (B, C, D) The relationship between normal stress and normal strain - Hooke's law in three dimensions. Adapted from (Santamarina, 2001).

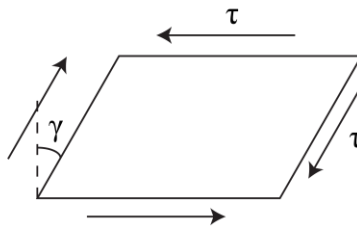


Figure A.4 - The relationship between shear stress and shear strain.

The constitutive relations derived from Hooke's law allows us to redefine the stresses and strains on a three-dimensional element.

**Generalized Hooke's Law (Stress-Strain) relationships:**

$$\epsilon_x = + \frac{\sigma_x}{E} - \frac{\nu\sigma_y}{E} - \frac{\nu\sigma_z}{E}$$

$$\varepsilon_y = -\frac{\nu\sigma_x}{E} + \frac{\sigma_y}{E} - \frac{\nu\sigma_z}{E}$$

$$\varepsilon_z = -\frac{\nu\sigma_x}{E} - \frac{\nu\sigma_y}{E} + \frac{\sigma_z}{E}$$

$$\gamma_{xy} = \frac{\tau_{xy}}{G}, \gamma_{yz} = \frac{\tau_{yz}}{G}, \gamma_{zx} = \frac{\tau_{zx}}{G}$$

Inversely, we can also define stresses in terms on strain and simplifying with lame's constants we get,

$$\sigma_x = \lambda\varepsilon_v + 2\mu\varepsilon_x$$

$$\sigma_y = \lambda\varepsilon_v + 2\mu\varepsilon_y$$

$$\sigma_z = \lambda\varepsilon_v + 2\mu\varepsilon_z$$

$$\tau_{xy} = \mu\gamma_{xy}, \tau_{yz} = \mu\gamma_{yz}, \tau_{zx} = \mu\gamma_{zx}$$

## A.3 Elastic Wave Equations

**Variable definitions:**

$$\omega = 2\pi f$$

$$k_R = \frac{\omega}{V_R}$$

$$k_L = \frac{\omega}{V_L}$$

$$i = \sqrt{-1}$$

$$\nabla^2 = \frac{\partial^2}{\partial x^2} + \frac{\partial^2}{\partial y^2} + \frac{\partial^2}{\partial z^2}$$

We can imagine the setting shown in figure 32, where we consider all the stresses acting on an element during wave propagation (isolated for the x-direction). Newtonian physics dictates that the sum of all forces must be equal to the inertial force of the element (Santamarina, 2000). Therefore, we can state that,

$$\frac{\text{Mass} \times \text{Acceleration}}{\text{unit volume}} = \frac{\text{force}}{\text{unit volume}}$$

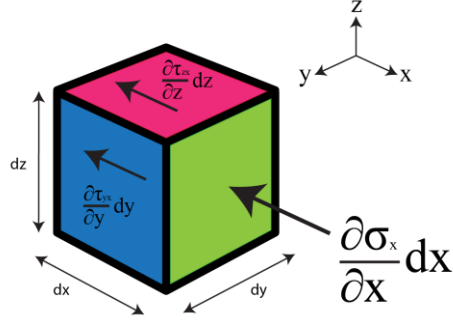


Figure A.5 Stresses acting on an element during wave propagation (isolated for the x-direction). Adapted from (Santamarina, 2001).

**Wave Equations:**

$$\rho \frac{\partial^2 u_x}{\partial t^2} = \frac{\partial \sigma_x}{\partial x} + \frac{\partial \tau_{yx}}{\partial y} + \frac{\partial \tau_{zx}}{\partial z} \quad \text{wave propagation in x-direction} \quad (\text{A.1})$$

$$\rho \frac{\partial^2 u_y}{\partial t^2} = \frac{\partial \tau_{xy}}{\partial x} + \frac{\partial \sigma_y}{\partial y} + \frac{\partial \tau_{zy}}{\partial z} \quad \text{wave propagation in y-direction}$$

$$\rho \frac{\partial^2 u_z}{\partial t^2} = \frac{\partial \tau_{xz}}{\partial x} + \frac{\partial \tau_{yz}}{\partial y} + \frac{\partial \sigma_z}{\partial z} \quad \text{wave propagation in z-direction}$$

Equation (A.1) can be expressed in terms of strain by using Hooke's law.

$$\rho \frac{\partial^2 u_x}{\partial t^2} = M \frac{\partial \varepsilon_v}{\partial x} + G \left( -2 \frac{\partial \varepsilon_y}{\partial x} - 2 \frac{\partial \varepsilon_z}{\partial x} + \frac{\partial \gamma_{zx}}{\partial z} + \frac{\partial \gamma_{yx}}{\partial y} \right) \quad (\text{A.2})$$

$$\rho \frac{\partial^2 u_x}{\partial t^2} = (M - G) \left( \frac{\partial^2 u_x}{\partial x^2} + \frac{\partial^2 u_y}{\partial x \partial y} + \frac{\partial^2 u_z}{\partial x \partial z} \right) + G \left( \frac{\partial^2 u_x}{\partial x^2} + \frac{\partial^2 u_x}{\partial y^2} + \frac{\partial^2 u_x}{\partial z^2} \right) \quad (\text{A.3})$$

Equation (A.3) can be reduced to the following, and applying the same process to all direction we get,

$$\rho \frac{\partial^2 u_x}{\partial t^2} = (M - G) \frac{\partial \varepsilon_v}{\partial x} + G \nabla^2 u_x \quad \text{wave propagation in x-direction}$$

$$\rho \frac{\partial^2 u_y}{\partial t^2} = (M - G) \frac{\partial \varepsilon_v}{\partial y} + G \nabla^2 u_y \quad \text{wave propagation in y-direction}$$

$$\rho \frac{\partial^2 u_z}{\partial t^2} = (M - G) \frac{\partial \varepsilon_v}{\partial z} + G \nabla^2 u_z \quad \text{wave propagation in z-direction}$$

**Body Waves:**

From these wave equations we define the fundamental seismic body waves, P-waves and S-waves. And we assume the wave has propagated sufficiently from the source to be considered a plane wave.

For a compressional (P) wave we know that displacement only exists in the direction of propagation and therefore we have,

$$\frac{\partial^2 u_x}{\partial t^2} = \frac{M}{\rho} \frac{\partial^2 u_x}{\partial x^2} \text{ P-wave propagation in x-direction}$$

$$\frac{\partial^2 u_y}{\partial t^2} = \frac{M}{\rho} \frac{\partial^2 u_y}{\partial y^2} \text{ P-wave propagation in y-direction}$$

$$\frac{\partial^2 u_z}{\partial t^2} = \frac{M}{\rho} \frac{\partial^2 u_z}{\partial z^2} \text{ P-wave propagation in z-direction}$$

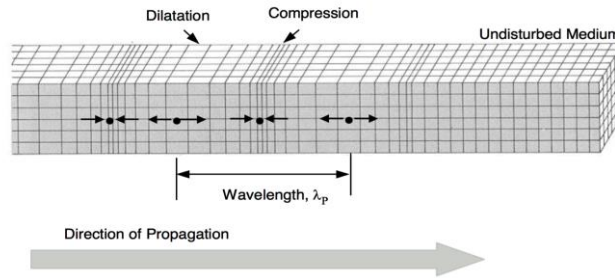


Figure A.6 – P wave propagation, from Stokoe & Santamarina, 2000.

For a shear (S) wave we know that Particle motion only exists perpendicular to propagation direction and we have,

$$\frac{\partial^2 u_y}{\partial t^2} = \frac{G}{\rho} \frac{\partial^2 u_y}{\partial x^2} \text{ SH-wave propagation in x-direction}$$

$$\frac{\partial^2 u_z}{\partial t^2} = \frac{G}{\rho} \frac{\partial^2 u_z}{\partial x^2} \text{ SV-wave propagation in x-direction}$$

$$\frac{\partial^2 u_x}{\partial t^2} = \frac{G}{\rho} \frac{\partial^2 u_x}{\partial y^2} \text{ SH-wave propagation in y-direction}$$

$$\frac{\partial^2 u_z}{\partial t^2} = \frac{G}{\rho} \frac{\partial^2 u_z}{\partial y^2} \text{ SV-wave propagation in y-direction}$$

$$\frac{\partial^2 u_x}{\partial t^2} = \frac{G}{\rho} \frac{\partial^2 u_x}{\partial z^2} \text{ SH-wave propagation in z-direction (displacement in x-direction)}$$

$$\frac{\partial^2 u_y}{\partial t^2} = \frac{G}{\rho} \frac{\partial^2 u_y}{\partial z^2} \text{ SH-wave propagation in z-direction (displacement in y-direction)}$$

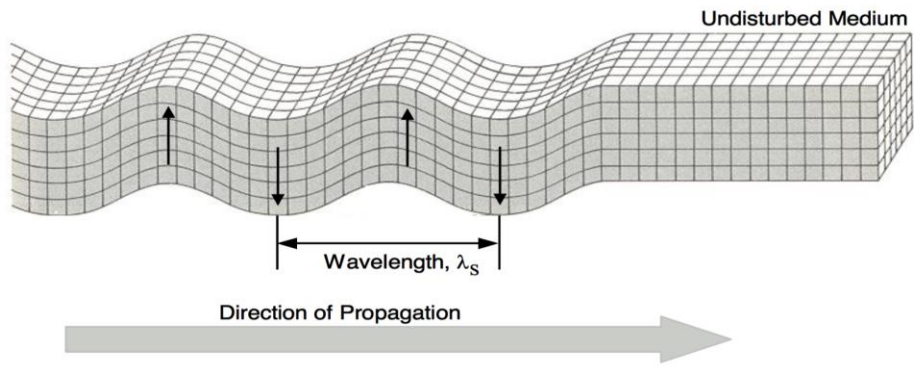


Figure A.7 - SV wave propagation, from Stokoe & Santamarina, 2000.

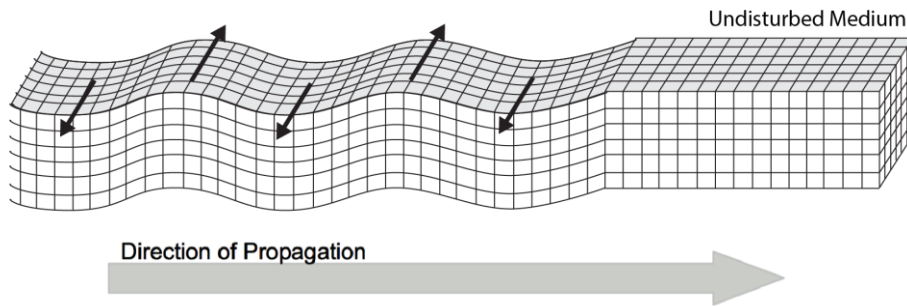


Figure A.8 - SH wave propagation

## Appendix B

### Dispersion Function Codes

The inversion of surface wave dispersion is only possible by means a forward modeling equation or algorithm. Forward modeling surface wave dispersion requires solving the wave equation, an often very difficult task. The most common approaches involved using the transfer matrix method, introduced by Thomson (1950) and Haskell (1953).

The following is a compact code written in the MATLAB® language that utilizes the Rayleigh wave dispersion algorithm provided by De Lucena (2014). This function inputs angular frequency, Rayleigh wave phase velocity, and the parameters of a layered model (i.e.  $V_p, V_s, \rho, h$  for each layer). The output of the function varies with frequency and phase velocity, but when it reaches zero (i.e. a root) the inputs represent a point on a dispersion curve. Another algorithm (not provided in this report) was developed to find all the roots of this function to eventually plot the dispersion curves.

```
function H=dunkin(param,c,w)      %c = Phase velocity, w = Angular frequency
n = length(param)/4;           %n = Number of layers
a = param(1:n);                %a = Vp (m/s)
B = param((n+1):(n+1+n-1));    %B = Vs (m/s)
pn = param((2*n+1):(2*n+1+n-1)); %pn = Density (kg/m3)
dn = param((3*n+1):(3*n+1+n-1)); %dn = Thickness (m)
k=w/c;                          %k = wavenumber (1/m)
%-----
l=n;
while l >= 1 %Begin loop at halfspace, then go up by 1 layer until done
    if l==n %Algorithm for the half-space
        hn=sqrt(((k)^2)-(w^2/(a(1)^2)));
        kn=sqrt(((k)^2)-(w^2/(B(1)^2)));
        ln=2.*(k)^2-(w.^2/(B(1)^2));
        un=pn(1)*B(1)^2; %Shear modulus G or rigidity of layer n
        T1212=((B(1)^4)/(4*w^4))*((ln^2/(hn*kn))-((4*w^2)/(c^2)));
        T1213=-((4*pn(1)*w^2*kn)^-1);
        T1214=i*((B(1)^2)/(4*pn(1)*(w^3)*c))*((ln/((hn*kn)))-2);
        T1223=T1214;
        T1224=1/(4*pn(1)*(w^2)*hn);
        T1234=((4*pn(1)^2*w^4)^-1)*((w^2)/(c^2*hn*kn))-1);
        R1212=T1212;
        R1213=T1213;
        R1214=T1214;
        R1224=T1224;
        R1234=T1234;
        R1223=T1223;
        %MOVE UP A LAYER
        l=l-1;
    end
    if l~= n %Algorithm for all layers except last layer
        hn=sqrt(((k)^2)-(w^2/(a(1)^2)));
        kn=sqrt(((k)^2)-(w^2/(B(1)^2)));
        ln=2.*(k)^2-(w^2/(B(1)^2));
        un=pn(1)*B(1)^2;
        hhn=hn/k; %This IS hn tilda
        kkn=kn/k; %This is kn tilda
        SH=(sinh((hn*dn(1))))/hhn;
        CH=cosh((hn*dn(1)));
        SK=(sinh(kn*dn(1)))/kkn;
        CK=cosh(kn*dn(1));
    end
end
```

```

yn=-(2*B(1)^2)/(c^2);
p1=yn+1;
p2=2*yn*(yn+1);
p3=(yn+1)^2;
p4=2*yn+1;
m=-pn(1)*c*w;
%DEFINE THE G MATRIX
G1212=-p2+(p2+1)*CH*CK-(p3+yn^2*hhn^2*kkn^2)*SH*SK;
G3434=G1212;
G1312=-m*(yn^2*kkn^2*CH*SK-p3*SH*CK);
G3424=G1312;
G1412=-i*m*((p2/2)*p4*(1-CH*CK)+(p1^3+yn^3*hhn^2*kkn^2)*SH*SK);
G2312=G1412;
G3414=G1412;
G3423=G1412;
G2412=-m*[p3*CH*SK-yn^2*hhn^2*SH*CK];
G3413=G2412;
G3412=-m^2*((p2^2)/2)*(1-CH*CK)+[p3^2+yn^4*hhn^2*kkn^2]*SH*SK);
G1213=m^-1*(-CH*SK+hhn^2*SH*CK);
G2434=G1213;
G1313=CH*CK;
G2424=G1313;
G1413=-i*[p1*CH*SK-yn*hhn^2*SH*CK];
G2313=G1413;
G2414=G1413;
G2423=G1413;
G2413=-hhn^2*SH*SK;
G1214=-i*m^-1*(p4*(1-CH*CK)+(p1+yn*hhn^2*kkn^2)*SH*SK);
G1223=G1214;
G1434=G1214;
G2334=G1214;
G1314=i*(p1*SH*CK-yn*kkn^2*CH*SK);
G1323=G1314;
G1424=G1314;
G2324=G1314;
G1414=1+p2*(1-CH*CK)+[p3+yn^2*hhn^2*kkn^2]*SH*SK;
G2323=G1414;
G2314=G1414-1;
G1423=G2314;
G1224=m^-1*(SH*CK-kkn^2*CH*SK);
G1334=G1224;
G1324=-kkn^2*SH*SK;
G1234=-i*m^-2*(2*(1-CH*CK)+(1+hhn^2*kkn^2)*SH*SK);
r1212=R1212*G1212+R1213*G1312+R1214*G1412+R1223*G2312+R1224*G2412...
+R1234*G3412;
r1213=R1212*G1213+R1213*G1313+R1214*G1413+R1223*G2313+R1224*G2413...
+R1234*G3413;
r1214=R1212*G1214+R1213*G1314+R1214*G1414+R1223*G2314+R1224*G2414...
+R1234*G3414;
r1223=R1212*G1223+R1213*G1323+R1214*G1423+R1223*G2323+R1224*G2423...
+R1234*G3423;
r1224=R1212*G1224+R1213*G1324+R1214*G1424+R1223*G2324+R1224*G2424...
+R1234*G3424;
r1234=R1212*G1234+R1213*G1334+R1214*G1434+R1223*G2334+R1224*G2434...
+R1234*G3434;

R1212=r1212;
R1213=r1213;
R1214=r1214;
R1224=r1224;
R1234=r1234;
end
%GO UP ONE LAYER
l=l-1;
end
H=R1212;

```

The following MATLAB® code was written by the author after translating it from Schwab and Knopoff's (1972) Love wave dispersion Fortran code. This code performs exactly the same function as the above Rayleigh wave dispersion function code, but for the Love wave. This function inputs angular frequency, Love wave phase velocity, and the following parameters of a layered model:  $V_s, \rho, h$ , for each layer.

```

%THIS IS A MATLAB TRANSLATION OF THE ORIGINAL CODE BY F.A. SCHWAB AND L.
%KNOPOFF (1972) - TRANSLATED BY BRIAN SAM SHAMS (IAG - 2015)
%COMPUTATION OF THE LOVE-WAVE DISPERSION FUNCTION 'FLOVE'
function FLOVE=fLove(parameters,c,w)
%DEFINE VARIABLES
n = length(parameters)/4;
N = n; %The layer number of the Half Space (or the total number of
layers)
OMEGA=w; %Angular frequency
C = c; %PHASE VELOCITY
B = parameters((n+1):(n+1+n-1)); %Shear wave velocities (Vs) Vector
BSQ = B.^2; %Vs squared
THKNES = parameters((3*n+1):(3*n+1+n-1)); %Layer thicknesses Vector
RHO = parameters((2*n+1):(2*n+1+n-1)); %Densities Vector
BETNSQ = B(end)^2; % squared Vs of Half Space layer (N)
NMNUS2 = N-2; %N minus 2
BSQRHN = BETNSQ*RHO(end); %The Rigidity as defined by Haskell (1953)
%SET LEFT-HAND MATRIX OF EQ. (10).
CSQ = C^2;
if BETNSQ == 0
    RBNMN = 0;
else
    RBNMN = -sqrt(1-CSQ/BETNSQ)*BSQRHN;
end
XK=OMEGA/C;
C11=RBNMN;
C12=-1;
%COMPUTE THE MATRIX PRODUCT TO THE LEFT OF THE RIGHT-HAND MATRIX IN EQ.
%(10)
for layer = 1:NMNUS2
    M=N-layer;
    BETMSQ=BSQ(M);
    ARGBTM=1-CSQ/BETMSQ;
    if ARGBTM > 0
        RBETAM=-sqrt(ARGBTM);
        RBMMM=RBETAM*BETMSQ*RHO(M);
        EXPPQM=0.5*exp(XK*RBETAM*THKNES(M));
        EXPMQM=0.25/EXPPQM;
        SINQM=EXPPQM-EXPMQM;
        B11=EXPPQM+EXPMQM;
        B21=-RBMMM*SINQM;
        TEMP=C11*B11-C12*B21;
        C12=C11*SINQM/RBMMM+C12*B11;
        C11=TEMP;
    elseif ARGBTM == 0 %GO to 170
        continue
    else
        RBETAM=sqrt(-ARGBTM);
        QM=XK*RBETAM*THKNES(M);
        RBMMM=RBETAM*BETMSQ*RHO(M);

```

```

        SINQM=sin(QM);
        B11=cos(QM);
        B21=RBMMM*SINQM;
        TEMP=C11*B11-C12*B21;
        C12=C11*SINQM/RBMMM+C12*B11;
        C11=TEMP;
    end
end
%INCLUDE THE RIGHT-HAND MATRIX OF EQ.(10) IN THE MATRIX PRODUCT.
BETMSQ=BSQ(1);
ARGBTM=1-CSQ/BETMSQ;
if ARGBTM > 0
    RBETAM=-sqrt(ARGBTM);
    EXPPQM=0.5*exp(XK*RBETAM*THKNES(1));
    EXPMQM=0.25/EXPPQM;
    B11=EXPPQM+EXPMQM;
    B21=-RBETAM*BETMSQ*RHO(1)*(EXPPQM-EXPMQM);
    FLOVE=C11*B11-C12*B21;
elseif ARGBTM == 0
    FLOVE=C11;
else
    RBETAM=sqrt(-ARGBTM);
    QM=XK*RBETAM*THKNES(1);
    B11=cos(QM);
    B21=RBETAM*BETMSQ*RHO(1)*sin(QM);
    FLOVE=C11*B11-C12*B21;
end
FLOVE=real(FLOVE);
end

```

## Appendix C

### Synthetic Model Inversions with MATLAB® Code

#### Model 1: A Simple Two-Layer Model

Layer number	$v_s$ (m/s)	$v_p$ (m/s)	$\rho$ (g/cm <sup>3</sup> )	$h$ (m)
1	100	340	1.8	10
Half-Space	500	1860	2.0	$\infty$

Figure C.1 - Properties of a simple two-layer model (1).

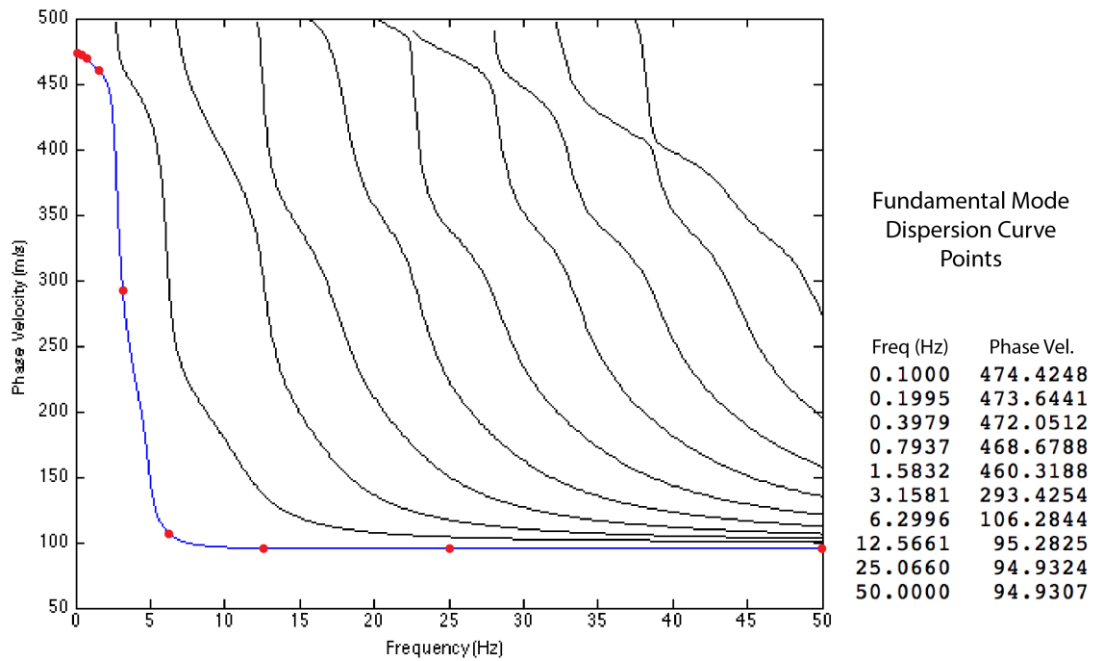


Figure C.2 - A graph showing the 10 points used for inversion of the fundamental mode of the dispersion curves for model 1.

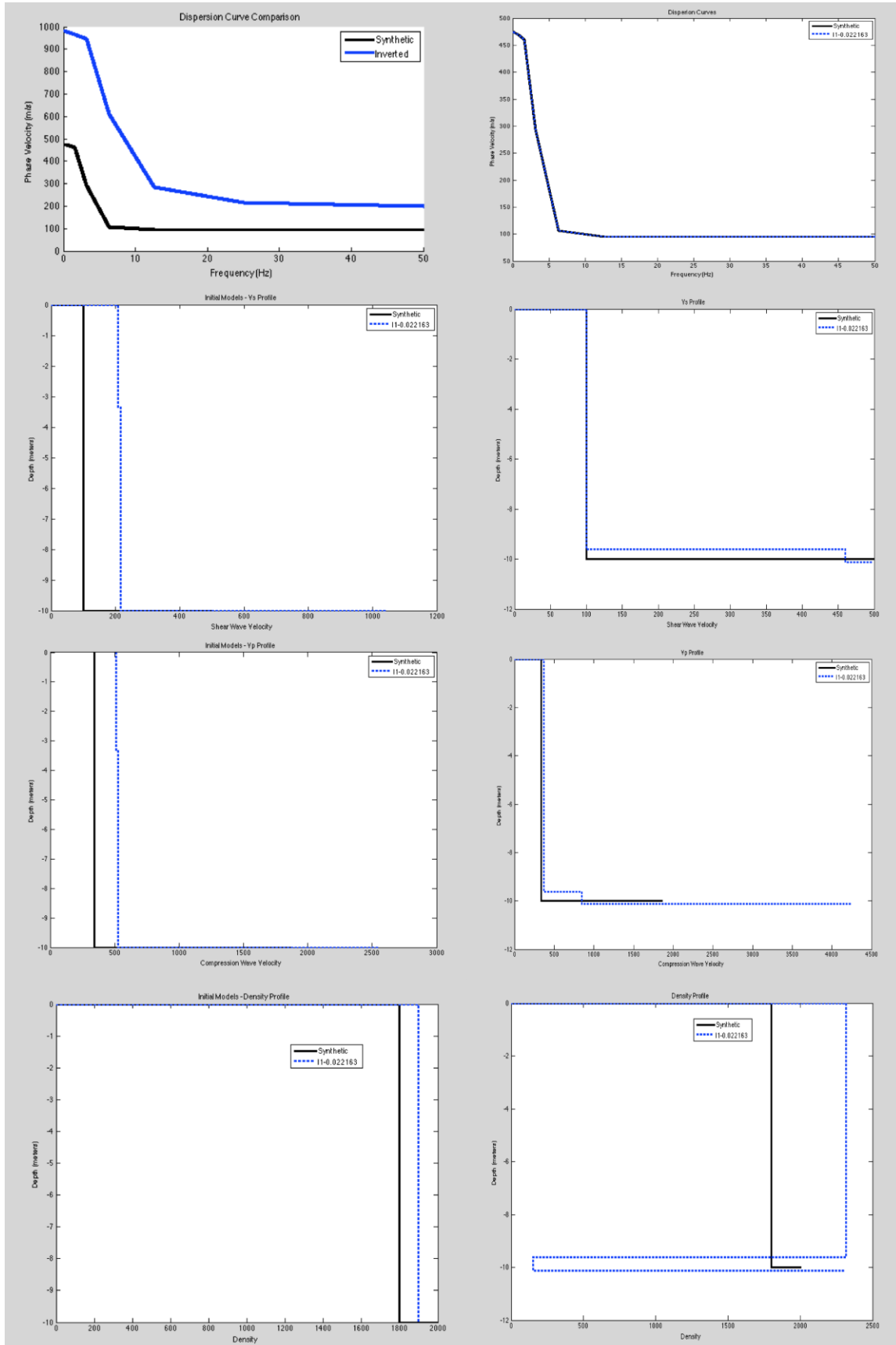


Figure C.3 - Results of the inversion of model 1, using an initial model as shown on the left for each parameter and the corresponding dispersion curve on top left. The right side shows the inverted parameters and dispersion curve on top. Inversion completed using *fminsearch* after 1300 iterations, with Euclidian distance of dispersion curves as *obj. func.*

**Model 2: A Six-Layer Model from Xia et al., 1999**

Layer number	$v_s$ (m/s)	$v_p$ (m/s)	$\rho$ (g/cm <sup>3</sup> )	$h$ (m)
1	194	650	1.82	2.0
2	270	750	1.86	2.3
3	367	1400	1.91	2.5
4	485	1800	1.96	3.8
5	603	2150	2.02	3.2
Half-Space	740	2800	2.09	$\infty$

Figure C.4 – Properties of model 2 (from Xia et al., 1999).

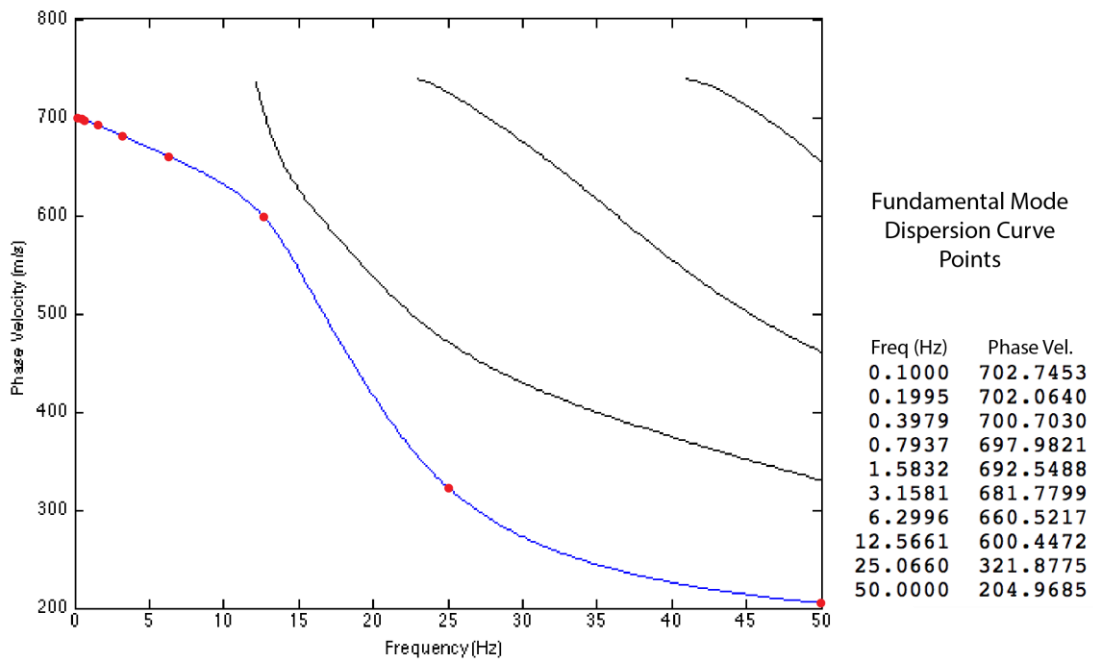


Figure C.5 - A graph showing the 10 points used for inversion of the fundamental mode of the dispersion curves for model 2 (same model used in Xia et al., 1999).

Initial Dispersion curves  
not shown

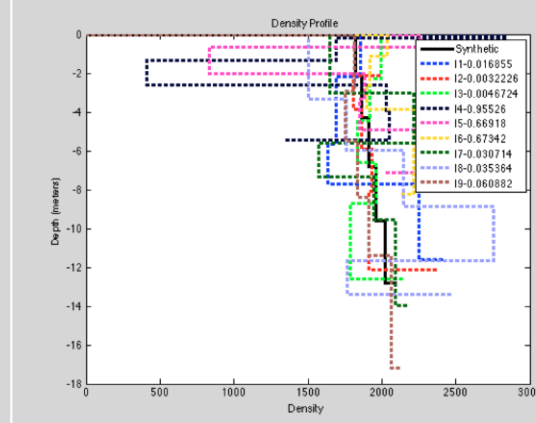
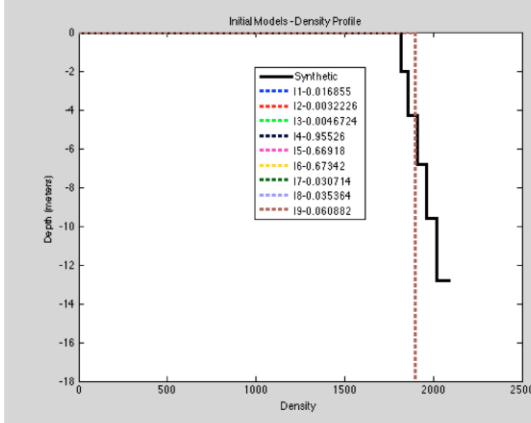
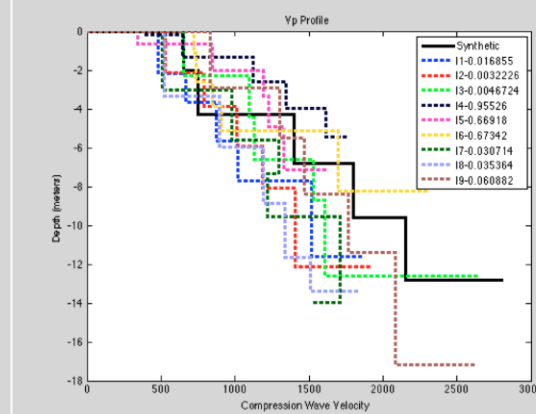
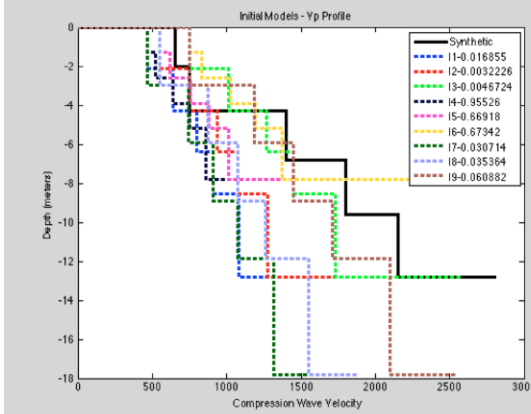
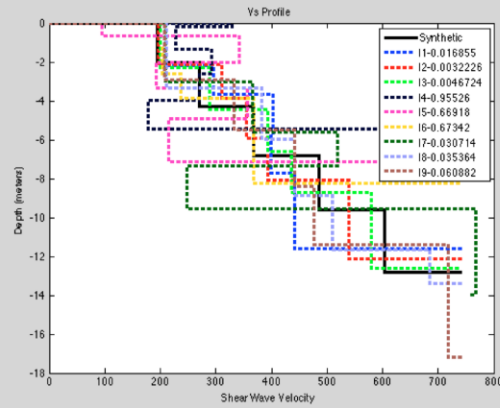
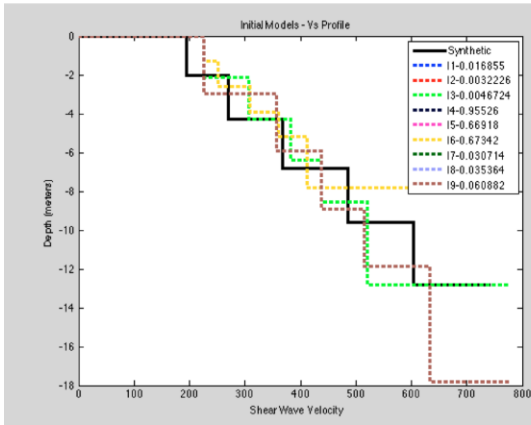
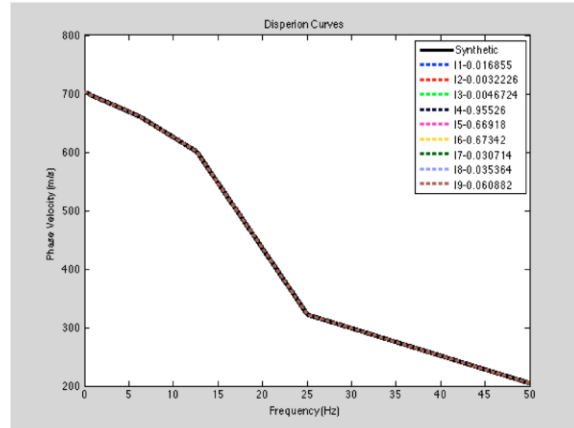


Figure C.6 - Results of the inversion of model 2, using 9 initial models that vary depth to Half-Space and Poisson's ratio. Inversion results for each parameter are shown on the right. Lines overlap in some occasions. Inversion completed using `fminsearch` after 5000 iterations, with Euclidian distance of dispersion curves as obj. function.

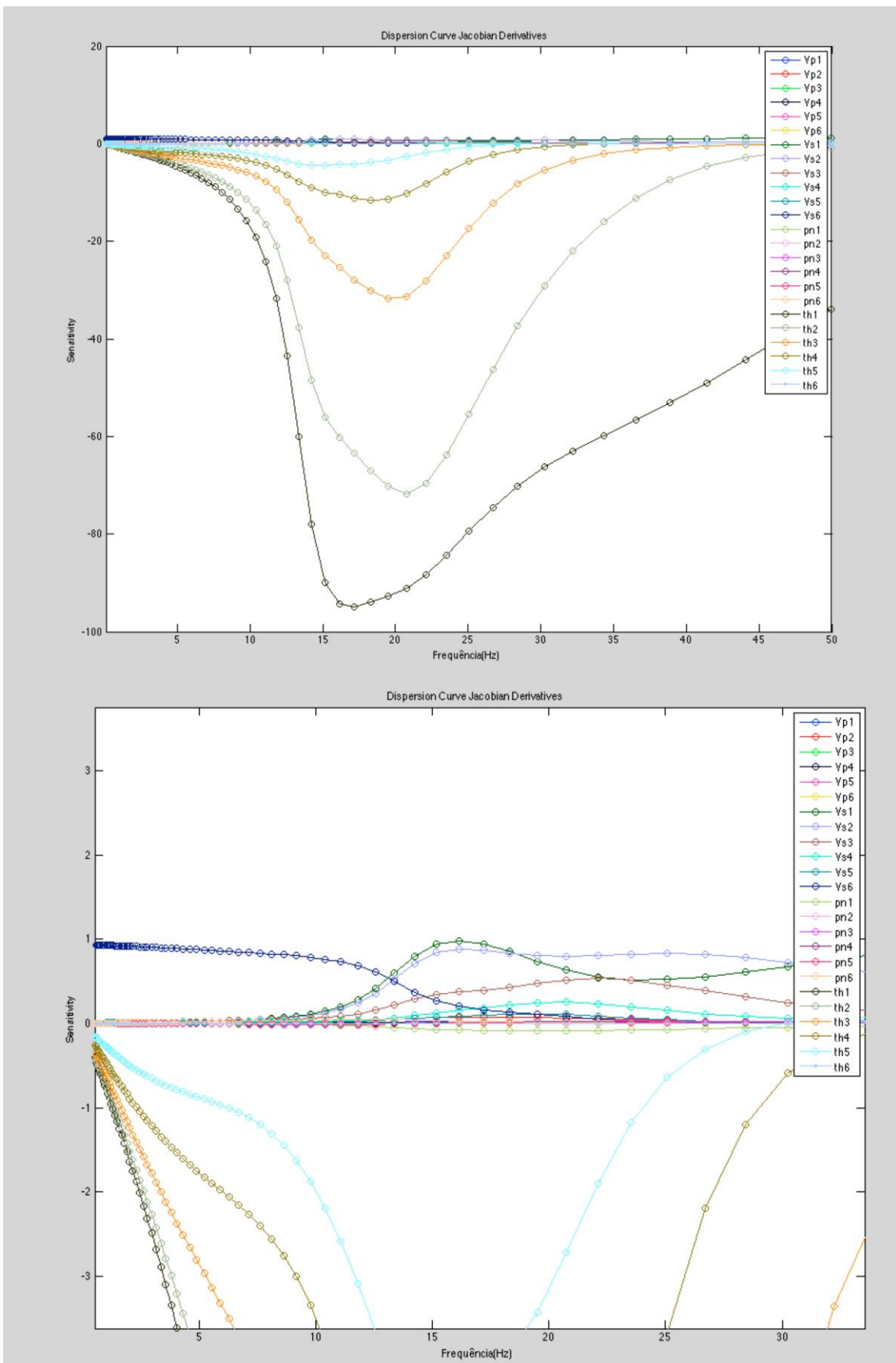


Figure C.7 – Sensitivity Analysis of each parameter for model 2 (same model used in Xia et al., 1999).

# Appendix D

## Refraction Data

### D.1 – SH Wave Refraction Data

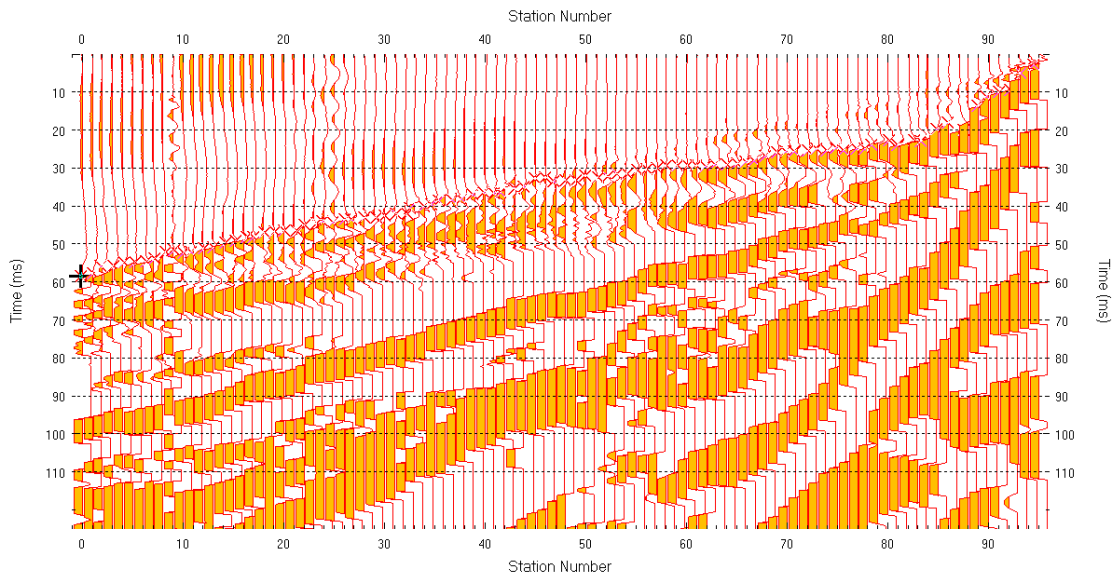


Figure D.1 - Picked arrivals for near shot offset.

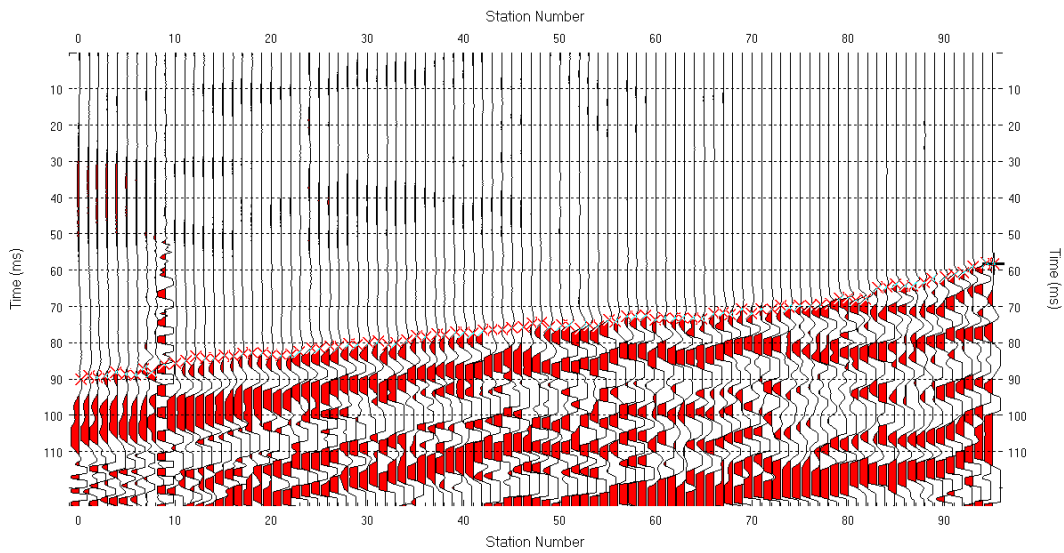


Figure D.2 - Picked arrivals for medium shot offset.

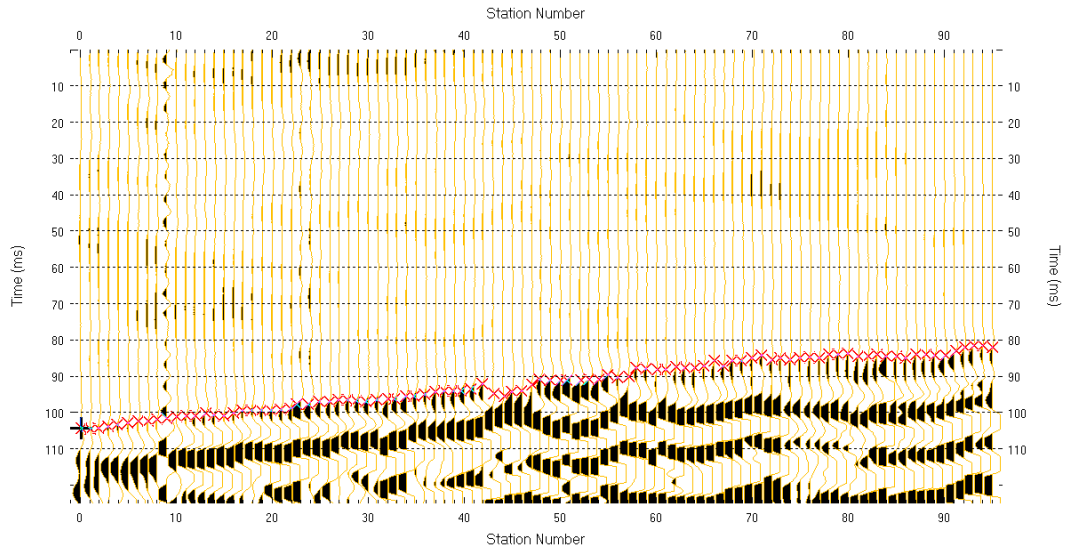


Figure D.3 - Picked arrivals for far shot offset.

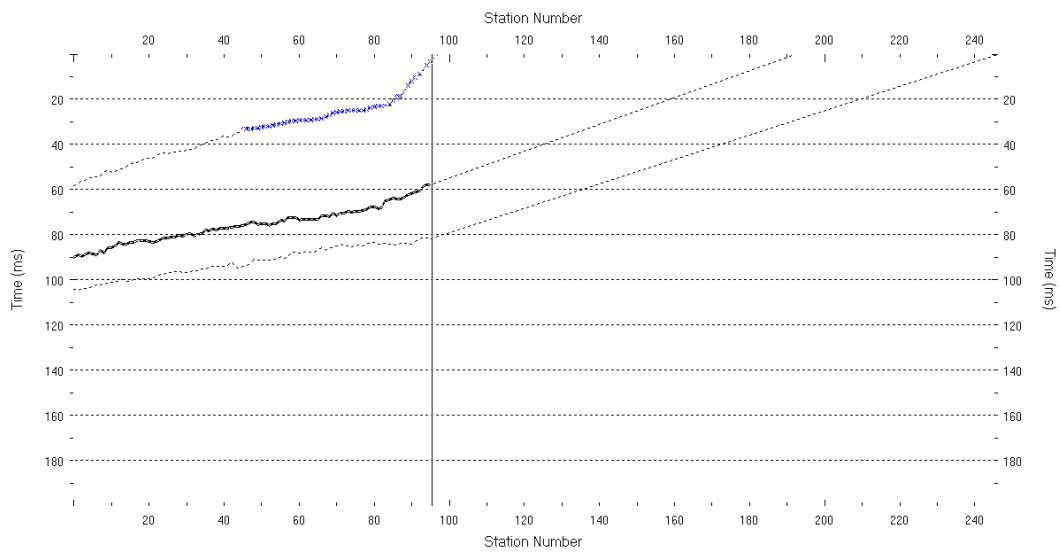
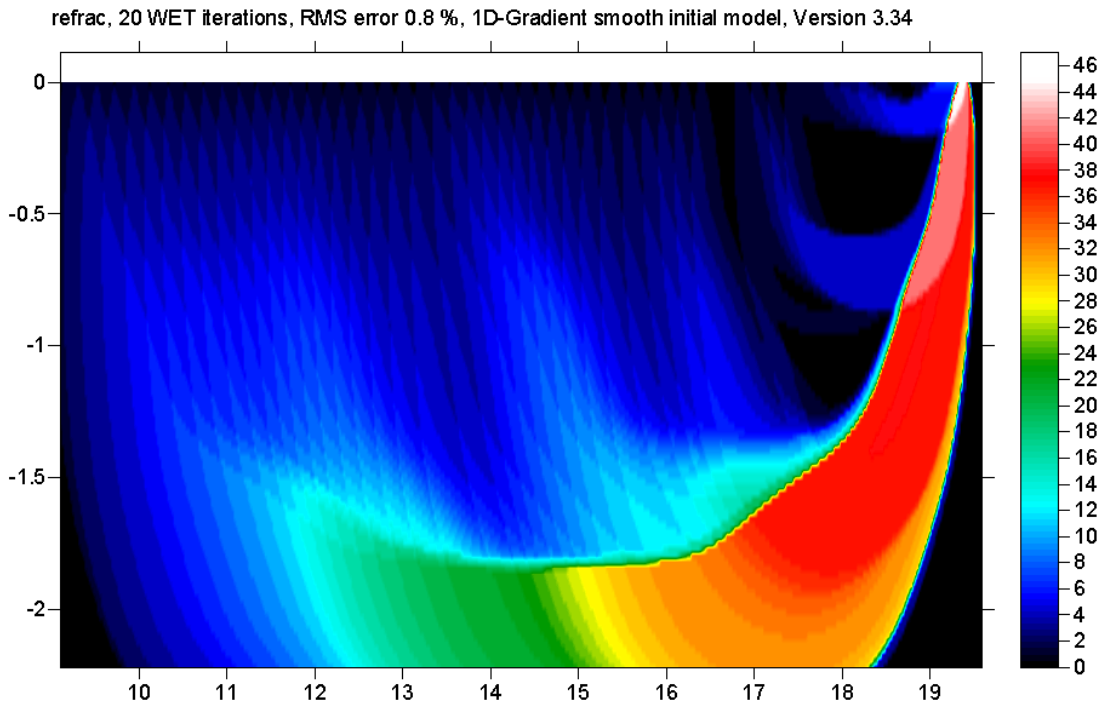
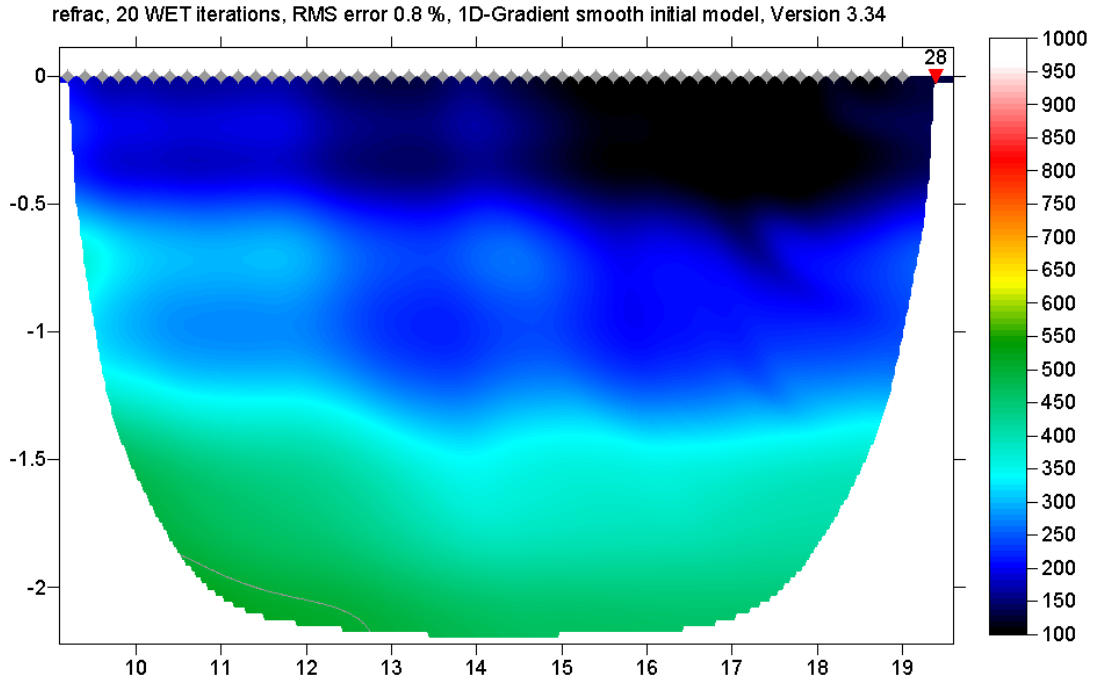
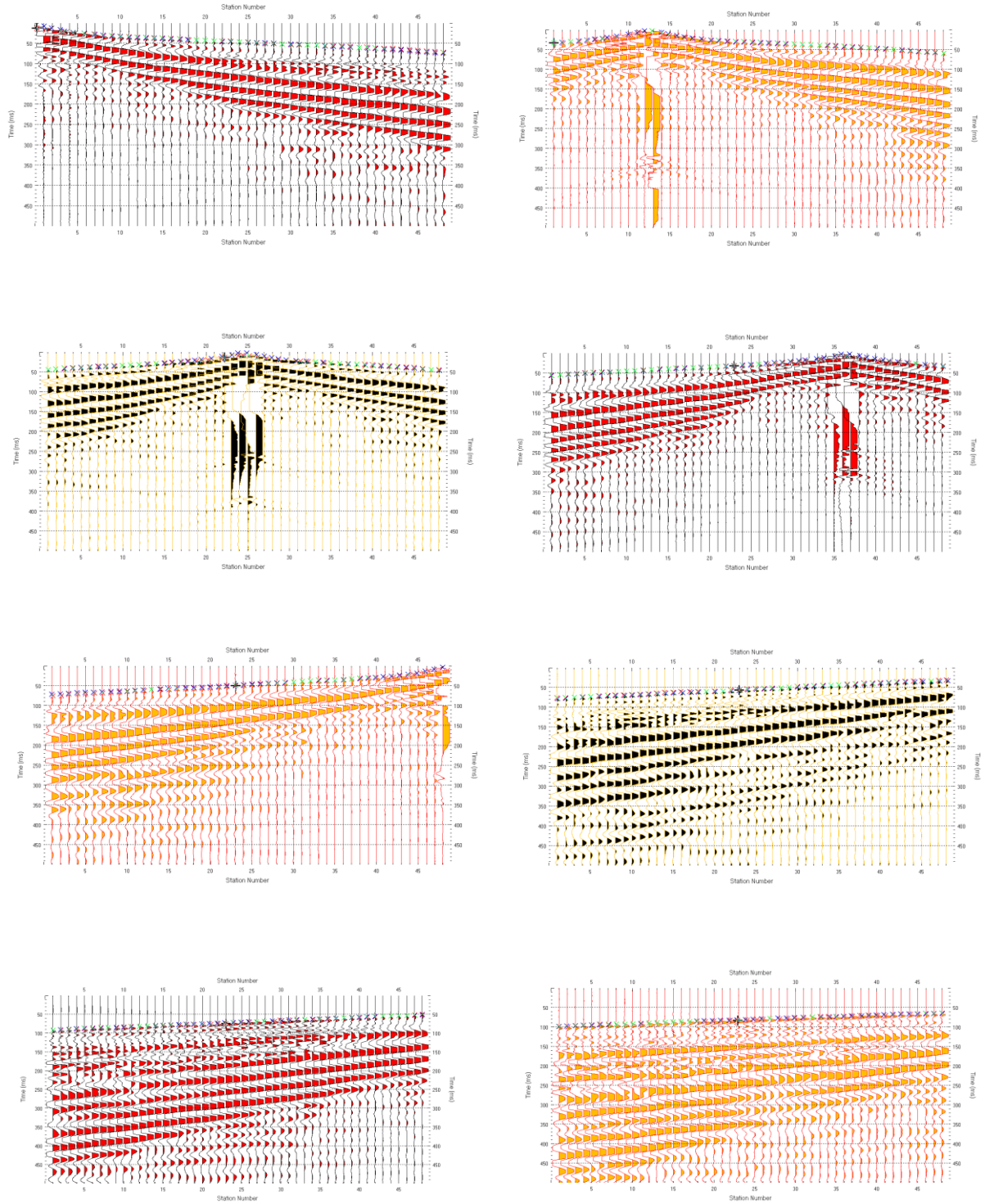
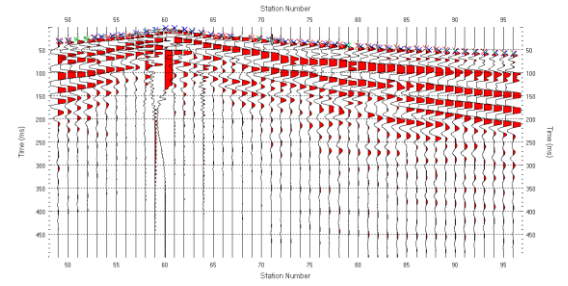
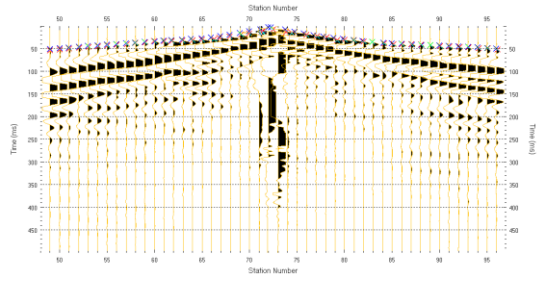
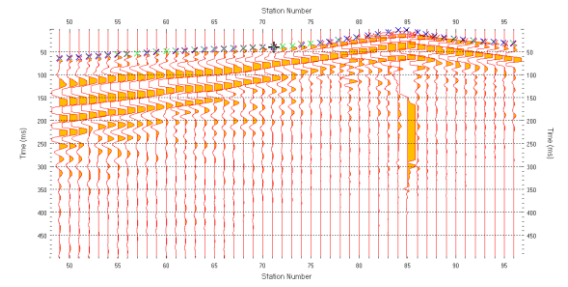
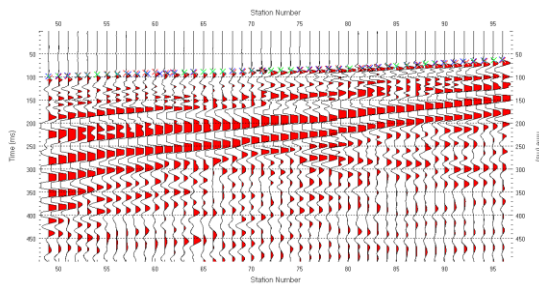
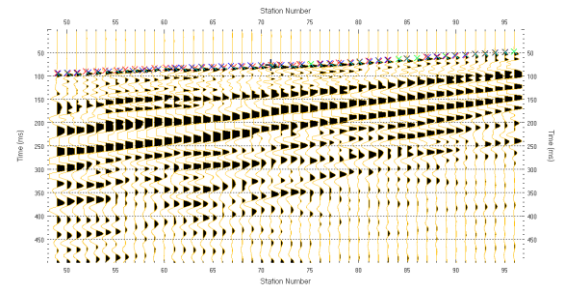
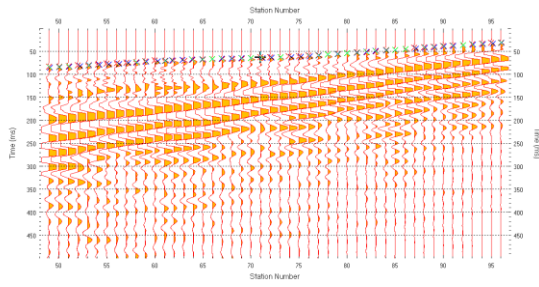
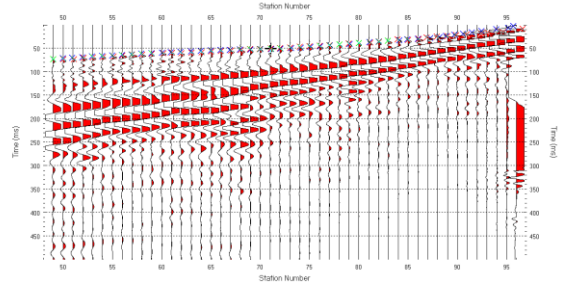
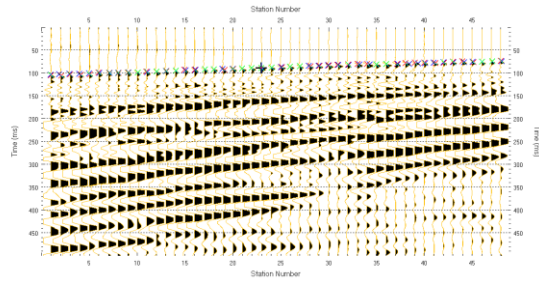


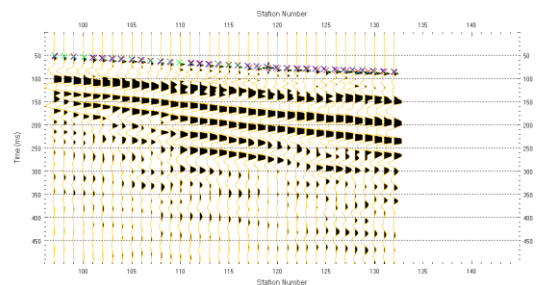
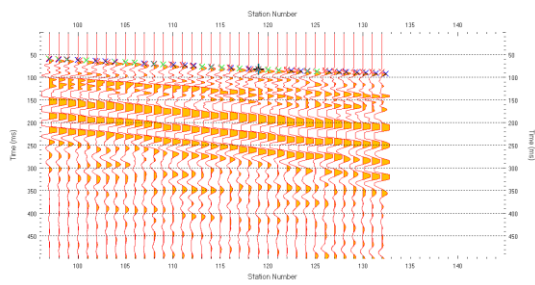
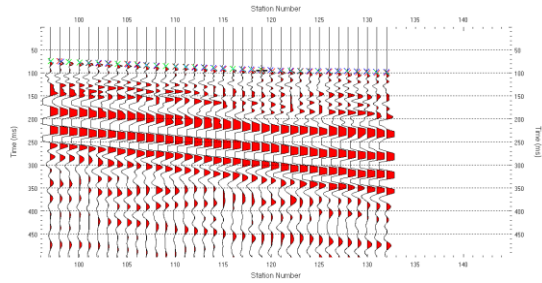
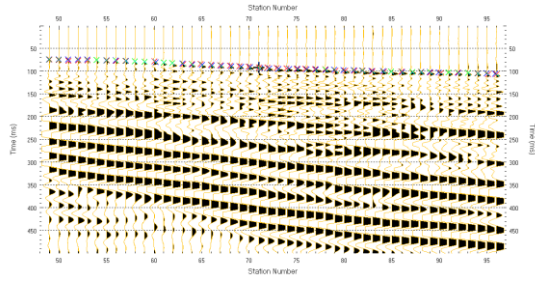
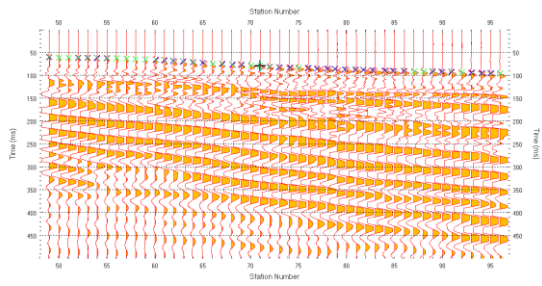
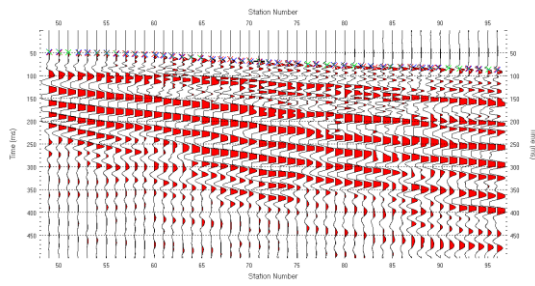
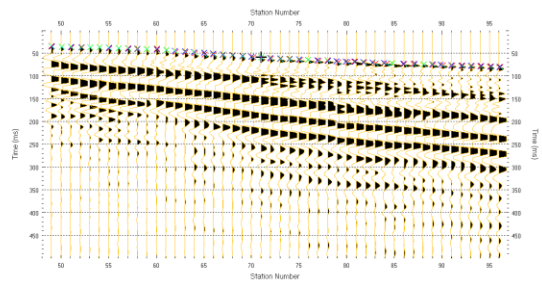
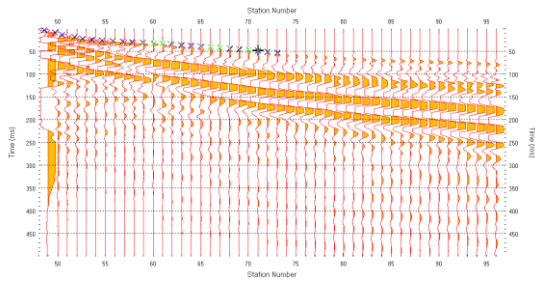
Figure D.4 - Travel time curves.



## D.2 – P Wave Refraction Data







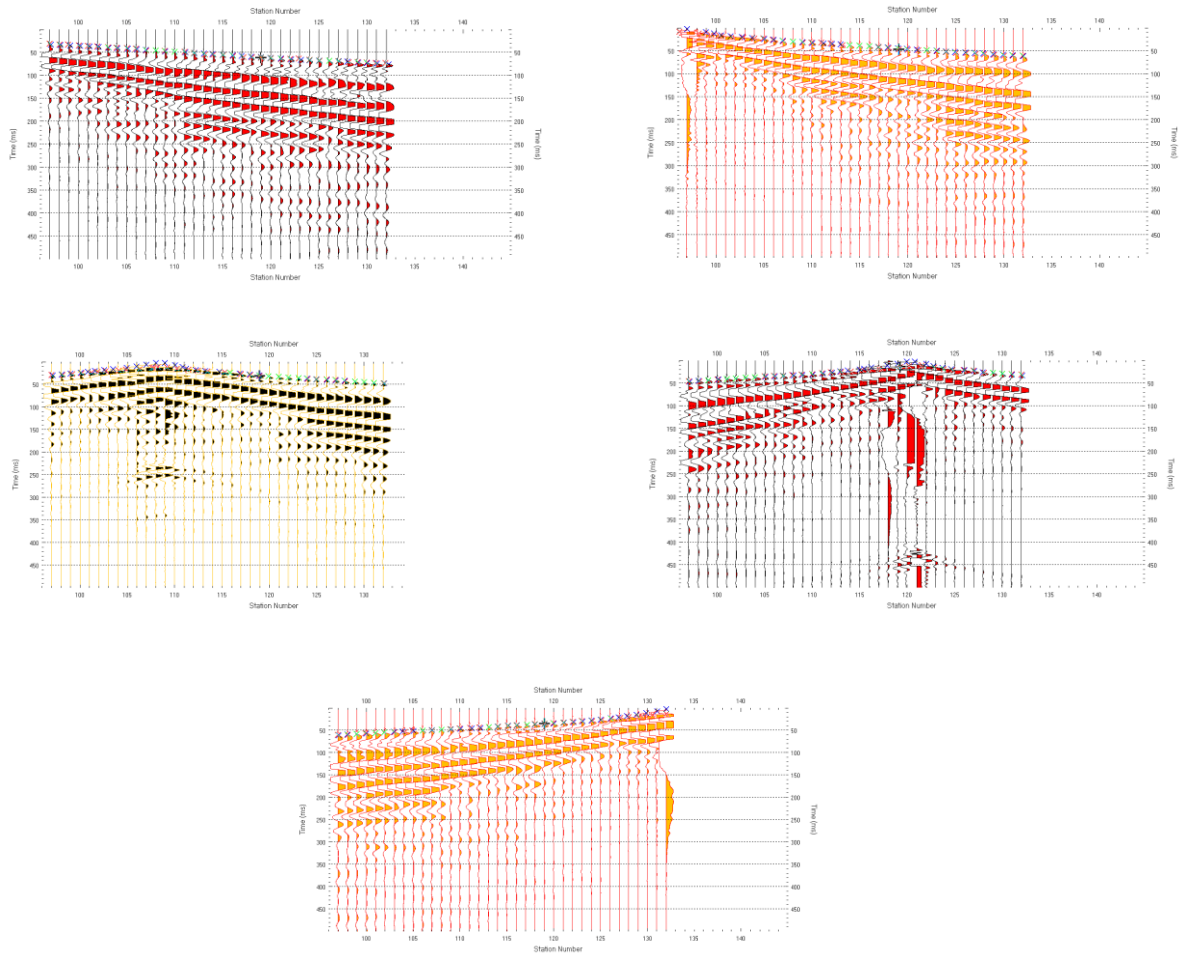


Figure D.7 - All the seismographs with picked first arrivals used for P wave refraction analysis.

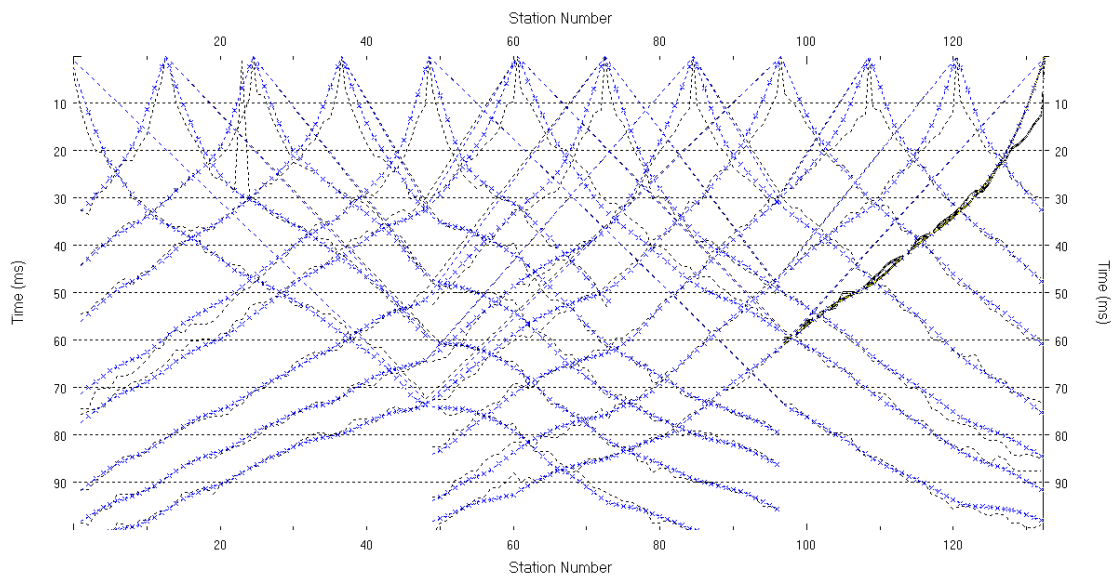


Figure D.8 – Travel time curves.

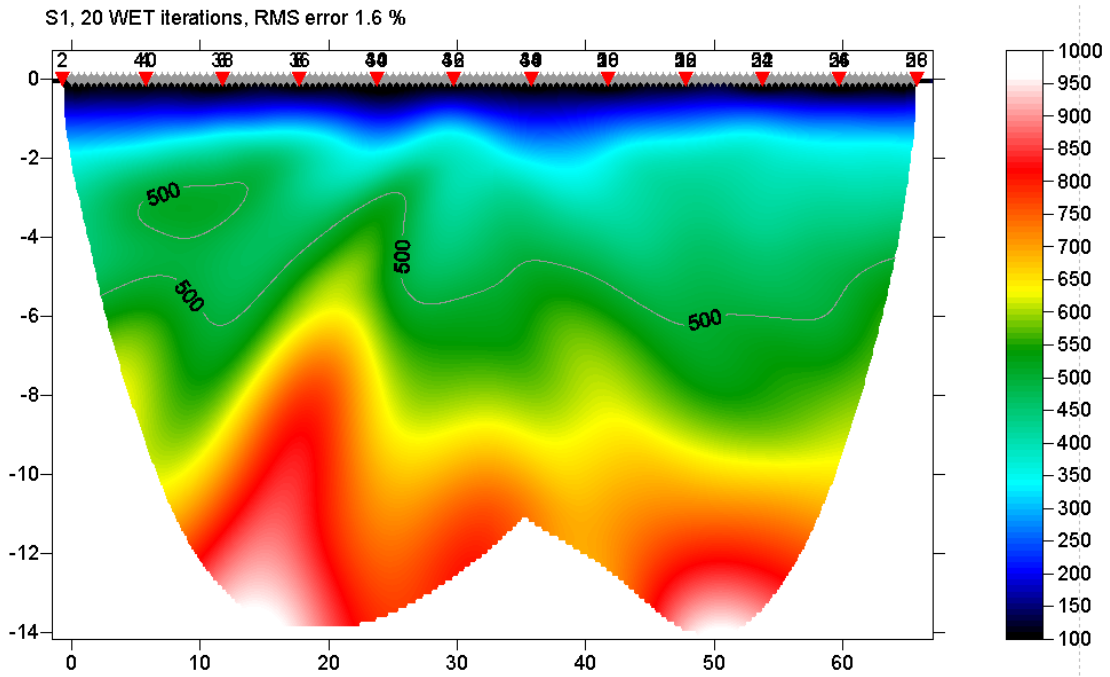


Figure D.9 - Smoothed WET inversion of P refraction data.

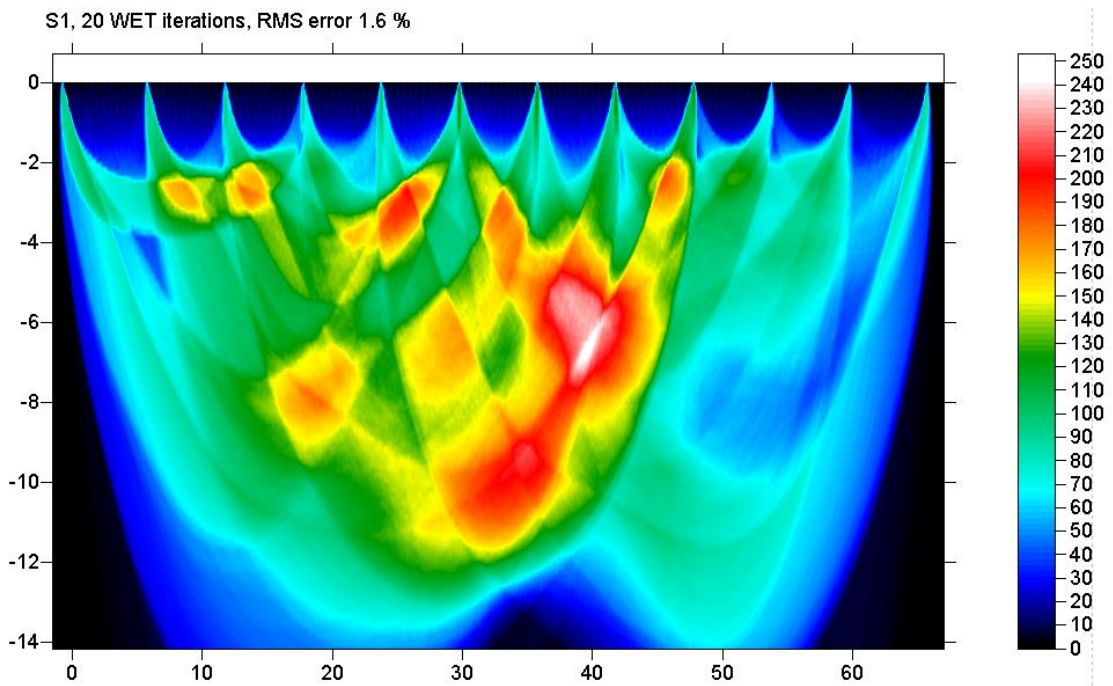


Figure D.10 - Wave coverage of P refraction data.

# Appendix E

## MASW Analysis Data

### E.1 – MASW of Short Arrays

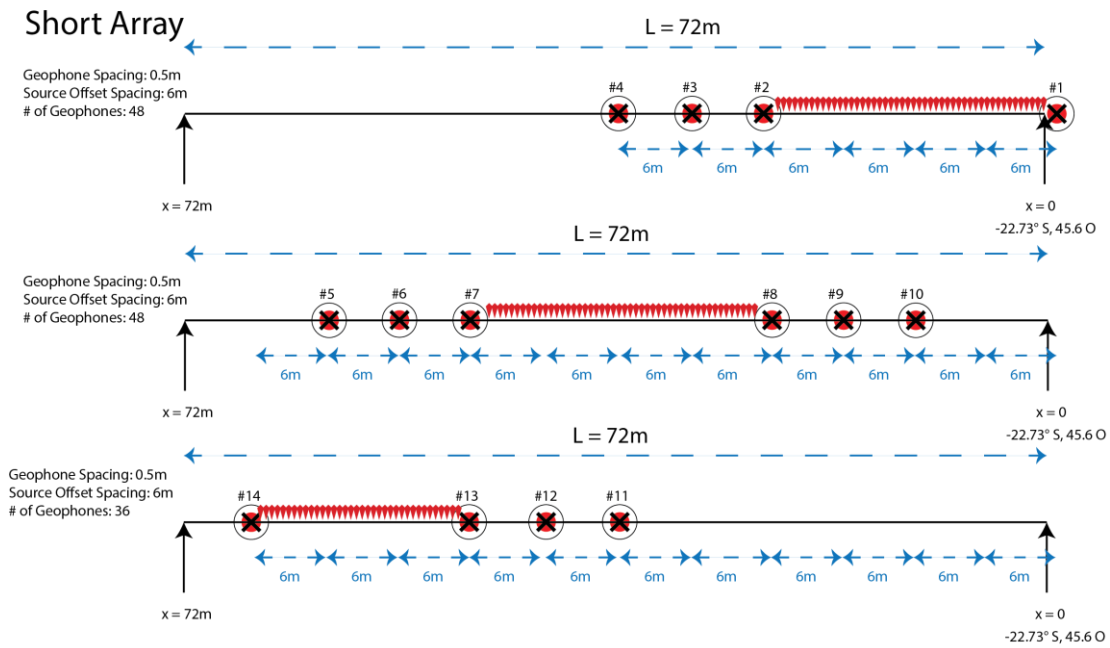
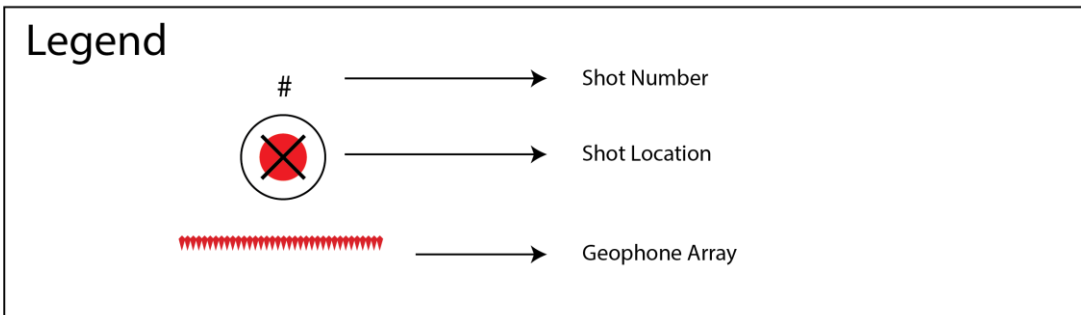
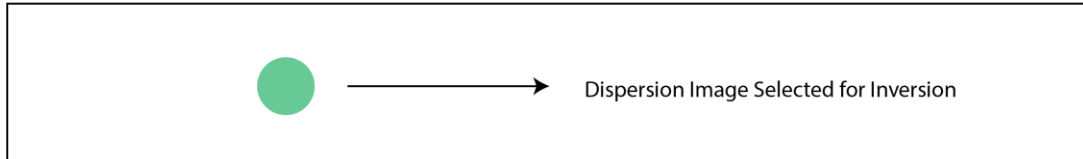


Figure E.1 - Diagram of shot locations and geophone array setup for the short arrays. The top two arrays have a length of 23.5 m, and the bottom array is 17.5 m long.



### E.1.1 – Selection of Best Dispersion Images



### Dispersion Images Midpoint (x = 12m)

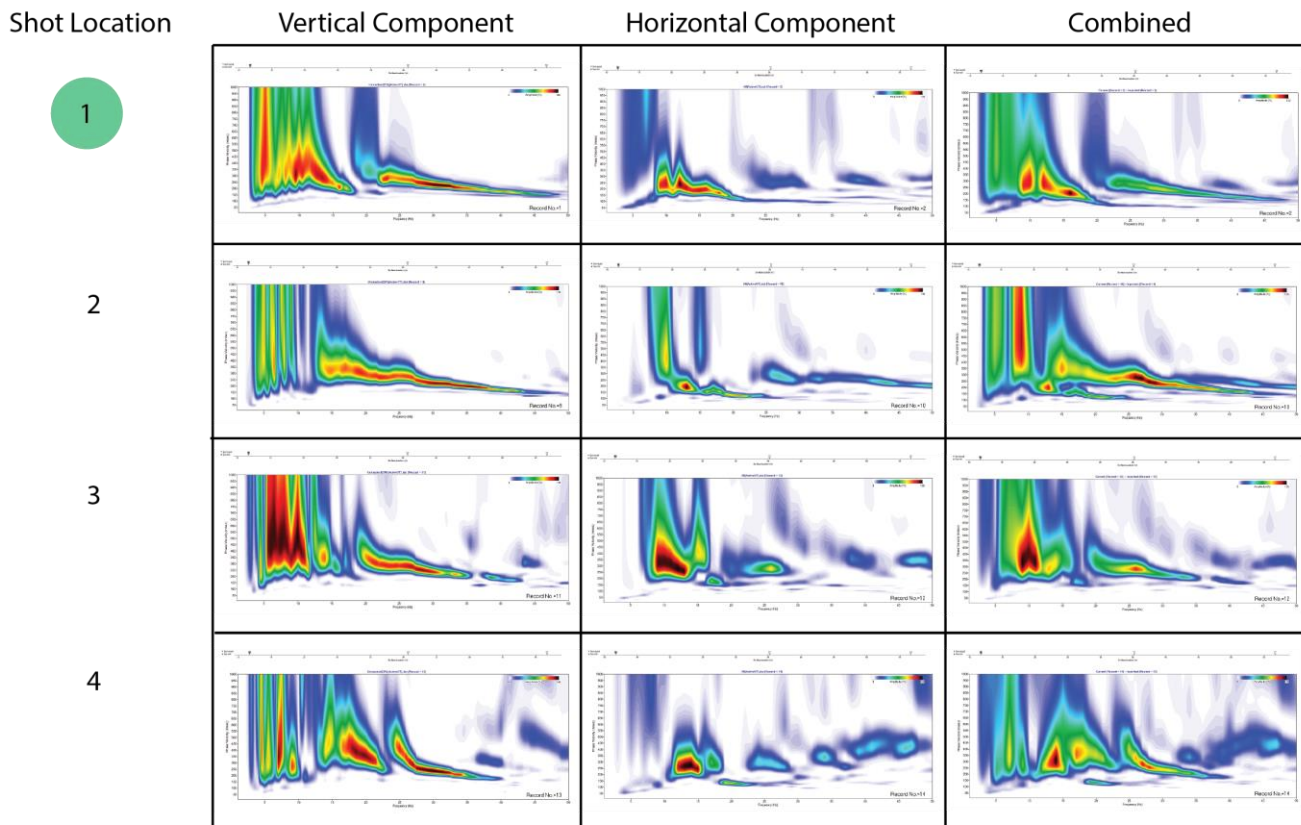


Figure E.2 - Dispersion images for the top array from (Figure 65) for a variety of shot locations. Horizontal and vertical components are shown separately and then combined. The best image is selected by the green circle.

## Dispersion Images Midpoint (x = 36m)

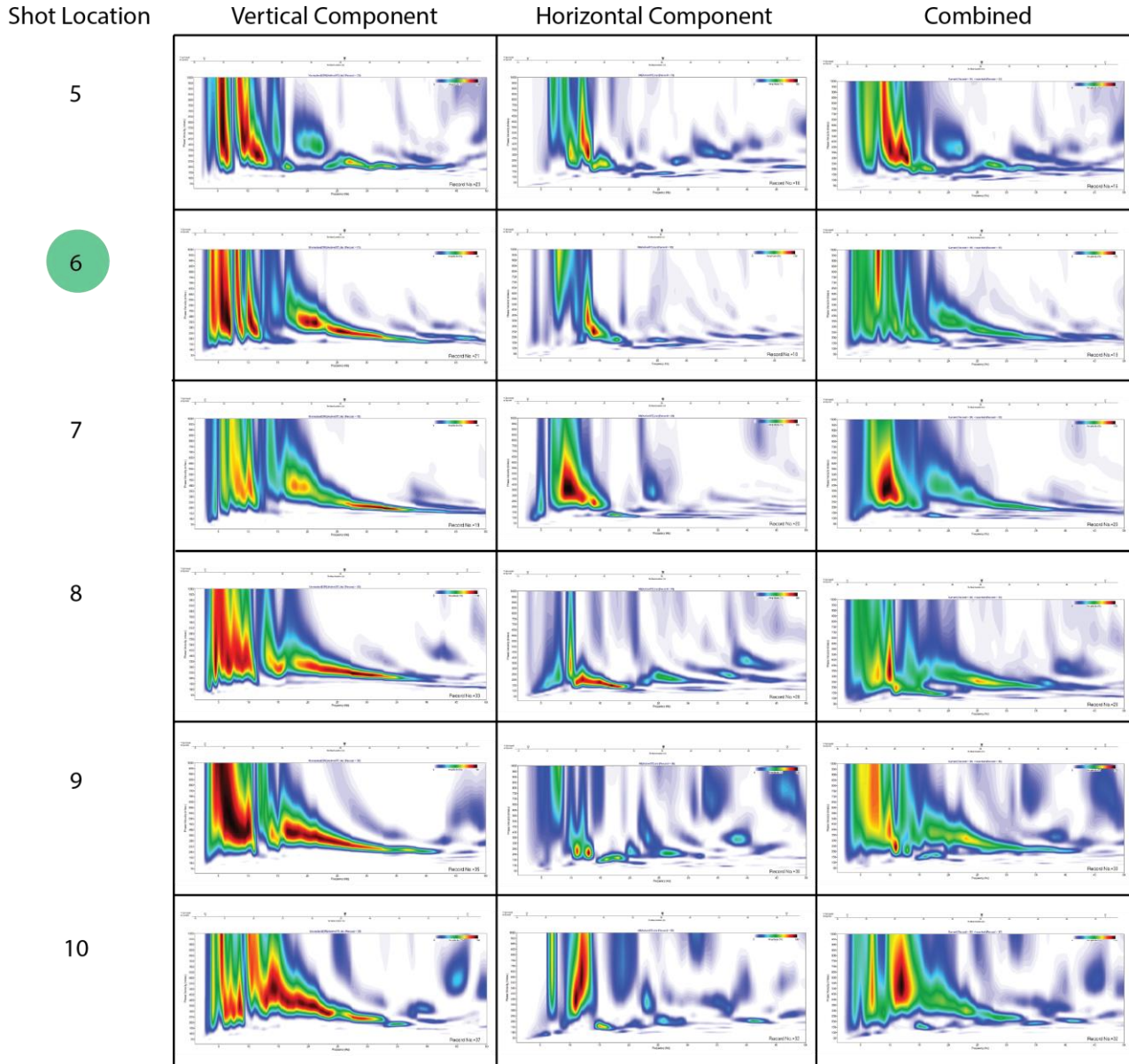
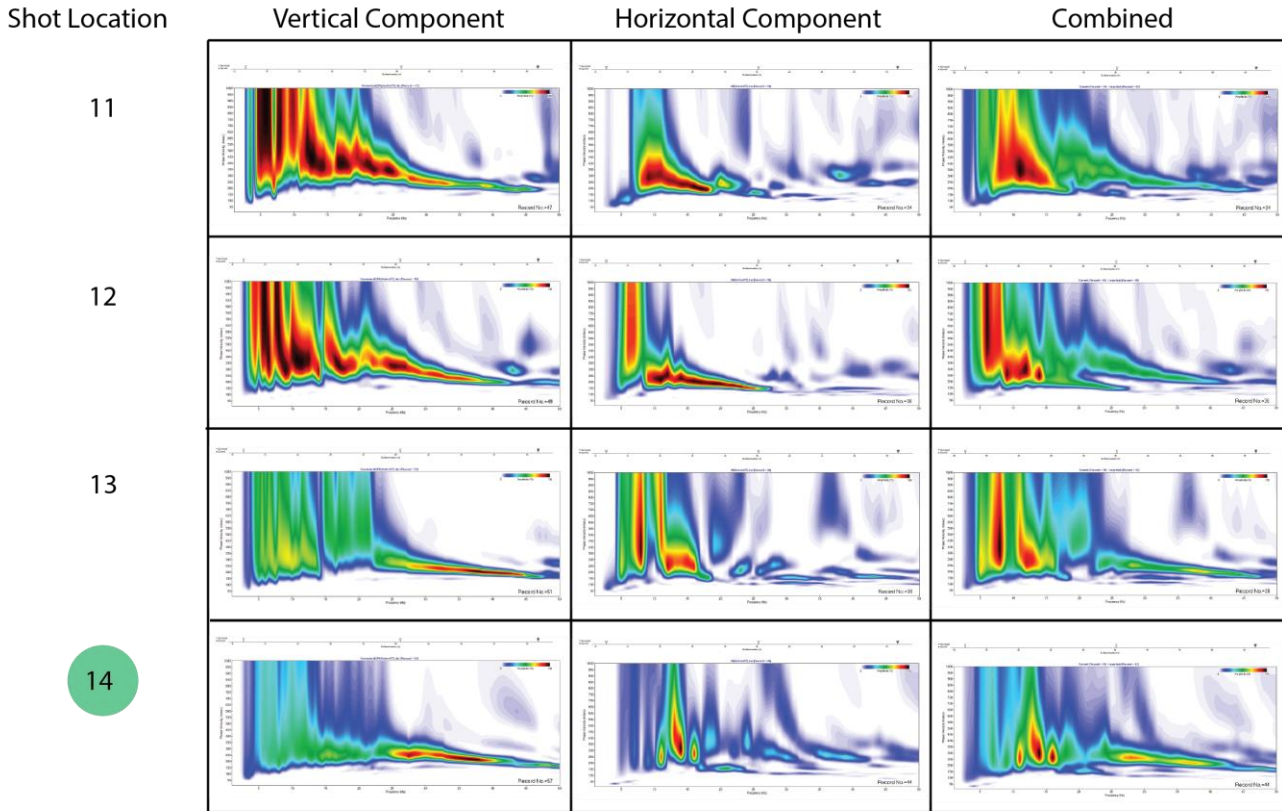


Figure E.3 - Dispersion images for the middle array from (Figure 65) for a variety of shot locations. Horizontal and vertical components are shown separately and then combined. The best image is selected by the green circle.

## Dispersion Images Midpoint (x = 57m)



14

*Figure E.4 - Dispersion images for the bottom array from (Figure 65) for a variety of shot locations. Horizontal and vertical components are shown separately and then combined. The best image is selected by the green circle.*

## E.1.2 – Dispersion Curve Selection & Inversion

# Dispersion Curve Selection

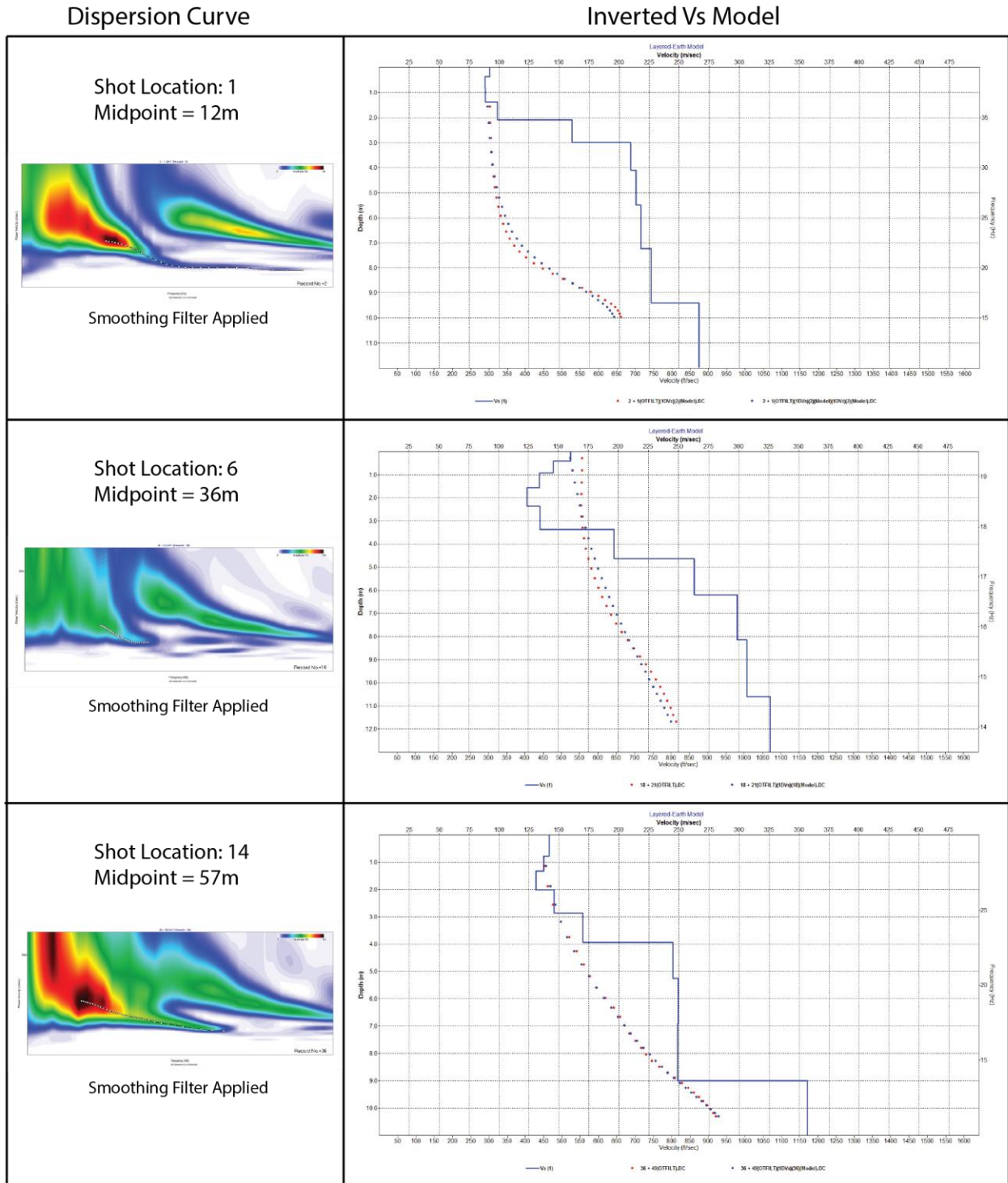
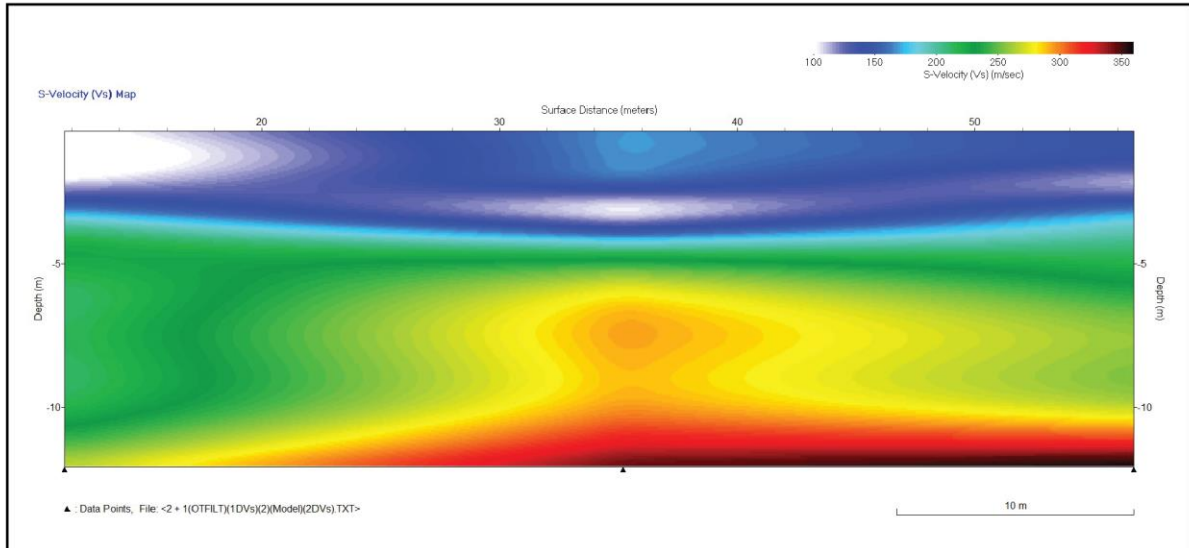


Figure E.5 - Individual inversions of the picked dispersion curves (left) of the best dispersion images for each short array.

## Interpolated 2D Vs Profile



## Interpolated 2D Confidence Profile

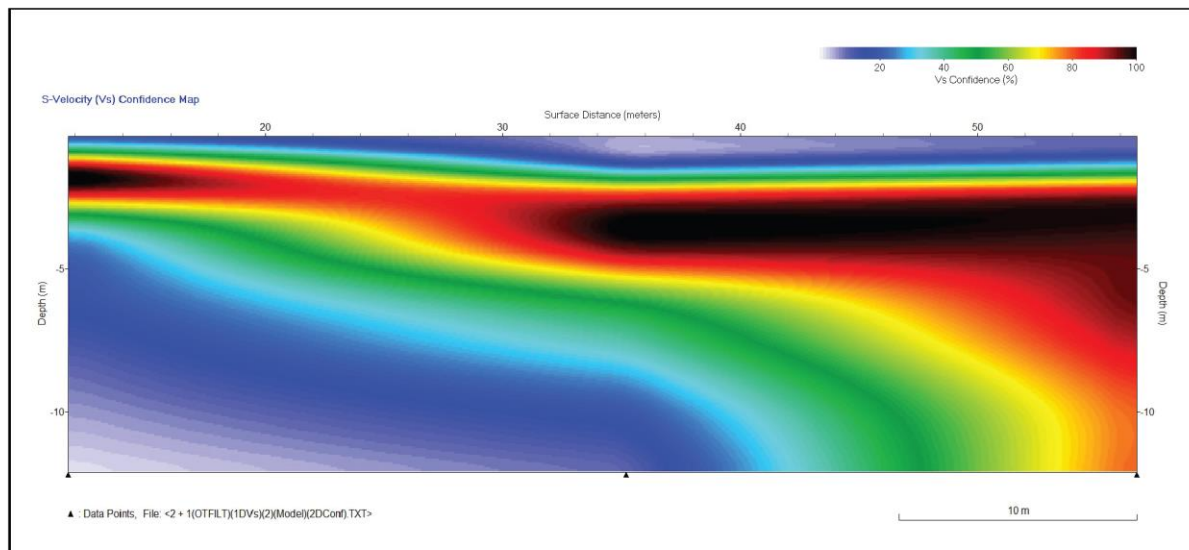


Figure E.6 – Interpolated 2-D shear wave velocity profile inversion, from 3 1-D inversions for each short array, using the default initial model in ParkSEIS© (top). Associated 2-D confidence profile (bottom). The confidence profile highlights the depths (from associated frequencies) where the dispersion curve is more sensitive, and where it is more sensitive, the more confidence there is in the inverted results. Note that the shallow interface around 3 meters has the most confidence, as this section influence the dispersion curve the most.

**A-Priori Inversion:**

Layer Parameters (2 + 1(OTFILT).DC

Layer	Bottom	Thickness	S-Vel (Vs)	P-Vel (Vp)	POS Ratio	Density (ρ)
1	1.000	1.000	150	240	0.179	1.335
2	2.000	1.000	250	400	0.179	1.500
3	4.000	2.000	280	500	0.272	1.651
4	12.000	8.000	300	600	0.333	1406.000
5	30.000	18.000	400	980	0.400	1.917
6	Half Space	Infinity	332	814	0.400	2.000

Figure E.7 - A-priori model inputted into SurfSeis© as the initial model in the inversion process.

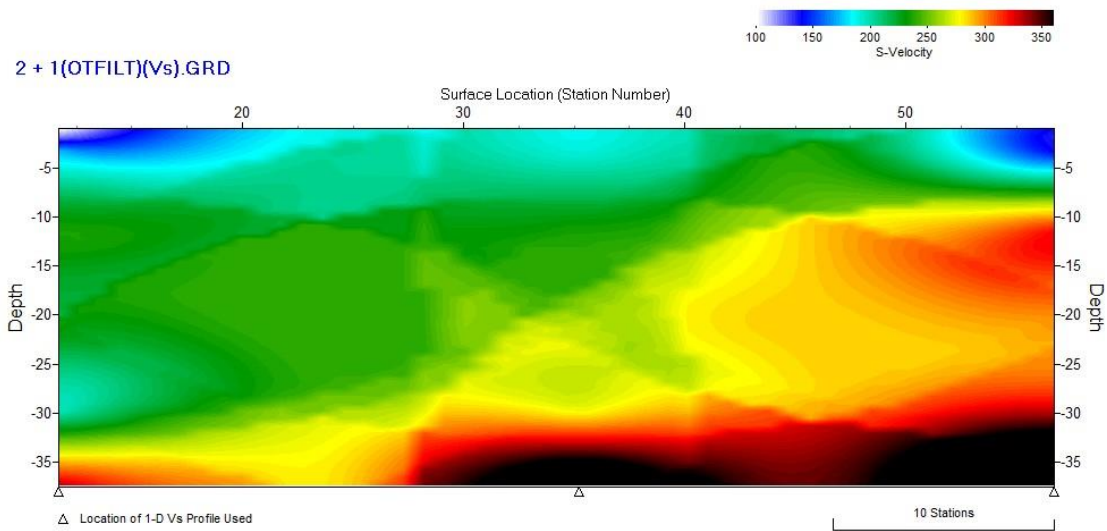


Figure E.8 - Interpolated 2-D inversion from three 1-D inversions of the shear wave velocity profile from the three short arrays. Result of using a-priori information as a starting model, in SurfSeis©.

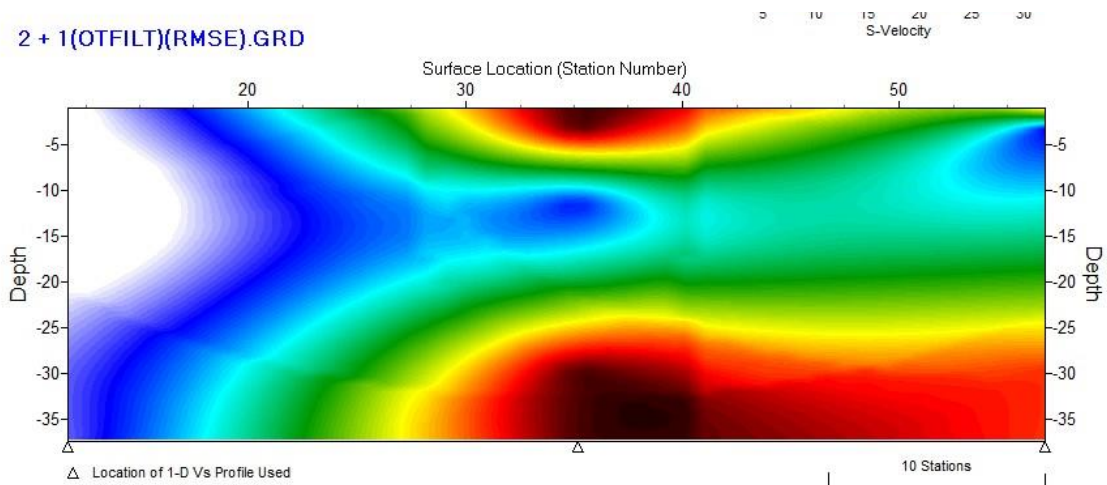


Figure E.9 - Associated RMSE profile. Notice the left section has a better inversion fit.

## E.2 – MASW of Long Array

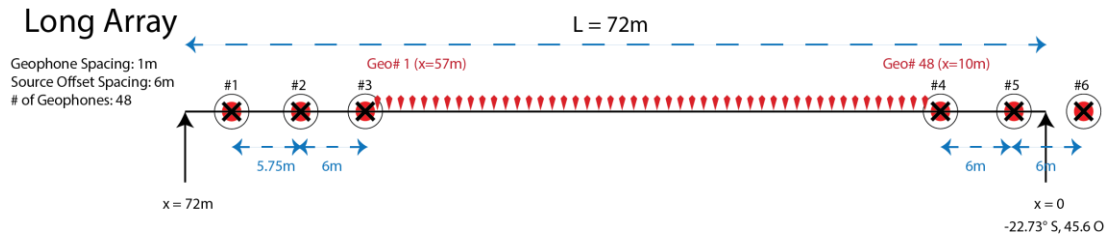
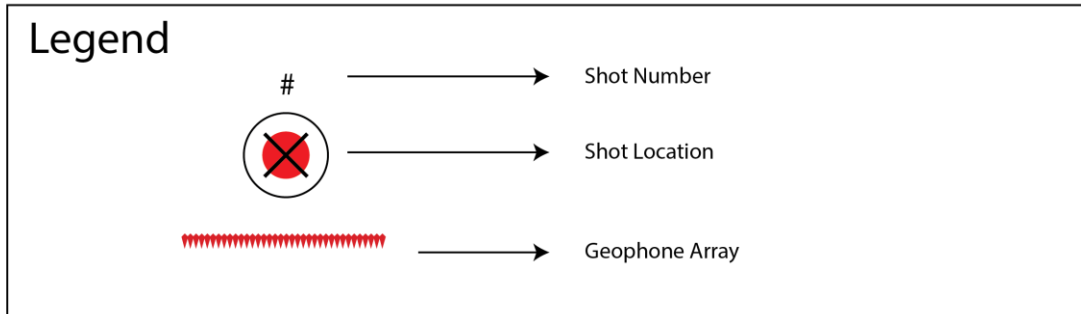
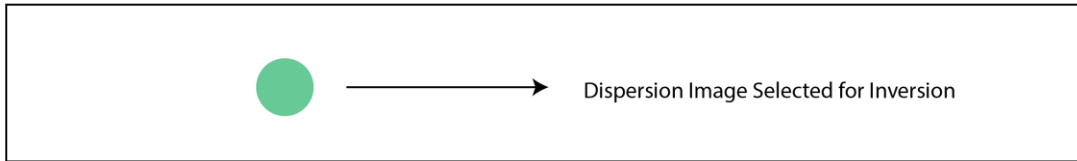


Figure E.10 - A diagram of the long array, showing shot locations. The length of the geophone array is 47 m.



### E.2.1 – Selection of Best Dispersion Images



## Dispersion Images Midpoint (x = 33.5m)

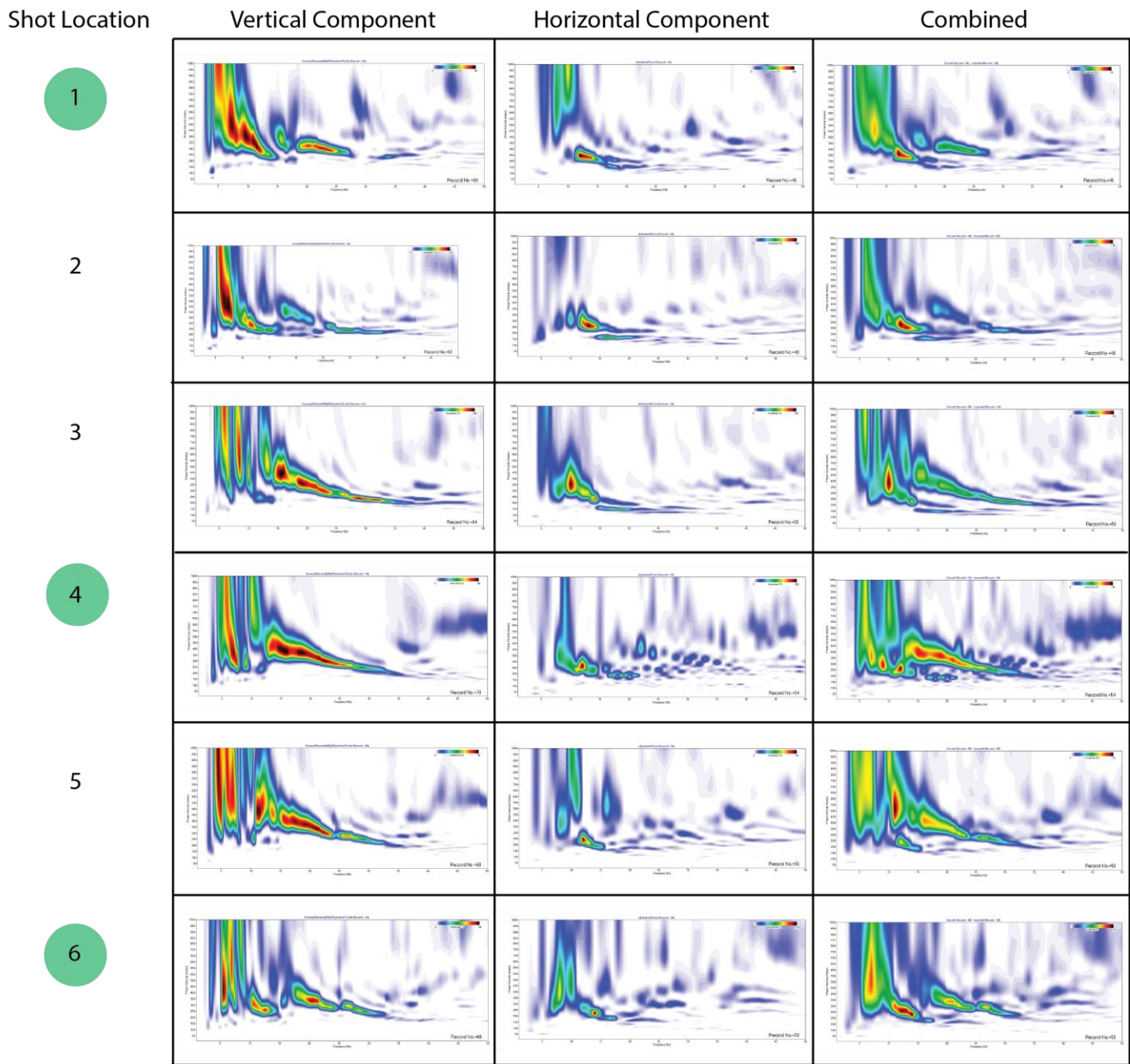


Figure E.11 - Dispersion images for the long array shown in the previous page for a variety of shot locations. Horizontal and vertical components are shown separately and then combined. The best images are selected by the green circle.

## E.2.2 – Dispersion Curve Selection & Inversion

### Dispersion Curve Selection

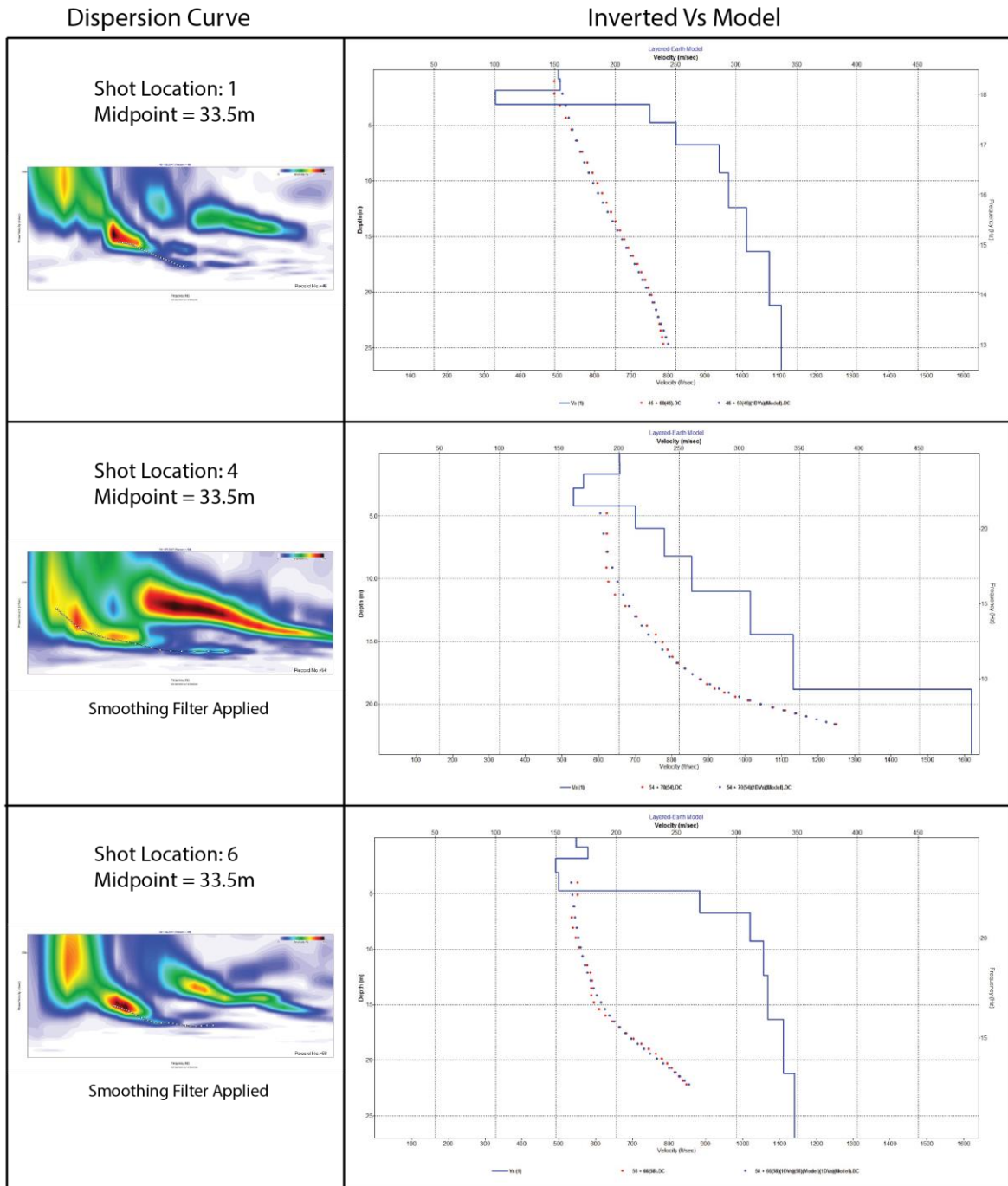


Figure E.12 - Individual inversions of the picked dispersion curves (left) of the best dispersion images. The perceived best is selected by a green circle.

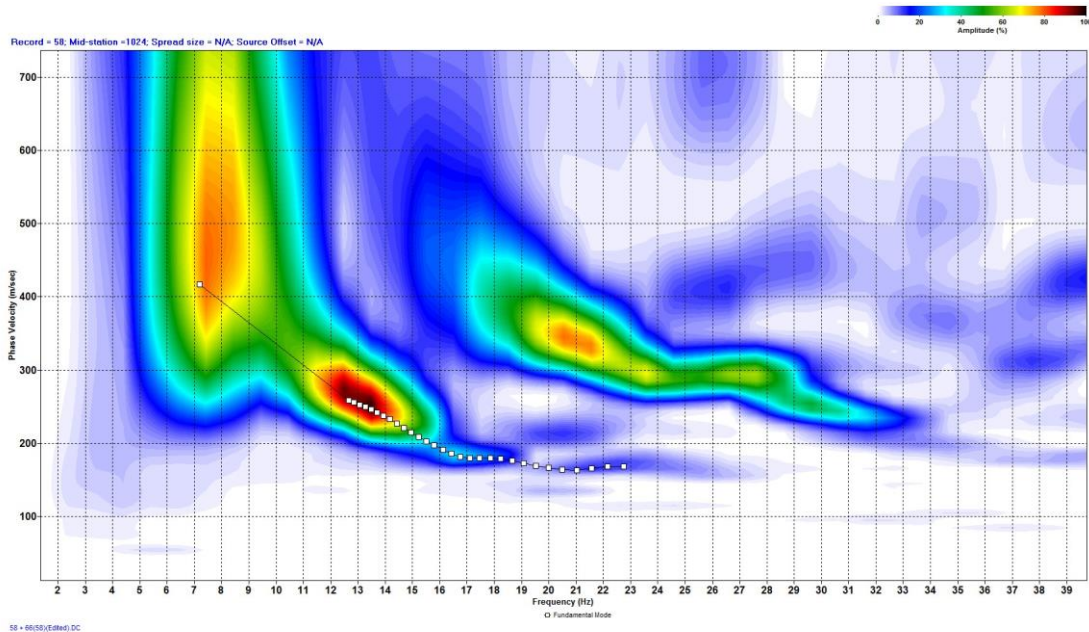


Figure E.13 - Reanalysis of the bottom picked dispersion curve in Figure E.12, by adding one more point at a lower frequency.

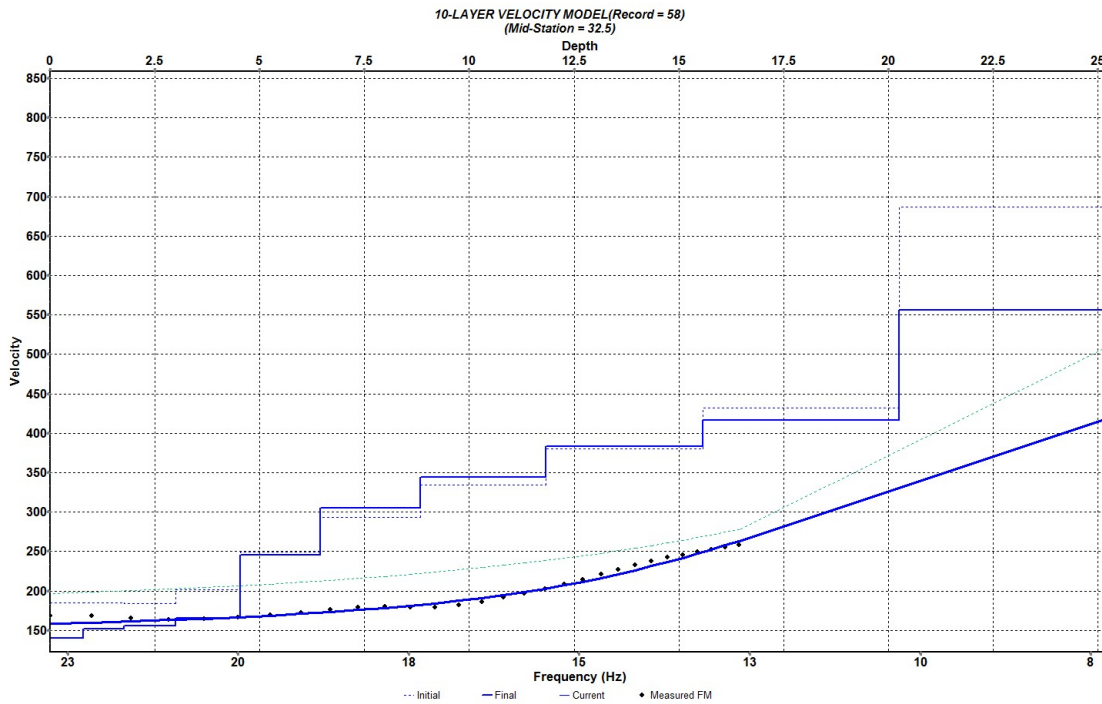


Figure E.14 - Inversion of the redefined dispersion curve using the default initial model in SurfSeis©. The Shear wave velocity profile shown along with the dispersion curve.

### E.2.3 – Comparison of Synthetic and Real Data

<Inverted Layer.LYR>

Layer	Bottom (m)	H* (m)	Vs* (m/sec)	Vp* (m/sec)	POS*	Rho*	Qs*	Qp*
1	0.790	0.790	140	454	0.448	1.550	5	20
2	1.770	0.980	152	454	0.437	1.600	10	30
3	2.990	1.220	156	452	0.432	1.650	10	30
4	4.530	1.540	166	495	0.437	1.700	20	50
5	6.450	1.920	245	609	0.403	1.750	20	50
6	8.840	2.390	305	717	0.390	1.800	50	150
7	11.840	3.000	344	818	0.393	1.850	50	150
8	15.580	3.740	383	931	0.398	1.900	50	150
9	20.260	4.680	417	1057	0.408	1.950	50	150
10	Half Space	Infinity	556	1684	0.439	2.000	75	250

\* H: Thickness, Vs: S-wave velocity, Vp: P-wave velocity, POS: Poisson's ratio, Rho: density in gm/cc, Qs: Q-factor for S-wave, Qp: Q-factor for P-wave

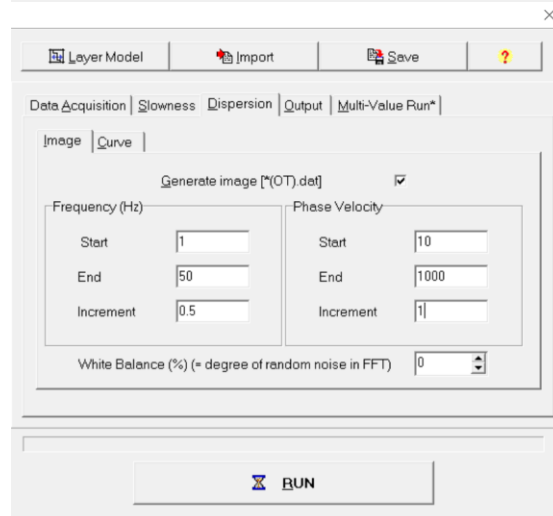
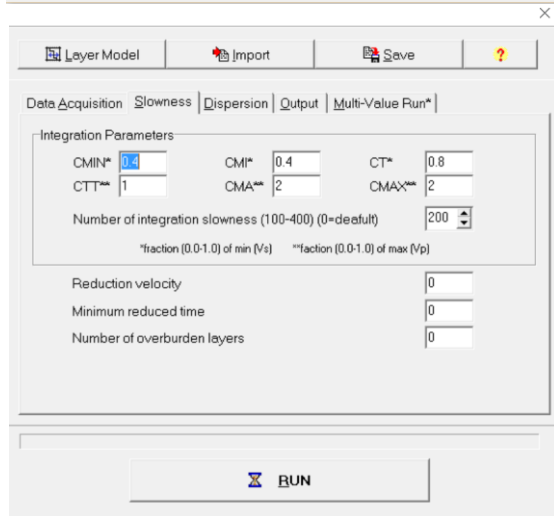
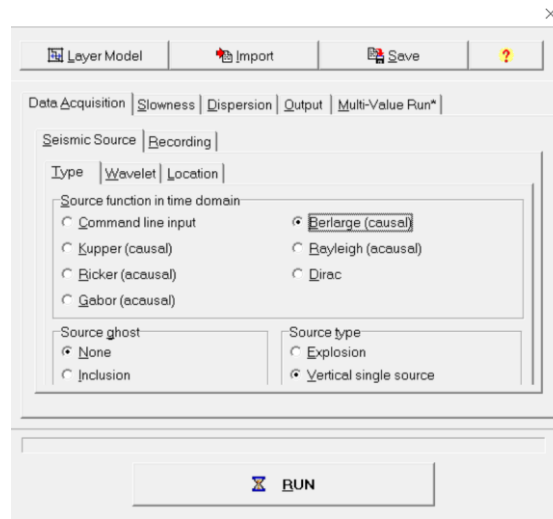
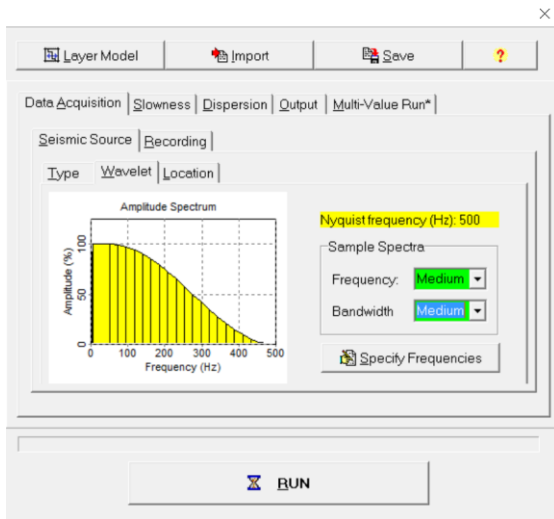


Figure E.15 – Synthetic model derived from inversion results from figure E.14 (long array) (top). And below are shown the parameters to create synthetic seismograms in ParkSEIS©, with same field parameters as in Figure E.10 (shot locaiton 6).

# Appendix E

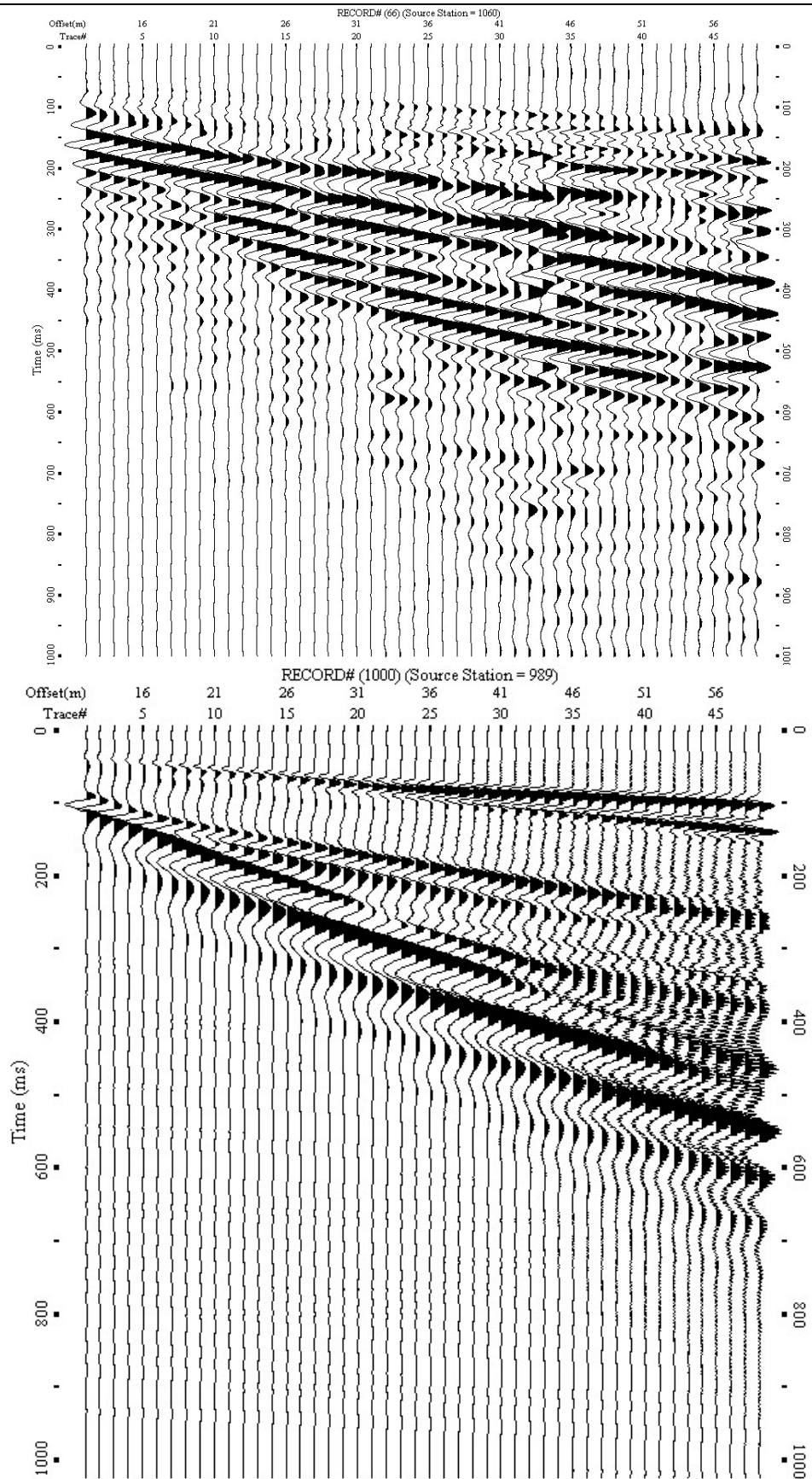


Figure E.16 – Real field data seismogram (vertical component) of shot location 6 (Figure E.10) for the long array (top). Synthetic data produced by modeling module in ParkSEIS© (bottom) with same field parameters based on inverted synthetic model (Figure E.15).

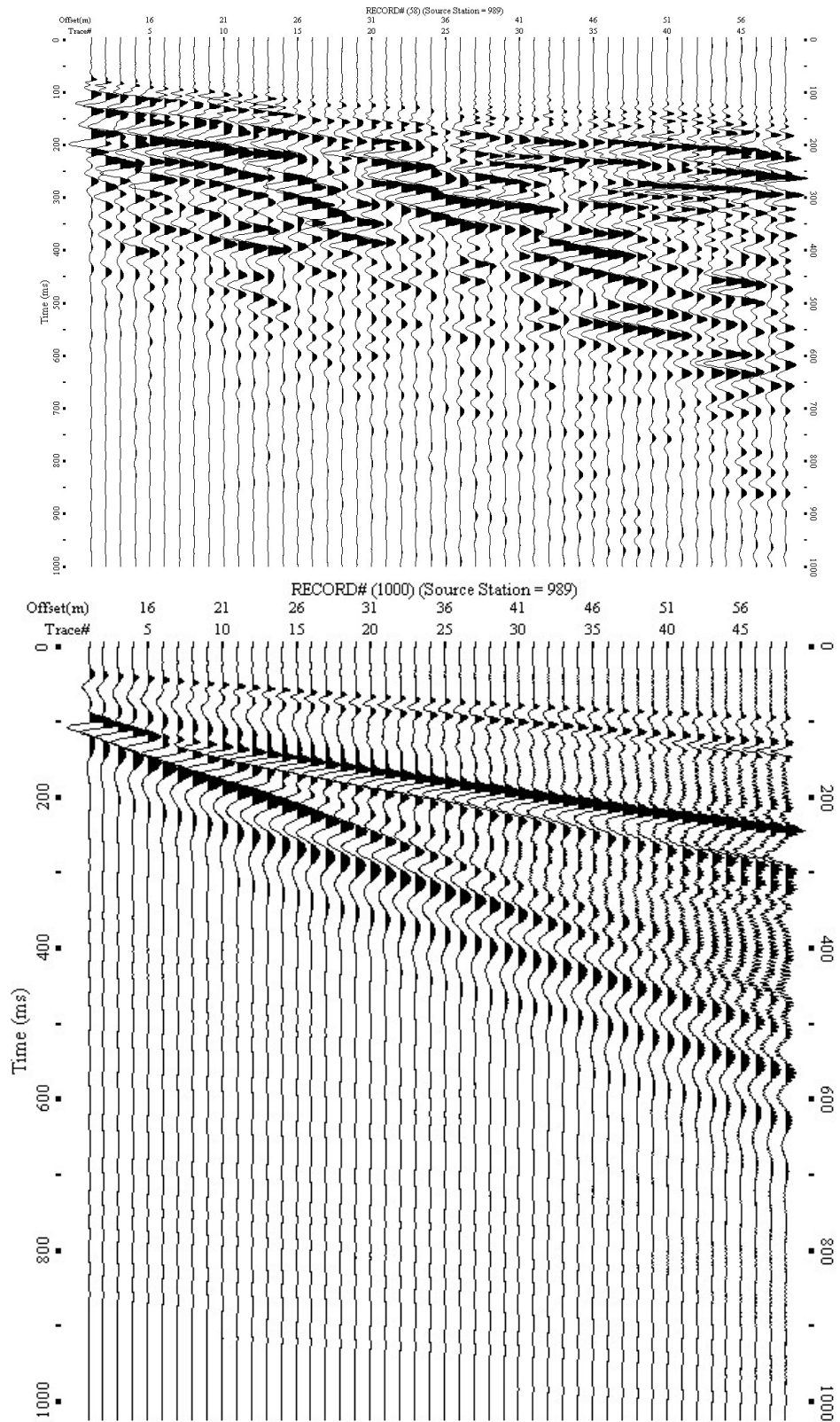


Figure E.17 – Real field data seismogram (horizontal component) of shot location 6 (Figure E.10) for the long array (top). Synthetic data produced by modeling module in ParkSEIS© (bottom) with same field parameters based on inverted synthetic model (Figure E.15).

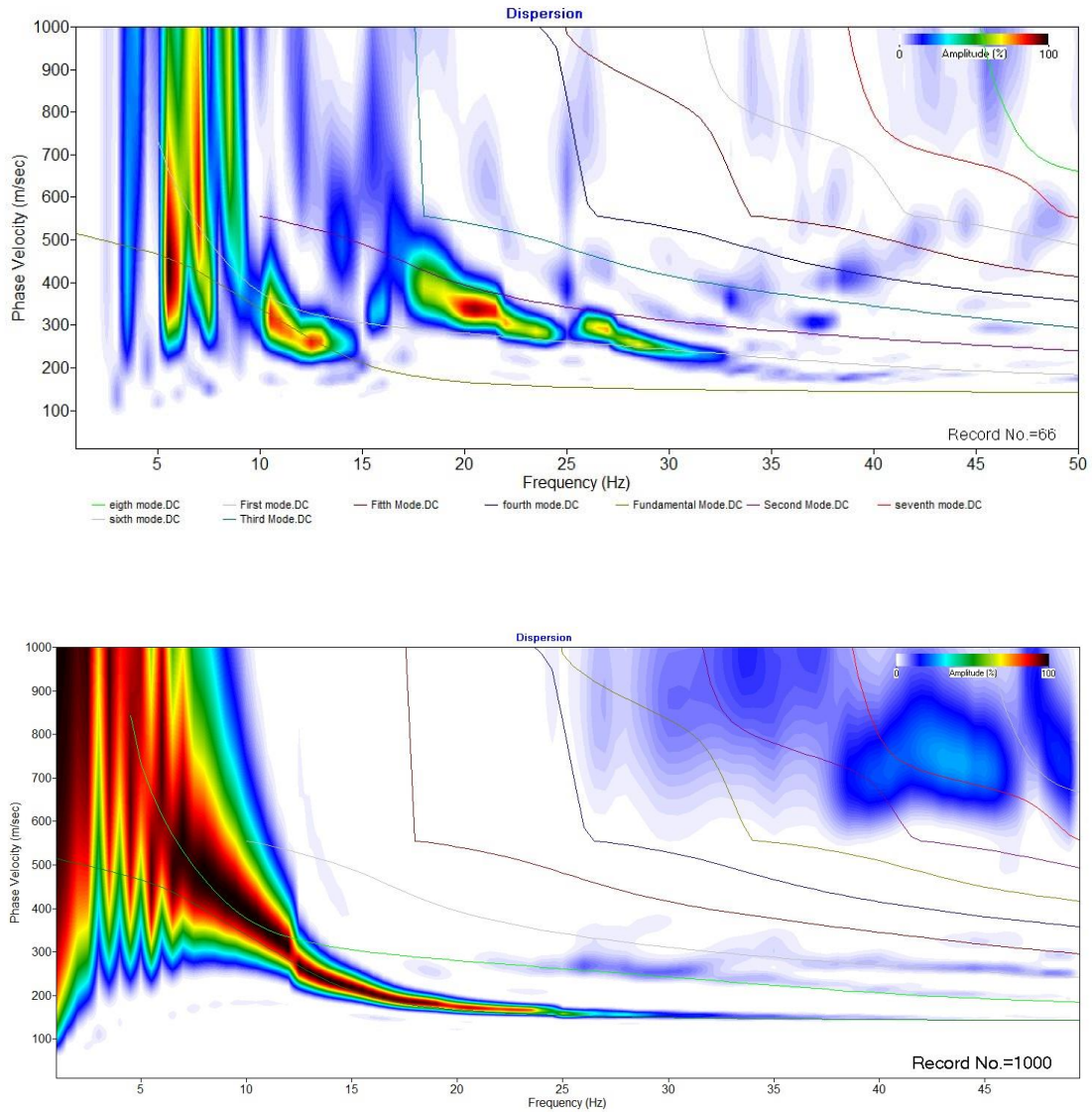


Figure E.18 – Dispersion image from real field data of shot location 6 (Figure E.10) for the long array and vertical component (top). Dispersion image from the vertical component synthetic data produced by modeling module in ParkSEIS© (bottom) with same field parameters based on inverted synthetic model (Figure E.15). Both dispersion images include the synthetic dispersion curves (fundamental to mode 8) which belong to the inverted synthetic model (Figure E.15).

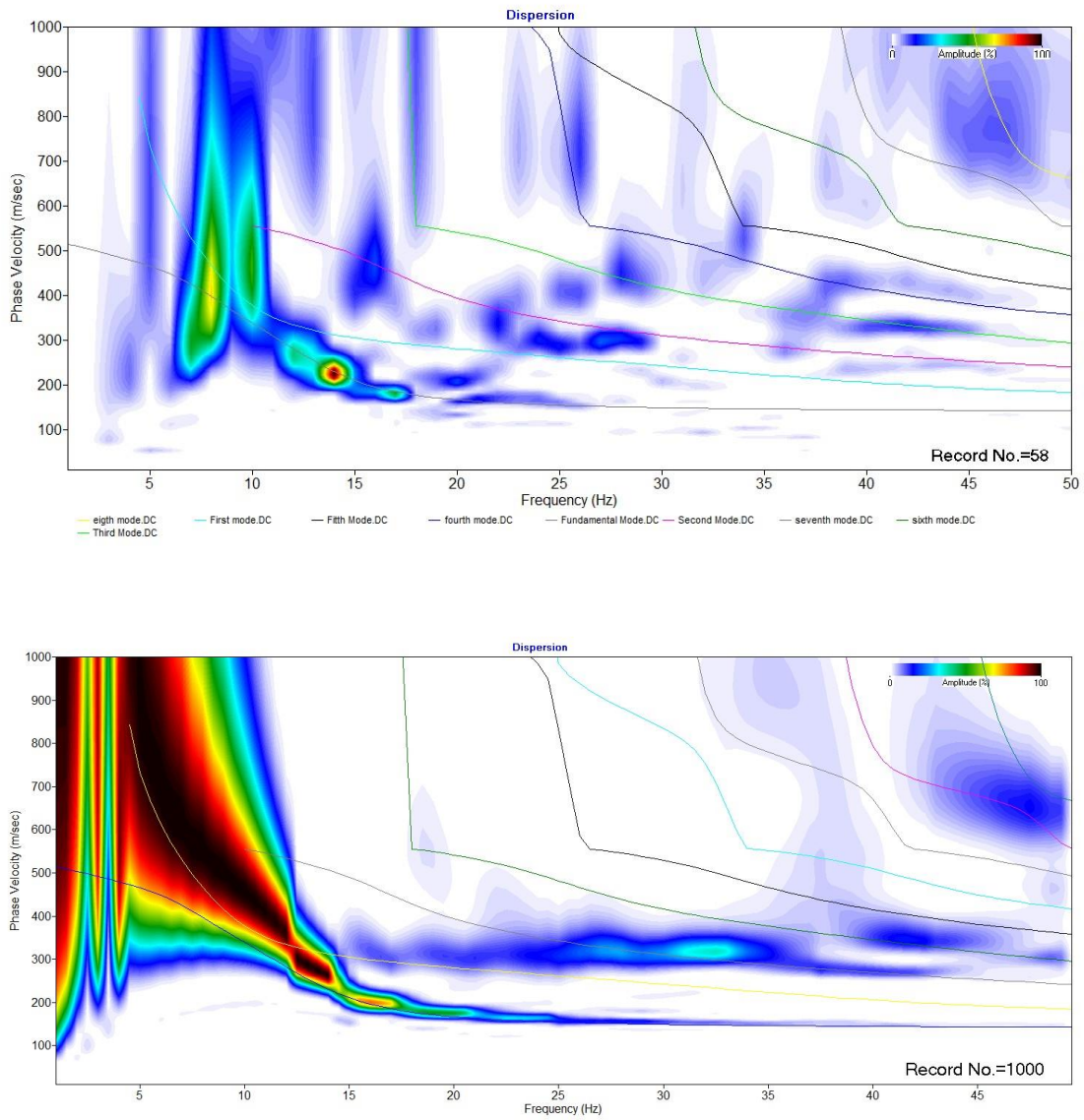


Figure E.19 - Dispersion image from real field data of shot location 6 (Figure E.10) for the long array and horizontal component (top). Dispersion image from the horizontal component synthetic data produced by modeling module in ParkSEIS© (bottom) with same field parameters based on inverted synthetic model (Figure E.15). Both dispersion images include the synthetic dispersion curves (fundamental to mode 8) which belong to the inverted synthetic model (Figure E.15).

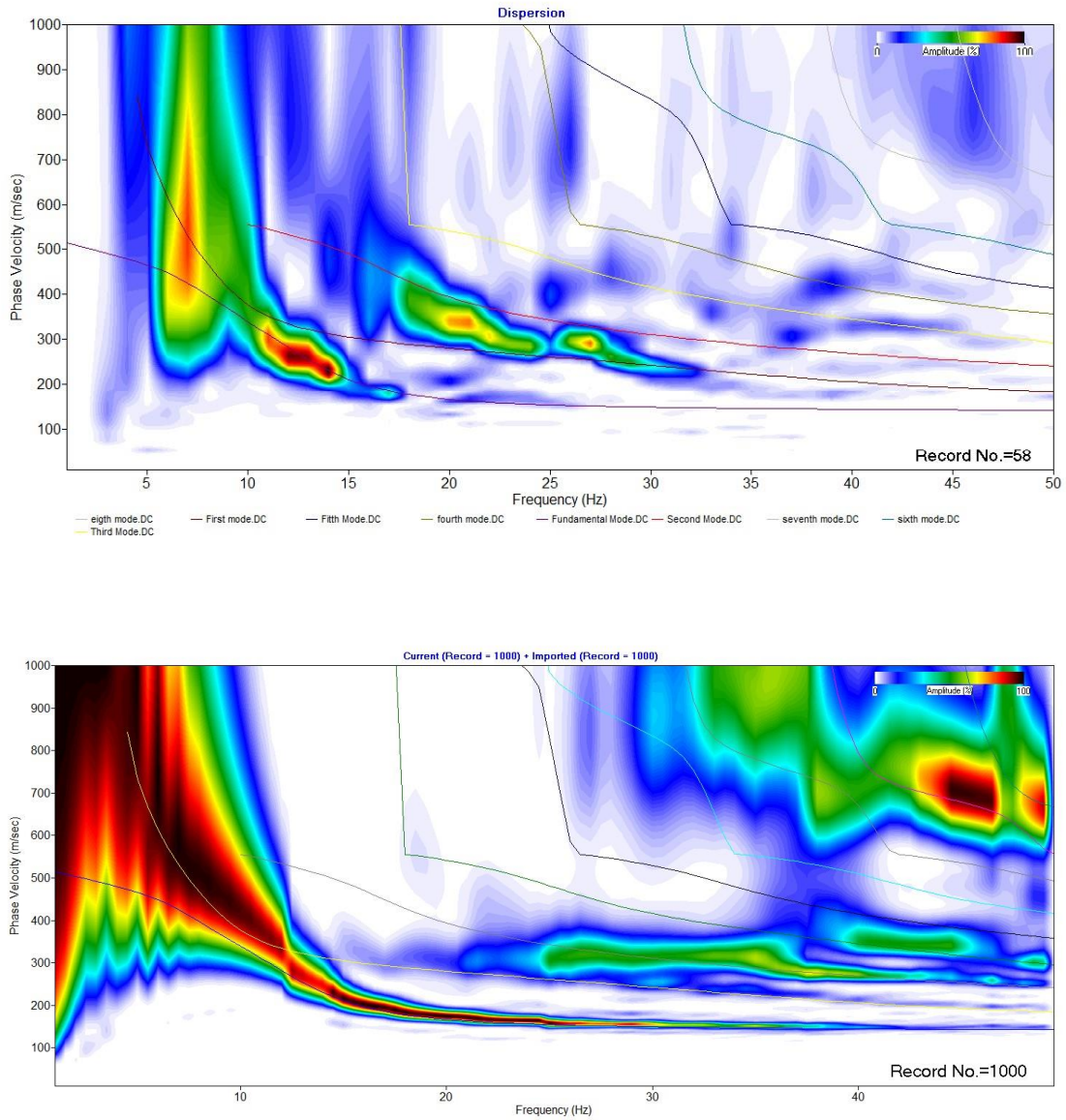


Figure E.20 - Dispersion image from real field data of shot location 6 (Figure E.10) for the long array and combined horizontal and vertical components (top). Dispersion image from the combined horizontal and vertical component synthetic data produced by modeling module in ParkSEIS© (bottom) with same field parameters based on inverted synthetic model (Figure E.15). Both dispersion images include the synthetic dispersion curves (fundamental to mode 8) which belong to the inverted synthetic model (Figure E.15).